The Dissertation Committee for Russell Wirkus Carter Certifies that this is the approved version of the following dissertation:

Fluid Characterization at the Cranfield CO_2 Injection Site: Quantitative Seismic Interpretation from Rock-Physics Modeling and Seismic Inversion

Committee:

Kyle T. Spikes, Supervisor

Mrinal K. Sen

Robert H. Tatham

Susan Hovorka

Peter Eichhubl

Fluid Characterization at the Cranfield CO_2 Injection Site: Quantitative Seismic Interpretation from Rock-Physics Modeling and Seismic Inversion

by

Russell Wirkus Carter, B.A.

Dissertation

Presented to the Faculty of the Graduate School of

The University of Texas at Austin

in Partial Fulfillment

of the Requirements

for the Degree of

Doctor of Philosophy

The University of Texas at Austin

December 2014

Dedication

To all those who have inspired me but who never knew it.

Acknowledgements

While I cannot claim to have achieved more than anyone else I can claim that I have achieved more than I would have had I been working on my own this entire time. My life to this point has not been influenced only by myself though; it has been a group effort. There have been many people from all walks of life who have helped me in ways known, and in ways unknown.

Had it not been for a well-placed undergraduate advisor at Colgate University, I might never have become a geologist and subsequently pursued geophysics. I would not be where I am without the help of Dr. Richard April, the advisor, friend, and mentor who first introduced me to the world of geology. Without Dr. April and the rest of the Colgate Geology department, I might have followed my original freshman goal of becoming a politician. Changing course to geology was a decision that I would never have made on my own and is one that I have never regretted.

From Colgate I migrated to San Francisco where I was, again, not without guidance and mentors. It was in San Francisco where I was hired to my first real job. While working at Fugro, I had a forgiving and understanding supervisor, Glenn Young, who helped me developed a work ethic and an understanding of the professional world that has served me every day over the course of my PhD. Glenn also recognized some potential in me and placed me on a variety of assignments both domestically and internationally. It was while working offshore in the Arabian Gulf that I had my first introduction to geophysics and from that assignment my fate to be a geophysicist was sealed.

During my first term at the Jackson School I felt as though I was lost at sea in a rapidly sinking vessel. Were it not for the amazing faculty and staff I would never have found safe harbor in a project that excited me nor would I have acquired the knowledge base to complete it. Of the faculty members at UT, I thank my committee members, Dr. Sen, Dr. Tatham, Dr. Hovorka, and Dr. Eichhubl. Without their input, suggestions, and encouragement I would still be struggling with where to start on my research. I also would like to thank Dr. Steven Grand who helped me to find new joy in science when I was in the doldrums. He reminded me that there could be joy science even if discoveries were elusive. Naturally, and with great admiration, I thank my advisor Kyle Spikes. Kyle saw potential in me before any one else at UT ever did. His leap of faith to admit me gave me the encouragement and the motivation to strive for my best and to test the limits of my own abilities. Certainly we had our disagreements and quarrels, but with out them I would not have questioned my own methods and abilities to arrive where I am now. Over the course of my degree Kyle has shared his knowledge and given me guidance and support that has been the envy of my peers in other research groups.

The help I have received at UT has not come only from the faculty. Regarding my research, Thomas Hess has done more for me in my time here than many other staff combined. He put in endless hours working with me and entertaining my near random ideas for data manipulation and processing. Without him I would still be struggling with how to load my data volumes. Philip Guerrero, the graduate student advisor, has been worth his weight in gold in ensuring that I have crossed all my t's and dotted all my i's on the administrative front. In addition to that he has been a friend who has welcomed me to Austin and made my time here enjoyable. In addition to those two, the staff of the Jackson school has backed me this entire time and made sure that I had the facilities needed to complete my research.

Within the four walls of my office and research lab I have not been alone in my seemingly endless string of struggles and confusions. The confusions and struggles would have been endless had it not been for my fellow graduate students, especially my office mates over the years. Meijuan Jiang, an unexpected friend who over the years has been a constant help, provided stimulating and thought provoking discussions regarding not only work, but also life, future, happiness, and finding meaning in it all. Kwon Taek Oh and Chang Lu have also helped to ensure that my smiles and question are not mine alone, but are shared with friends. I cannot list here all the students who I have come across while at UT, but a few that have left the largest impact are Isaac Smith, Bruce Frederick, Kumar Das, Alex Lamb, Sharif Morshed, Qi Ren, Yang Wang, and Terrence Campbell. Thank you, you have kept me sane and, more often than not, focused while I have been here.

I would also like to thank the member companies of the EDGER forum as their generous contributions helped fund my work while at UT. The data analyzed in this study were collected as part of the research into effective monitoring of CO_2 storage by The Gulf Coast Carbon Center at the University of Texas at Austin Bureau of Economic Geology as part of the Southeast Regional Carbon Sequestration Partnership contract number DE-FC26-05NT42590. I also would like to thank the field operator, Denbury Onshore LLC, and Thomas Daley at Lawrence Berkeley National Laboratory for providing me with data.

Obviously I would not be where I am without the support of my family. Firstly to my mother, Lydia Wirkus, who always believed in me and has pushed me to achieve greatness from day one. While I have not yet achieved greatness, I feel I am one step closer now than before. She is also the one who many years past gave me a rock hammer for a birthday gift. That gift helped to nurture my curiosity and encourage me to always

question what I saw. It didn't take me long to realize that even the most boring looking piece of shale could contain a fossilized leaf or animal mold. Those early exposures to discovery served me well and taught me that scientific discovery could be interesting and exciting. Words fail me as to how I can thank Faustin Carter, my brother. He has always been there for me and has always shown me the way either through his own example or through words of guidance. I would be but a shadow of my current self without him. To the rest of my family, thank you for always picking me up when I fail and for helping to remind me that all my stumbles through life are only temporary set backs.

Lastly, I thank Dr. Zeilenger. She has believed in me since before I believed in myself.

Fluid Characterization at the Cranfield CO_2 Injection Site: Quantitative Seismic Interpretation from Rock-Physics Modeling and Seismic Inversion

Russell Wirkus Carter, Ph.D.

The University of Texas at Austin, 2014

Supervisor: Kyle T. Spikes

This dissertation focuses on quantitatively interpreting the elastic properties of the Cranfield reservoir for CO_2 saturation. In this work, quantitative interpretation starts by examining the relationship between CO_2 saturation and the elastic properties of the reservoir. This relationship comes from a rock-physics model calibrated to measured well data. Seismic data can then be inverted using a model for CO_2 saturation and rock-property estimates.

The location and saturation of injected CO_2 are important metrics for monitoring the long-term effectiveness of carbon capture utilization and storage. Non-uniform CO_2 saturation is a contributing factor to both lateral and time-lapse changes in the elastic properties of the Cranfield reservoir. In the Cranfield reservoir, CO_2 saturation and porosity can be estimated from the ratio of P-wave velocity (*Vp*) to S-wave velocity (*Vs*) and P-impedance (*Ip*), respectively. Lower values of *Ip* for a given rock matrix often correlate to higher porosity. Similarly, for a given area of the reservoir, lower *Vp*/*Vs* frequently can be associated with higher CO_2 saturation. If a constant porosity from the

baseline to the time-lapse survey is assumed, changes in *Ip* over time can be attributed to changes in CO_2 saturation in lieu of using *Vp*/*Vs*. Decreases in *Ip* between the baseline and time-lapse survey can be attributed to increases in CO_2 saturation. With a rock-physics model calibrated to the reservoir, *Ip* and *Is* from a vertical seismic profile were correlated to statistical ranges of porosity and CO_2 saturations. To expand the lateral interpretation of reservoir porosity and CO_2 saturation, the time-variant changes in *Ip* between baseline and time-lapse surface seismic datasets were compared to changes in CO_2 saturation calculated from the rock-physics model.

Characterizing the CO_2 saturation of the Tuscaloosa sandstones helped to establish a workflow for estimating reservoir properties and fluid saturation from multiple types of geophysical data. Additionally, this work helped establish an understanding for how CO_2 injected into a reservoir alters and changes the elastic properties of the reservoir and the degree to which those changes can be detected using geophysical methods.

Table of Contents

List of Tables

List of Figures

Chapter 1: Introduction

1.1 MOTIVATIONS AND OBJECTIVES

Improving the methods and accuracy to monitor and track CO_2 injected into the subsurface has the potential to help improve the efficiency of sequestration and storage of anthropogenically emitted CO_2 emissions. Additionally, improved monitoring can help to increase the efficiency of enhanced oil recovery (EOR) from CO_2 injection. Since the 1950's, a pronounced increase in global CO_2 emissions has caused the atmospheric CO_2 concentration to reach levels unprecedented in the past 800,000 years (IPCC, 2013). At the same time that global emissions of CO_2 have increased, many mature hydrocarbon fields have been depleted or have started to reach the extents of their expected life cycles. Injection of CO_2 into depleted or nearly depleted reservoirs for carbon storage and utilization has the potential to help reduce the amount of CO_2 released into the atmosphere while at the same time increasing the productivity and prolonging the life span of some existing mature and producing or already abandoned fields.

Monitoring CO_2 after injection into the reservoir to ensure secure long-term storage and sweep efficiency is a significant challenge. A wide array of reservoir properties can impact CO_2 migration. These properties can include reservoir depth, thickness, porosity, original fluid composition, mineralogy, grain shape, permeability, pressure, temperature, fractures, and seal capacity. Some of these properties can be obtained from conventional surface seismic data, and some can change due to the injection of CO_2. Properties that can change due to CO_2 injection include pressure, saturation, fracture density and orientation in the reservoir and caprock, and permeability.

Monitoring and tracking CO_2 injected into reservoirs while trying to account for even some of these changes is a challenging and active field of study.

Rock-physics models provide a way to link lithological parameters in the reservoir with the observed elastic parameters sampled with surface seismic waves and well log measurements. Of the wealth of rock-physics models that have been developed over time, certain classes of models are most effective to explain specific rock types under various conditions. A requirement for the work presented in this dissertation was that the model must be able to explain a mixed-grain material with intergranualar cement. In addition to modeling the rock structure, the model also must accommodate fluid substitution in order to explain a range of fluid saturations with the end members being brine, hydrocarbon, or CO_2.

This research has been completed by examining CO_2 injection and sequestration in the cemented sandstone of the Tuscaloosa Formation. However, the nature of this work is such that the workflows presented here are adaptable to a broad range of applications. Changing the rock-physics model will allow for the workflow described here to be used with different types of host rock formations. Using different elastic parameters for the fluids will allow the methods presented here to be applied to situations where the fluids, injected or produced, are different from the ones used in this dissertation. One of the workflows in this dissertation provides a template to estimate porosity and fluid saturation in a multi-phase environment when only a single multi-component vertical seismic profile (VSP) is available. The multicomponent survey provides P-impedance (*Ip*) and S-impedance (*Is*) information. A separate workflow is presented for situations where two or more vintages of surface seismic information

containing *Ip* is available, but *Is* information is not available. Both workflows present a way to estimate the porosity and fluid saturation within a reservoir and provide some constraints on mineralogy of the reservoir.

Lateral changes in the *Ip* and *Is*, or time-dependent changes in the *Ip* of the reservoir, permit interpretation of the spatial variation of porosity and fluid saturation within a reservoir. In situations where both *Ip* and *Is* are available, porosity is estimated primarily as a function of *Ip*, while pore fluid is primarily a function of *Ip/Is*. When time-dependent *Ip* of a reservoir is available, porosity is a function of the baseline *Ip*. Changes in fluid saturation in a reservoir between vintages of data is a function of changes in *Ip* between the two datasets.

1.2 STRUCTURE OF THE DISSERTATION

Chapter 2 presents the study area and the data used in this dissertation. The geological description and production history of the Cranfield study area are also introduced. Additionally, the available data is reviewed, and a discussion of the types of data, their lateral extents, and the limitations and benefits of each type of data is presented. Finally, this chapter contains information regarding the mineral and fluid properties used throughout the subsequent chapters.

Chapter 3 presents a few of the common geophysical techniques used in subsequent chapters. The fundamentals of amplitude variations with angle are presented as well as the Aki and Richards (1980) form of the angle-dependent reflectivity equations. Rock-physics models are reviewed, namely the contact cement model (CCM), which is the model used in subsequent chapters of this dissertation. A review of model-

based inversion of surface seismic data is given as well as a brief overview of the statistical methods used in later chapters.

Chapter 4 establishes the relationship between the lithologic parameters and the elastic properties of the Cranfield reservoir through the use of rock-physics modeling. This chapter also examines how different saturations of injected CO_2 alter and change those same elastic properties. This relationship is the first major step in the workflows presented in later chapters. The results and findings from this chapter guided the direction of subsequent research and identified a set of elastic parameters that help to differentiate between different concentrations of CO_2 saturation. The elastic parameters that best differentiated changes in CO_2 saturation were the ratio of P-wave velocity (*Vp*) to S-wave velocity (*Vs*) and *Ip*. This work also provided the sensitivity analysis of the reservoir elastic parameters to changes in CO_2 saturation.

Chapter 5 takes the best performing elastic parameters from Chapter 4 and integrates them with probabilistic rock-physics modeling and seismic impedance inversion. This chapter presents a methodology for using a single vintage of a 3D 3C VSP to determine both the CO_2 saturation and the porosity of the sampled portion of the reservoir. The workflow provides probabilistic estimates of CO_2 saturation and porosity using a rock-physics model calibrated to the reservoir. The methodology was tested initially on well log data that was simulated to show varying concentrations of CO_2 saturation in order to determine the accuracy of the final CO_2 and porosity estimates. To estimate reservoir porosity and saturation, *Ip* and *Is* data were inverted from the multicomponent 3D VSP data, and then the calibrated rock-physics model was inverted using those same *Ip* and *Is* values. Resulting estimates of porosity showed a high

correlation to the measured porosity logs. Estimates of CO_2 saturation indicated the ability to infer some information regarding location and saturation of CO_2, but not with the same accuracy as the porosity measurements.

Chapter 6 adapts the workflow presented in Chapter 5 to be compatible with time-lapse surface seismic data. Two vintages of surface seismic data were used, and a double difference rock-physics approach was used to estimate, probabilistically, the CO_2 saturation and porosity. The double difference formulation used the *Ip* information from the baseline seismic data to estimate the porosity of the reservoir. The porosity estimates were taken as the constant initial model from which CO_2 saturation was probabilistically estimated using a version of the CCM computed for a range of CO_2 saturations. The changes in *Ip* between the baseline and the time-lapse surface seismic surveys could then be quantitatively linked to changes in fluid saturations. Probabilistic estimates of CO_2 saturation showed CO_2 accumulating primarily in the vicinities of the injection wells.

Chapter 7 discusses the overall conclusions of the dissertation in addition to presenting addition avenues for future work. Initial results showed that *Vp/Vs* and *Ip* were the elastic parameters that were best suited to discriminate different CO_2 saturations. Results from the work using the VSP and the two vintages of surface seismic data showed similar porosity and spatial distributions of CO_2. However, there are some saturation differences between the results from the two methods where the datasets overlap. At the field scale the results showed that the reservoir porosity is similar to the initial estimates and observations. Accumulations of CO_2 within the reservoir were primarily located at and around the locations of injection wells. Additionally, results

from this work agreed with results from other studies pertaining to the locations and approximate sizes and saturations of some CO_2 accumulations.

Chapter 2: Study Area and Data

This chapter introduces the Cranfield study area. The location, setting, geology and history are presented first, and then the available data that were used for different parts of this study are presented second. The focus of this study was the Cranfield reservoir, which is located in west-central Mississippi near Louisiana. The reservoir is comprised of the Tuscaloosa Sandstones of Upper Cretaceous age. This project is run by The Gulf Coast Carbon Center at the University of Texas at Austin Bureau of Economic Geology in conjunction with the Southeast Regional Carbon Sequestration Partnership and the local field operator. Available data include two vintages of 3D surface seismic data, a single post-injection multicomponent 3D VSP, and numerous well logs from within the area of the CO_2 sequestration study and also from the surrounding areas of the producing reservoir.

2.1 GEOLOGIC DESCRIPTION AND FIELD HISTORY

The study area is located in Mississippi near the town of Natchez and the border of Louisiana (Figure 2.1). The target interval is a siliciclastic reservoir and is part of the Lower Tuscaloosa Formation, which has been dated to the Upper Cretaceous. Depth of the reservoir is about 3050 to 3200 meters below sea level. Within the reservoir, temperature and pressures are about 125 C and 32 MPa, respectively (Lu et al., 2012a). Porosity of the Cranfield reservoir is between 0–37% with an average porosity value of 20% (Lu et al., 2012b). Permeability of the Cranfield reservoir is typically between 0.1–1000 millidarcies (Lu et al., 2012b). Alternating sequences of sands and shales are present in the Late Cretaceous section, with shales comprising the reservoir seals and the

sands forming the reservoir rock. A regional seal of Middle Tuscaloosa age is formed by the presence of a thick marine shale (Figure 2.2). Buoyant rising of a local salt body is forcing a local four-way anticline at the location of the Cranfield study area and has caused the reservoir portion of the anticline to dip 1–3° (Zhang et al., 2013a).

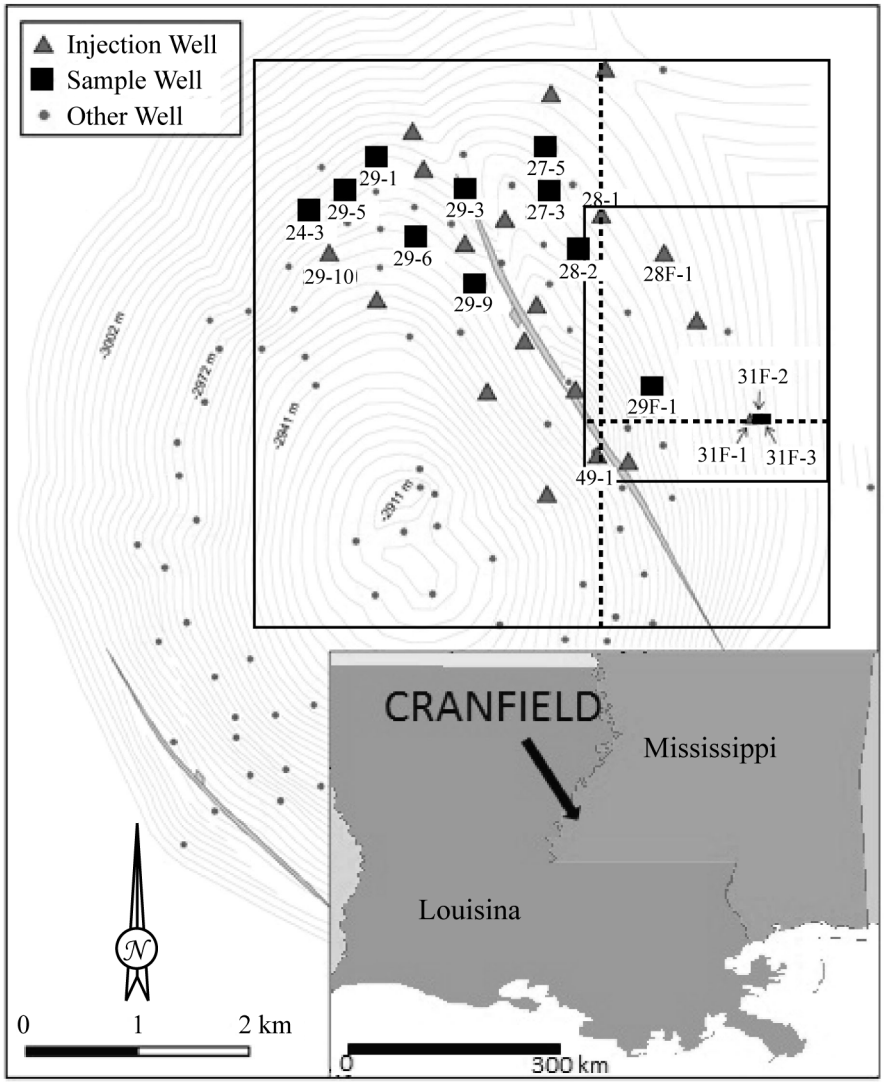

Figure 2.1: Map of the study area. Gray triangles show injection wells, black squares show the sample wells, and small gray circles show other wells. The large black box shows the approximate extent of the 3D surface seismic surveys. The small black inset box shows the approximate location of the 3D VSP dataset. The vertical dashed line indicates inline number 1084, and the horizontal dashed line within the 3D VSP area shows a portion of cross line 197. A sealing fault is shown running diagonally across the study area.

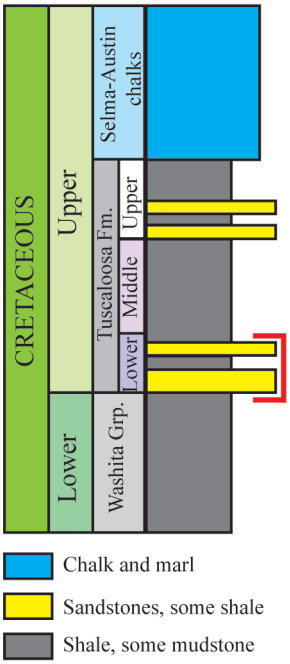

Figure 2.2: A generic stratigraphic column for the Cranfield reservoir area. The reservoir zone is part of the Lower Tuscaloosa and is shown by the lower pair of yellow sandstones. The Tuscaloosa Formation sits below the Austin Chalks and above the Washita-Fredericksburg Group. The thick marine shales of the Middle Tuscaloosa act as the regional seal for the reservoir. The reservoir zone has been highlighted by the red bracket and is on average approximately 30 m thick.

Core samples from the Cranfield reservoir sands indicate that the grain size ranges from conglomerates to muddy sandstones (Lu et al., 2012b). The fining upward sequences found in the reservoir zone are typical of areas that are associated with meandering stream channels. Mineralogy of the reservoir has been shown by Kordi et al. (2010) at the location of well F-2 to be composed primarily of 60–80% quartz, 10–20% clay, and 10–20% feldspar, with the remainder being small percentages of muscovite, calcite, and other minerals. The primary authigenic mineral in the reservoir is chlorite, which formed as a grain-coating mineral (Lu et al., 2012a). By forming primarily as

grain coating as opposed to pore filling, the introduction of chlorite has not been at the expense of significant porosity and has allowed the chlorite to act as a grain-contact cement. Additionally, the formation of chlorite around the mineral grains has helped to prevent the formation of intergranular quartz cement (Lu et al., 2012a).

Production at the Cranfield reservoir was active between the years of 1943 to 1966. With modern developments in EOR from CO_2 injection, the site recently has been revived as a location of hydrocarbon production in part because of regionally available CO_2 and existing local infrastructure (Lu et al., 2012a). The CO_2 sequestration study area is located within the Detail Area Study (DAS), which is 4 km^2 in size, and is contained within the small black box on Figure 2.1. The wells within the DAS consist of one injection well, CFU-31F-1 (F-1), and two down dip monitoring wells, CFU-31F-2 (F-2) and CFU-31F-3 (F-3). Injection rates of CO_2 into well F-1 ranged between 200 to 500 tons per day and were achieved over the duration of CO_2 injection from December 2009 to late 2010. Over 4.8 million tons of CO_2 have been injected in the entire Cranfield area since the start of EOR and the sequestration study.

2.2 DATA DESCRIPTION

The seismic data used for this work included two vintages of 3D surface seismic data, one from 2007, before CO_2 injection started, and a second (monitoring survey) from 2010, after a significant amount of CO_2 had been injected into the reservoir zone. Both vintages of seismic data covered approximately 36km^2 (6 km x 6 km). The surveys overlapped for 221 inlines (1003–1224) and 242 cross-lines (109–351). Inline and cross-line spacing was 25 m. A single multicomponent 3D 3C VSP was also used in this work. The VSP data was acquired in 2010 after a significant amount of CO_2 had been injected

into the reservoir interval. In addition to the surface seismic and 3D VSP data, well log data from within the DAS area were available. Select well log curves were also available from some wells outside of the DAS area.

2.2.1 Surface Seismic Data

This study used two vintages of poststack 3D surface seismic data. The baseline data was acquired in 2007, and the time-lapse data was acquired in 2010. The seismic source for both the baseline and time-lapse datasets was Vibroseis©. The baseline data and the time-lapse data have been gridded to have the same acquisition footprint, with an inline range from 1003–1224 and a cross line range from 109–351. In both surveys the inline and cross-line source and receiver spacings were approximately 25 m. Overlapping coverage between the two surveys covered an area of approximately 6 km by 6 km. Example inlines from both surveys are shown in Figure 2.3. The north-south oriented dashed line in Figure 2.1 shows the location of the selected inline 1084. In Figure 2.3, panel a shows inline 1084 from the baseline data while panel b shows inline 1084 from the time-lapse data. In both panels, red shading shows positive amplitude, and blue shading shows negative amplitude. The upper and lower green lines running sub-horizontally across both panels indicate the picked top and bottom of the Cranfield reservoir. Well CFU28-1 (28-1) is located at inline 1084, and the measured *Ip* from the well logs is included in both panels. Panels c and d show the amplitude spectra of the baseline and time-lapse surveys, respectively. In panels c and d, the x-axis shows frequency, and the y-axis show amplitude. In both surveys the dominant frequency is in the 20–40 Hz range. Assuming that the average *Vp* through the reservoir is 3 km/s, then for the dominant frequency of 25 Hz, the wavelength through the reservoir is 120 m.

Thus, the approximate resolution limit of the seismic data is 30 m. At the location of well F-1 the reservoir is approximately 30 m thick, while at well 28-1 the reservoir is less than 30 m thick and, therefore, thinner than the approximate resolution of the seismic data.

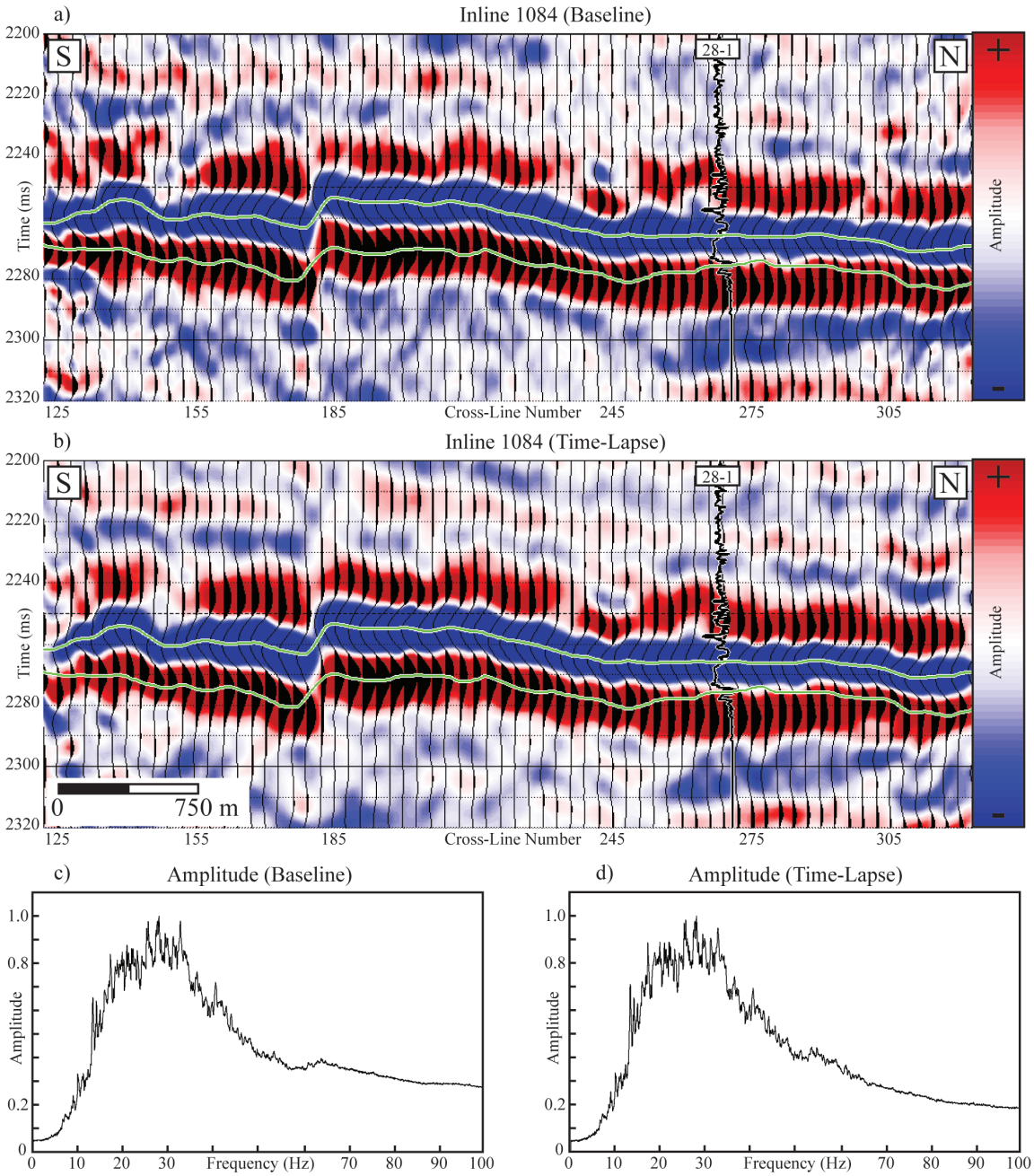

Figure 2.3: Panels a and b show the baseline and time-lapse seismic data, respectively, along inline 1084. In both panels, positive amplitudes are colored red, and negative amplitudes are colored blue. The interpreted top and bottom of the reservoir are shown by the upper and lower green lines, respectively. Well 28-1 is shown in both panels with the displayed log curve being *Ip*. The baseline and time-lapse amplitude spectra are shown in panels c and d, respectively. In panels c and d the vertical axis is amplitude, and the horizontal axis is frequency in Hertz.

Because of the depth of the Cranfield reservoir, the frequency range of the seismic data is insufficient to clearly resolve both the top and bottom of the reservoir. Figure 2.3a and b show that the top of the reservoir is a trough, and the base of the reservoir is usually the neighboring peak. However, in some areas the reservoir is thinner than a single trough to peak, particularly near cross-lines 270–300 in panels a and b. Panels a and b also illustrate that the amplitude of the reflection from the reservoir varies laterally. This variation indicates the presence of heterogeneities in the reservoir zone. The heterogeneities within the reservoir are more clearly visible in a horizon slice of the baseline data. Figure 2.4 shows the RMS amplitude extracted across the top of the Cranfield reservoir. In Figure 2.4, inline number is shown on the horizontal axis, and cross-line number is shown on the vertical axis. The two-way time range for this extracted horizon ranged from 2215 ms to 2294 ms. The amplitude is shown by color with red indicating larger absolute amplitude and blue indicating lower absolute amplitude. White dots indicate the location of wells 28-1 and F-1, and the dashed vertical line in the image is the location of inline 1084. The gray shading marks locations that are outside the coverage area of the survey. In Figure 2.4, the fault can be seen as a narrow low-amplitude feature running NW-SE in the southern half of the survey marked by the gray arrow. Additionally the amplitude variations over the field have been interpreted to be partially due to channelization features in the reservoir zone.

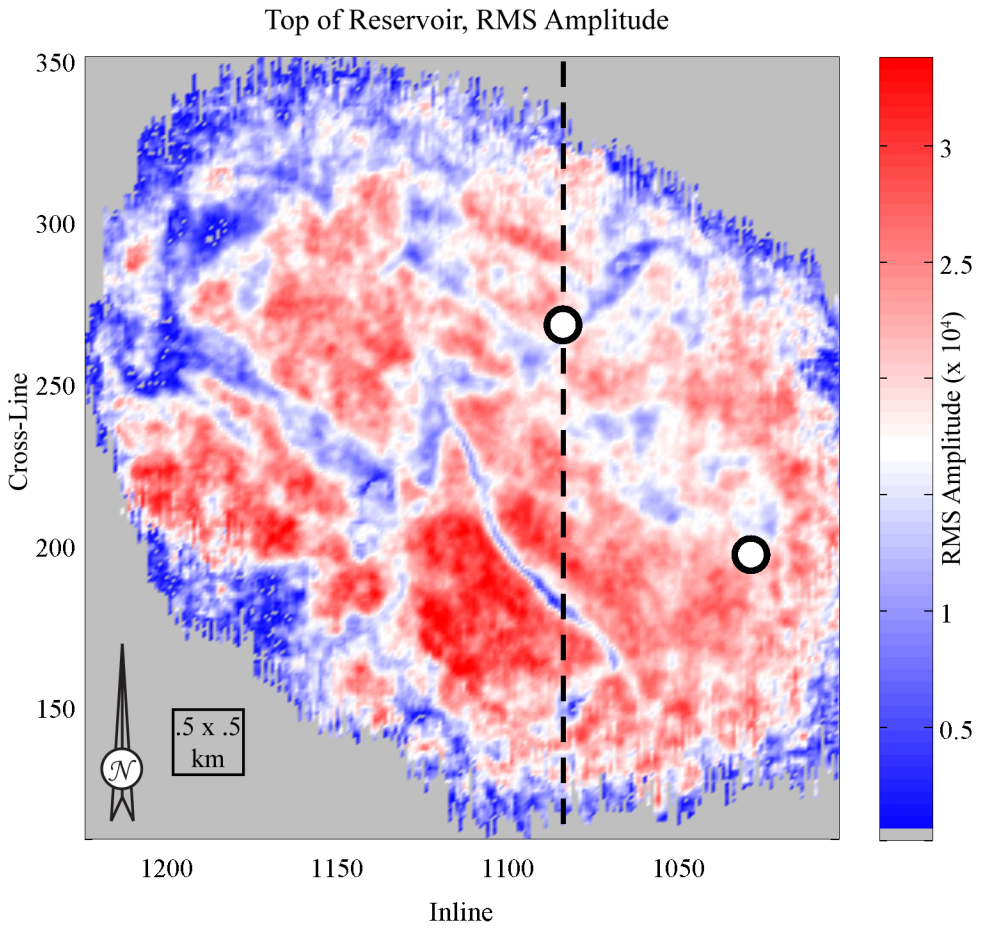

Figure 2.4: RMS smplitude extraction across the top of the reservoir (2215 ms to 2294 ms) with inline number shown on the horizontal (E-W) and cross-line shown on the vertical (N-S) axis. Red indicates larger RMS amplitudes and blue shows smaller RMS amplitudes. Inline 1084 is marked with the dashed vertical line. The white point on inline 1084 is well 28-1, and the other white point is the location if injection well F-1. A scale block is included with sides of 500 meters by 500 meters to clarify the dimensions of the figure.

2.2.2 Multicomponent 3D VSP Data

In addition to the two vintages of surface seismic data, a single vintage 3C 3D VSP dataset was available. The 3D VSP data was acquired around well F-1 in 2010, after approximately 2.2 tons of CO_2 had been injected into the reservoir over the whole study area. The seismic source for the 3D VSP was 5.5 lbs of dynamite per shot, located

at a depth between 30.5 and 36.5 m. For acquisition, 50 multicomponent geophones were clamped in well F-1 between the depths of 2407–3143 m with a geophone spacing of just over 15 m. A total of 893 shots comprised the VSP dataset. Because of the geometry of the VSP acquisition, the survey needed to be regridded to match the grid of the 3D surface seismic. After regridding, the 3D VSP had a PP reflection footprint that covered inline values ranging from 1000 to 1130 and cross-lines that ranged from 150 to 290. However, the reservoir was not imaged over this entire area. The 3D VSP survey was not designed for S-wave (horizontal component geophones) information. Therefore, the portion of the reservoir sampled by P-S S-wave reflections is significantly smaller than the portion of the reservoir imaged by P-waves (vertical component geophone). P-wave data is collected by an incident P-wave reflecting a P-wave (PP) while S-wave information is collected when an incident P-wave is mode converted at reflection and recorded as an S-wave (PS).

An example of the VSP P-wave data is shown in Figure 2.5. In Figure 2.5 calculated equivalent two-way travel time from the surface is shown on the vertical axis of panel a. The x-axis is marked with approximate inline number referenced to the surface seismic data with an inline spacing of 25 m. The interpreted top and bottom of the reservoir is shown by the upper and lower green lines, respectively, running across the figure. As expected, the 3D VSP contained higher frequencies for P-waves than the surface seismic data as shown by panel b of Figure 2.5. Panels b and c of Figure 2.5 show frequency on the horizontal axis and amplitude on the vertical axis. Panel b shows the frequency content of the vertical component P-wave data, and panel c shows the frequency content of the horizontal component S-wave data. Frequency content of the P-

wave information from the multicomponent 3D VSP has a dominant frequency in the 50–60 Hz range, nearly double that of the surface seismic information. This increase translates to a vertical resolution from the P-wave component of the 3D VSP that is better by a factor of two compared to the vertical resolution from the surface seismic data. Because of the increase in resolution compared to the surface seismic data, the top and bottom of the reservoir is clearly resolved in the VSP dataset and is interpreted as a trough and the following peak. Frequency content of the S-wave information is much lower than that of the P-wave information. However, due to the slower velocities of the S-waves, spatial resolution of the P- and S-wave information is comparable.

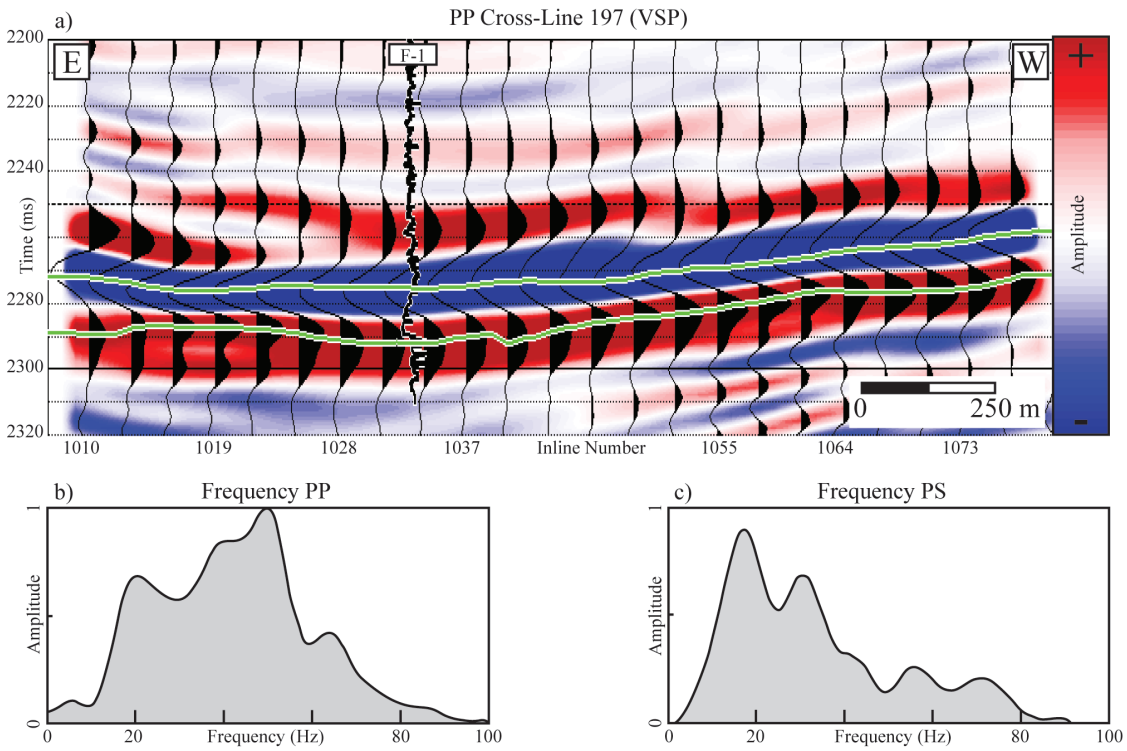

Figure 2.5: P-wave (vertical component geophone) component of cross-line 197 from the VSP. Panel a is colored to amplitude with red showing positive amplitude and blue showing negative amplitude. The vertical axis shows calculated two-way travel time with inline number shown on the horizontal axis. The included well log curve is *Ip* from well F-1. The top and bottom of the reservoir are shown by the upper and lower green lines, respectively. Panels b and c show frequency on the horizontal axis and amplitude on the vertical axis for the PP data and the mode-converted PS data, respectively.

2.2.3 Well Log Data

Well log data were available from the three wells within the DAS area. Open hole logs were present for wells F-2 and F-3 from the preinjection environment, and cased hole logs were available from after injection. Additional logs from well F-1 were available from before the injection started. In addition to logs from the wells within the DAS, some well logs were available from injection and monitoring wells located in the producing portions of the field. Of the available well logs, the logs from well 28-1 provided the most utility.

Available well log curves from the open-hole data included *Vp*, *Vs*, density, porosity, resistivity, and gamma ray (GR) among others. The *Vp*, *Vs*, porosity, and density logs were used to calibrate the rock-physics model. The resistivity logs from the two monitoring wells within the DAS study area (F-2 and F-3) were used to calculate baseline fluid composition and correct the porosity logs for in situ fluid composition. Before any of the measured curves were used or considered accurate, a complete analysis of the caliper logs was completed and used to edit all other logs. At depths where there was poor contact between the caliper tool and the borehole wall, the accuracy and reliability of the measured values was reduced. In spite of log editing, some uncertainty still remains in the measured data. Open-hole well logs from wells F-2 and F-3 are shown in Figures 2.6 and 2.7, respectively. In both figures, panels a, b, c, and d show GR, density, porosity, and sonic velocity, respectively. In panel d in both figures, the blue line is S-wave velocity, and the black line is P-wave velocity. In both figures, the reservoir zone has been highlighted in light gray in all panels. The Cranfield reservoir is identifiable from the surrounding shales by a decrease in GR count and the increase in porosity relative to the surrounding shales. Data from both wells F-2 and F-3 were used to calibrate the rock-physics model. Although there are some differences in the logs from wels F-2 and F-3 indicating lateral heterogeneity, the ranges of measured values from the two wells are similar, with *Vp* and *Vs* ranging from 3.1–3.6 km/s and 1.8–2.4 km/s, respectively, for well F-2. For well F-3 *Vp* ranges from 3.0–4.5 km/s while the range for *Vs* is 1.5–2.75 km/s. Similarly, measured density values for the reservoir zone is 2.2–2.6 g/cc for F-2 and 2.1–2.8 g/cc for F-3. Porosity, sonic, and density logs from wells F-1

and 28-1 were used to check the results of the inversion at later stages of this research, but they were not used in calibration of the rock-physics model.

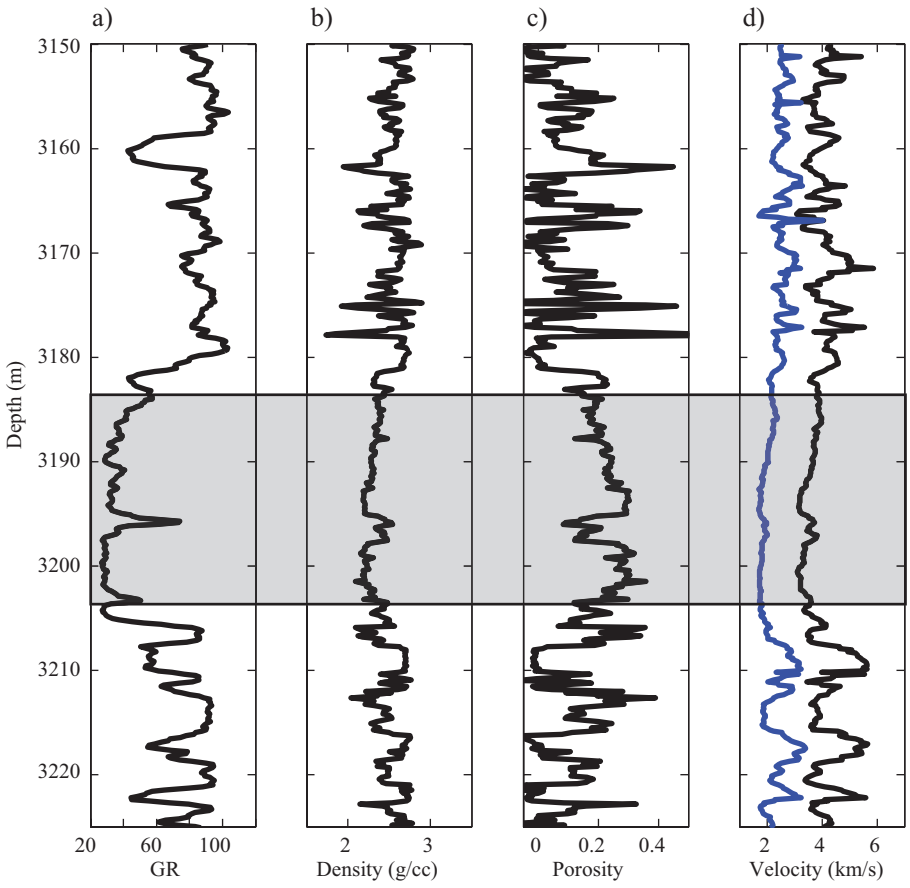

Figure 2.6: Open-hole logs from well F-2. Panel a shows the gamma ray log, panel b shows the density log, panel c shows the porosity log, and panel d shows sonic velocity logs. In panel d the blue line is the S-wave velocity, and the black line is the P-wave velocity. The light gray shading in all panels highlights the reservoir zone and is approximately 20 m thick.

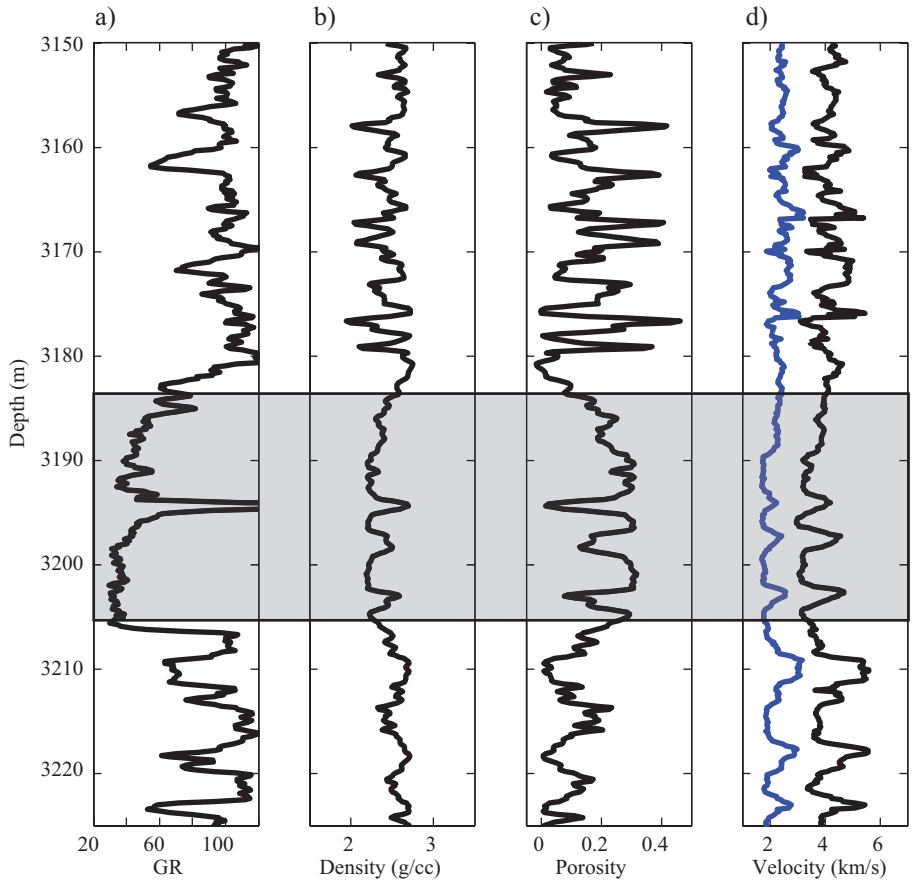

Figure 2.7: Measured well logs from well F-3. Panel a shows gamma ray count, panel b shows density in g/cc, and panel c shows porosity. Panel d shows the P-wave velocity in black and the S-wave velocity in blue. The approximately 20 m thick reservoir zone is shaded by the light gray overlay in all panels.

2.3 MINERAL AND PORE FLUID PROPERTIES

In rock-physics models, specifically contact-theory based rock-physics models, the effective moduli of the modeled materials is dependent on the moduli of the component minerals comprising the mineral grain, the grain contact cement, and the pore filling-fluid. The effective moduli of the different minerals, cement, and fluids used in this study are shown in Table 2.1. For certain minerals such as quartz and feldspar, the effective moduli are well known. For other minerals, specifically chamosite and chlorite,

which have been combined as a single clay term, the effective moduli at the temperatures and pressures of the Cranfield reservoir are known with much less certainty. Similarly, fluid moduli are well known for brine, but much less well known for CO_2 at different temperature and pressure conditions. Mineral properties shown in Table 2.1 are from Mavko et al. (2009). Properties shown for CO_2 are extrapolated from Wang (2000). The clay bulk modulus was calculated from a mixture of approximately 35% kaolinite and 65% chamosite. A shear modulus was not available for the chamosite component, so it was interpolated to give the clay mixture a bulk to shear modulus ratio similar to 'Gulf Clays' (Han et al., 1986 and Tosaya, 1982).

Table 2.1: Percentages of minerals used in the contact cement models.

Fluid/Mineral	Density (g/cm^3)	Bulk Modulus (GPa)	Shear Modulus (GPa)
Brine	1.045	2.2	0
CO_2	.675	.1275	0
Quartz	2.65	36	45
Clay	2.8	30.5	10.5
Feldspar	2.63	55	28
Muscovite	2.79	58	35
Calcite	2.71	71	36

Chapter 3: Methods and Techniques

This chapter provides a general outline and an introductory explanation of some of the geophysical techniques used in this dissertation. Presented here are explanations for amplitude variations with angle (AVA), used in Chapter 4, which is derived from the Zoeppritz (1919) equations. The contact cement model, which is used in Chapters 4, 5, and 6, is presented and explained. The model-based inversion (MBI) technique, as used in Chapter 5, is outlined. This chapter concludes with a discussion and brief overview of the statistical methods utilized and outlines the statistical approaches used in Chapters 4, 5, and 6.

3.1 AMPLITUDE VARIATIONS WITH ANGLE

Amplitude variations with angle, or as it is more commonly referred to as amplitude variations with offset, is the principle that the reflection and transmission coefficients of a wave depends on the velocity and density contrasts between two layers and the angle at which the incident wave contacts the interface. The relationship between the angle of incidence and the angle of reflection or transmission between two rays is given by Snell's Law (Equation 3.1).

$$p = \frac{\sin\theta p_1}{Vp_1} = \frac{\sin\theta p_2}{Vp_2} = \frac{\sin\theta s_1}{Vs_1} = \frac{sin\theta s_2}{Vs_2} \tag{3.1}$$

In Equation 3.1 p is the ray parameter (or horizontal slowness), θp_i and θs_i indicate angle of P- and S-waves, respectively. P- and S-wave velocities are given by Vp_i and Vs_i, respectively, and the 1 and 2 subscripts on all terms indicate the layer, with 1 being the

upper layer, indicating a reflected wave and 2 being the lower layer, indicating a transmitted wave. While the angle at which a wave is reflected or transmitted is fairly intuitive, the amplitudes of those reflected and transmitted waves is slightly less intuitive. The Knott-Zoeppritz equations (Knott, 1899 and Zoeppritz, 1919) can be used to calculate the amplitude of reflected and transmitted waves and non-normal angles of incidence. In The Knott-Zoeppritz equations, it is assumed that the material is linear-elastic and isotropic. Additionally, the equations assume that the propagating energy is in the form of a plane-wave. The Knott-Zoeppritz equations have been rewritten into a more convenient matrix form by Aki and Richards (1980). The full matrix components Aki and Richards form are shown in equations 3.2–3.5.

$$\begin{bmatrix} \grave{P}\acute{P} & \grave{S}\acute{P} & \acute{P}\acute{P} & \acute{S}\acute{P} \\ \grave{P}\acute{S} & \grave{S}\acute{S} & \acute{P}\acute{S} & \acute{S}\acute{S} \\ \grave{P}\grave{P} & \grave{S}\grave{P} & \acute{P}\grave{P} & \acute{S}\grave{P} \\ \grave{P}\grave{S} & \grave{S}\grave{S} & \acute{P}\grave{S} & \acute{S}\grave{S} \end{bmatrix} = R^{-1}P \tag{3.2}$$

In Equation 3.2, P and S indicate P and S-wave energy, respectively, while the ` and ′ accent marks denote down going and up going ray paths, respectively.

$$R = \begin{bmatrix} -sin\theta p_1 & -cos\theta s_1 & sin\theta p_1 & cos\theta s_2 \\ cos\theta_1 & -sin\theta s_1 & cos\theta p_2 & -sin\theta s_2 \\ 2\rho_1 Vs_1 sin\theta s_1 cos\theta p_1 & \rho_1 Vs_1(1-2sin^2\theta s_1) & 2\rho_2 Vs_2 sin\theta s_2 cos\theta p_2 & \rho_2 Vs_2(1-2sin^2\theta s_2) \\ -\rho_1 Vp_1(1-2sin^2\theta s_1) & \rho_1 Vs_1 sin2\theta s_1 & \rho_2 Vs_2(1-2sin^2\theta s_2) & -\rho_2 Vs_2 sin2\theta s_2 \end{bmatrix} \tag{3.4}$$

$$P = \begin{bmatrix} sin\theta p_1 & cos\theta s_1 & -sin\theta p_1 & -cos\theta s_2 \\ cos\theta_1 & -sin\theta s_1 & cos\theta p_2 & -sin\theta s_2 \\ 2\rho_1 Vs_1 sin\theta s_1 cos\theta p_1 & \rho_1 Vs_1(1-2sin^2\theta s_1) & 2\rho_2 Vs_2 sin\theta s_2 cos\theta p_2 & \rho_2 Vs_2(1-2sin^2\theta s_2) \\ \rho_1 Vp_1(1-2sin^2\theta s_1) & -\rho_1 Vs_1 sin2\theta s_1 & -\rho_2 Vs_2(1-2sin^2\theta s_2) & \rho_2 Vs_2 sin2\theta s_2 \end{bmatrix} \tag{3.5}$$

In Equations 3.4 and 3.5, the variables and subscripts are the same as those for Equation 3.1, with the addition of ρ_i being density. Despite the more computationally efficient matrix form proposed by Aki and Richards (1980), the equations are still not intuitive concerning the information contained in angle-dependent reflectivity. The Aki and Richards (1980) approximate equations show that AVA effects are a function of changes in *Vp*, *Vs* and ρ across an interface. A more intuitive approach to AVA can be given by examining some of the linearized approximations of the full Knott-Zoeppritz equations. The Bortfeld (1961) and the later Shuey (1985) approximations are shown here. The Bortfeld approximation is given in equation 3.6, and the more popular Shuey approximation and its components are given in 3.7–3.10.

$$Rpp(\theta p_1) \approx \frac{1}{2}\ln\left(\frac{Vp_2\rho_1 cos\theta p_1}{Vp_1\rho_2 cos\theta p_2}\right) + \left(\frac{\sin\theta p_1}{Vp_1}\right)^2 (Vs_1^2 - Vs_2^2)\left[2 + \frac{\ln(\rho_1/\rho_2}{\ln(Vs_2/Vs_1)}\right] \tag{3.6}$$

$$Rpp(\theta p_1) \approx Rp_0 + Bsin^2\theta p_1 + \frac{1}{2}\frac{\Delta Vp}{\overline{Vp}}(tan^2\theta p_1 - sin^2\theta p_1) \tag{3.7}$$

$$Rp_0 \approx \frac{1}{2}\left(\frac{\Delta Vp}{\overline{Vp}} + \frac{\Delta\rho}{\overline{\rho}}\right) \tag{3.8}$$

$$B = C - 2(1 + C)\left(\frac{1-2\overline{\sigma}}{1-\overline{\sigma}}\right) \tag{3.9}$$

$$C = \frac{\frac{\Delta Vp}{\overline{Vp}}}{\frac{\Delta Vp}{\overline{Vp}} + \frac{\Delta\rho}{\overline{\rho}}} \tag{3.10}$$

The variables and subscripts in equation 3.6–3.10 are the same as those listed in equations 3.1–3.4, with the addition of Poisson's ratio, σ. These approximations assume that the contrast in *Vp*, *Vs*, σ, and ρ are small and the angle of incidence is small, typically less than 30 degrees. Furthermore, at angles of incidence (θp_1) close to zero, the first portion of both the Bortfeld (Equation 3.6) and Shuey (Equation 3.7) equations is the primary component of the P-wave reflection coefficient (*Rpp*). In the Bortfeld approximation (Equation 3.6) as θp_1 increases, the first term in the approximation is minimized, and the second term, which is a function of sin θp_1 is maximized, increasing the contribution of the shear velocity and the density contrasts to the reflection coefficient. Similarly in the Shuey approximation (Equation 3.7), it is evident that at intermediate angles of incidence, the reflection coefficient is largely a function of Poisson's ratio. The final term of Equation 3.7 is solely a function of *Vp* and is maximized at large (greater than 30 degrees) angles of incidence when the other two terms contribute nominally. When wide-angle reflection coefficients can be used in conjunction with near-angle reflection coefficients, it is possible to obtain some estimates of the density of the medium. This density estimate is possible because the wide -angle coefficients are a function of *Vp* while the near-angle reflection coefficients are a function of *Vp* and ρ. However, post-critical reflections inhibit stable estimates of density.

3.2 CONTACT CEMENT MODEL

Contact-theory models are a subset of rock-physics models that are based on the assumption that the elastic moduli of a rock are related to the moduli of the individual grains, the number of grain contacts in the grain packing, and the stiffness and amount of cement that is present at grain contacts (Dvorkin et al., 1994 and Dvorkin and Nur, 1996).

The contact cement model, used in this study, is derived from Hertz-Mindlin theory (Mindlin, 1949). During the derivation of the contact cement model, a grain contact cement term was included in the model. However, the pressure term of the model was ultimately dropped. Because the inclusion of cement between two grains under compression reduces to a linear integral regression where the stiffness of the cemented grains does not depend on confining pressure (Dvorkin et al., 1991). Thus the pressure term cancels from the equations. The model provides closed-form solutions where the porosity of the rock varies inversely with the amount of contact cement because cement is being deposited in the existing pore-space of the rock frame. A complete list of the equations that comprise this model can be found in Appendix A. Cement in this model can be deposited in two different ways as shown with the solid and dashed lines in Figure 3.1. The first method, the method used in this dissertation, is to deposit the cement evenly and concentrically around each grain. This depositional geometry corresponds to the dashed line of Figure 3.1. The second method of cement formation is that cement is deposited only at grain contacts. The solid line of Figure 3.1 illustrates this depositional geometry. This study used the method of cement deposition where cement coats each grain concentrically (dashed line Figure 3.1).

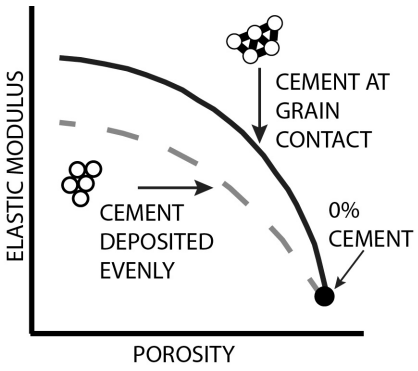

Figure 3.1: A schematic of the contact cement model. Cement can be deposited concentrically around the grain following the lower line on the graph or only at grain contacts, following the upper line on the graph. As cement content increases, porosity decreases, and the elastic moduli increase.

3.3 MODEL-BASED SEISMIC INVERSION

Seismic inversion is a tool that is used to help interpret seismic information. Inversion of seismic data is accomplished by converting measured reflection coefficients into the elastic properties of the reservoir. The calculation of elastic properties from reflection coefficients is accomplished by minimizing the difference between modeled data and observed data (Sen, 2006). The elastic properties most commonly inverted from seismic data are P- and S-impedance. Model-based inversion (MBI), using the convolutional forward operator, is one of the most commonly used approaches to invert seismic data due to its efficiency and effectiveness (Rowbotham et al., 2003 and Hampson et al., 2005). In convolution based MBI the forward model is compiled by convolving a wavelet, extracted from the surface seismic data, with a simple model of the pre-defined geology, usually developed from interpretation of seismic horizons. After convolution of the wavelet with the model, the misfit between the initial model and the data is calculated, and the model is updated to reduce the misfit. As the model is updated, the synthetic result starts to converge with the measured data. The final model of

impedance is generated when the misfit between the synthetic result and the measured data is minimized. In situations such as those presented in Chapter 5, where both P- and S-wave data are inverted for P- and S-impedance, respectively, a joint inversion is completed. In a joint inversion the initial model is updated to simultaneously minimize the difference between the convolution of the P-wavelet with the model to the P-wave data and the convolution of the S-wavelet with the model to the S-wave data.

3.4 STATISTICAL METHODS

Statistical methods are used in seismic interpretation to help account for uncertainty, provide a range of equi-probable outcomes, and to integrate different types of data such as surface seismic information and well log information (Avseth et al., 2005 and Rowbotham et al., 2003). Statistical methods have been shown by many to produce quality results that extend beyond the limits imposed by purely deterministic approaches and are a primary component of quantitative interpretation methods (Hass and Dubrule, 1994; Mukerji et al., 2001; and Eidsvik et al., 2002). In this study multiple different statistical approaches are used to examine the range of probable outcomes (Chapter 4), the differences between datasets (Chapter 4), and the uncertainties and probabilities associated with the outcomes (Chapters 5 and 6).

The approach used in Chapter 4 to analyze the range of possible outcomes is based on a Monte Carlo estimate. In the Monte Carlo estimation of AVA, the AVA parameters are calculated from two randomly selected depth points taken from the well logs. The first depth point is randomly selected from a depth range above the reservoir, and the second depth point is randomly selected from a certain range within the reservoir. By computing the AVA signatures many hundreds of times with randomly selected

velocity and density values, the range of possible outcomes, as well the probability of each outcome, can be estimated.

Later in Chapter 4, statistical methods are used to differentiate between two data classes. To do this, bivariate probability density functions (PFDs) were generated to represent different fluid saturations. A comparison of the two different PDFs at the location of the parent data provides information regarding how different they are and the extent to which it is possible to differentiate between them. The parent data for each PDF is mapped back to a pair of PDFs, and each data point is associated with the PDF that has the highest probability at that given point. The success rate at which parent data is mapped to its daughter PDF quantifies the ability to differentiate between two different datasets. This result informs the choice of elastic parameters for use in later parts of the study.

In Chapter 5 a statistical approach is used to estimate porosity and fluid saturation within the reservoir while in Chapter 6 a slightly modified approach is used to estimate the single parameter of porosity. In both Chapters 5 and 6, prior distributions of porosity, mineralogy, and fluid saturation are used as inputs into the contact cement model. The prior distributions used in Chapters 5 and 6 are shown by the marginal PDFs 3.11–3.13.

$$P(\phi) \tag{3.11}$$

$$P(min) \tag{3.12}$$

$$P(S_{CO2}) \tag{3.13}$$

The prior distributions are marginal probability density functions of porosity ($P(\phi)$), mineralogy ($P(min)$), and CO_2 saturation ($P(S_{CO2})$). The prior distributions 3.11–3.13 were selected to contain all expected ranges of each unknown within the Cranfield reservoir interval.

From the prior distributions I was able to examine the probability of a given porosity and fluid saturation given initial ranges of elastic properties from the inverted data. This is shown by the conditional PDF expression (Equation 3.14).

$$P(\phi, fl | a < Ip < b, c < Vp/Vs < d) \tag{3.14}$$

A conditional PDF is a PDF that has been constrained by a range of related parameters. Equation 3.14 is read as the joint probability of ϕ and *fl* given *Ip* and *Vp/Vs*. In the conditional PDF (3.14) ϕ is porosity, *fl* is fluid saturation, *Ip* is P-impedance between the range of *a* and *b*, and *Vp/Vs* is the ratio of P-wave velocity to S-wave velocity over the range of *c* and *d*. In chapter 6 this probability is simplified to the conditional PDF (Equation 3.15).

$$P(\phi | a < Ip < b) \tag{3.15}$$

In this simplification, the probability of porosity (ϕ) is determined solely from a range P-impedance (*Ip*) values. To generate the relationship from the rock-physics model, only the prior distributions of porosity and mineralogy were used as model inputs. By using

the stochastic relationships from the rock-physics model instead of a strictly deterministic approach, uncertainty and variability can be constrained to a higher degree.

Chapter 4: Sensitivity Analysis of Tuscaloosa Sandstones to CO_2 Saturation, Cranfield Field, Cranfield MS[1]

4.1 ABSTRACT

The study of the seismic response of reservoirs partially saturated with injected CO_2 is important because it will improve monitoring and characterization of sites used for CO_2 utilization and storage. I investigated the sensitivity of the seismic properties to CO_2 saturation of the Cranfield injection site using rock-physics modeling, fluid substitution, amplitude variations with angle (AVA), and statistical classification. Rock-physics models quantitatively linked the elastic properties to variations of CO_2 saturation, lithology, and cement content. I modeled velocity and density logs with different fluid compositions. With seismic properties corresponding to these different fluid compositions, I computed 1) AVA responses through Monte Carlo simulations and 2) probability density functions to use for statistical classification. Rock-physics modeling indicated that the reservoir was a stiff cemented sandstone. Consequently, AVA analysis illustrated that the stiff reservoir tended to dominate the seismic response. The statistical classification scheme successfully differentiated between CO_2 and brine saturation, with the ratio of compressional wave velocity to shear wave velocity (*Vp/Vs*) used as the discerning parameter. Accordingly, these seismic-based tools, when applied to relatively high-resolution data, showed the sensitivity of the elastic properties of the Cranfield reservoir to modeled changes of CO_2 saturation.

[1] This chapter is based on the publication: Carter, R.W. and Spikes, K.T., 2013, Sensitivity analysis of Tuscaloosa sandstones to CO_2 saturation, Cranfield field, Cranfield, MS: International Journal of Greenhouse Gas Control, **18**, 485-496. Dr. Spikes provided technical guidance and editing.

4.2 INTRODUCTION

Sequestration of CO_2 within subsurface geologic formations is a technology that could potentially help to reduce the amount of anthropogenic CO_2 released into the atmosphere. Recent studies have shown that brine-saturated reservoirs and depleted hydrocarbon reservoirs can store large quantities of CO_2. Various sites have shown this potential including the Sleipner, Norway (Ghaderi and Landrø, 2009), Weyburn, Canada (Ma and Morozov, 2010 and Verdon et al., 2010), and Otway, Australia projects (Dodds et al., 2009 and Urosevic et al., 2010). An important aspect of CO_2 sequestration is to monitor the volume and location of the fluid during and after injection to ensure that the CO_2 remains in place. Geophysical techniques, in particular surface seismic methods, could potentially contribute to this monitoring capability over spatial areas not sampled by observation or injection well bores. When used in a time-lapse manner and linked quantitatively to the reservoir and fluid properties, seismic data potentially can be used to map the lateral extent of the injected fluid.

Quantitative seismic interpretation techniques have been used successfully to detect and characterize hydrocarbon reserves (e.g., Bosch et al., 2009; Russell et al., 2003; and Avseth and Norunn, 2011). These methods include fluid substitution and AVA, more commonly referred to as AVO, among others. Conventional fluid substitution work has focused primarily on modeling elastic properties and seismic data subject to different fluid-saturation scenarios to help distinguish between brine and hydrocarbon reservoirs (Das and Batzle, 2008; Artola and Alvarado, 2006). Signatures of AVA have proven useful as a proxy in identifying natural gas and have been organized into different classes of gas-saturated sandstones (Rutherford and Williams, 1989; Castagna et al., 1998; and Simm et al., 2000). Although these methods are useful for

analyzing the response of seismic data to pore fluid types, injected CO_2 has very different physical properties than do both liquid and gas hydrocarbons when contained within reservoirs. Accordingly, it is quite important to understand how sequestered CO_2 affects the elastic parameters of reservoirs into which it is injected. My work here assesses the sensitivity of the elastic properties of the Cranfield reservoir to changes in CO_2 saturation using several quantitative seismic-based techniques.

Geophysical research pertaining to CO_2 injection and monitoring includes a wide range of topics. Siggins et at. (2010) compared laboratory ultrasonic velocities of CO_2-saturated core plugs to synthetic saturated sandstones from the Otway project for a wide range of pore pressures. This work concluded that replacing methane in the gas cap with CO_2 might not be observable from surface seismic measurements. However, replacing brine in a formation with CO_2 should produce a change in impedance that is measurable with surface seismic techniques. Additionally, high-frequency velocity measurements of CO_2-saturated core plugs from the Cranfield F-1 well were examined under a range of confining pressures by Joy (2011). Joy (2011) found that the elastic wave velocities were approximately linearly proportional to the differential pressure of the sample. In addition, changes in the pore structure and the cementation of the samples resulted from injecting CO_2 dissolved in brine. Lumley (2010) examined the feasibility of time-lapse seismic monitoring of CO_2 saturation by looking at the fluid properties of CO_2 as a function of temperature, pressure, and saturation. The same study also helped to bridge the scale gap between laboratory-scale experiments and field-scale studies. This work concluded that the challenges to time-lapse monitoring of CO_2 include repeatability, CO_2-

rock interactions, in situ CO_2 properties, pressure changes, and non-linear and non-unique responses of seismic waves to CO_2 saturation.

Research has been completed that focuses on CO_2 monitoring and detection involving surface seismic data. Ghaderi and Landrø (2009) examined time-lapse reflection amplitude and travel-time shifts to estimate thickness and velocity changes in the Sleipner field. They found that when combined, time-lapse (4-D) amplitude and time shifts could be used to discriminate between changes in thickness and changes in velocity in CO_2 layers in sand beds. Chadwick et al. (2010) quantitatively analyzed multiple vintages of data from the Sleipner field. They applied a prestack stratigraphic inversion algorithm and compared it to poststack inversion methods. Prestack inversion of seismic reflection data better characterized thin intra-reservoir mudstone and sand layers compared to using poststack inversion. More recently, Daley et al. (2011) compared modeled and measured cross-well seismic data to estimate properties of an injected CO_2 plume at the Frio-II project and generated updated flow models from the relatively high-resolution cross-well seismic observations.

The study presented here combines rock-physics modeling, fluid substitution, AVA, and statistical classification to differentiate between brine- and CO_2-saturated zones in the Cranfield reservoir located in Cranfield, MS. Rock-physics modeling related the reservoir zone lithology, porosity, and cement content to elastic parameters. We employed Gassmann (1951) fluid substitution to model the reservoir using multiple fluid mixing schemes and fluid compositions. For the AVA analysis, we modeled a shale-sandstone interface. The underlying sandstone was varied according to the fluid-substitution modeling, which allowed analysis of the angle-dependent reflectivity as a

function of saturation. The classification scheme compared modeled data to pairs of probability density functions (PDFs) to determine which class had the highest probability of occurrence for each datapoint. Importantly, the method of fluid mixing and the corresponding *Vp/Vs* played important roles in the classification.

4.3 THEORY AND METHODS

This study was a multi-step procedure that integrated rock-physics modeling, fluid substitution, AVA analysis, and statistical classification. Rock-physics modeling linked reservoir properties to elastic parameters. The fluid substitution showed the sensitivity of the reservoir elastic properties to saturation changes. Closely linked to the fluid substitution was the AVA analysis, which examined the sensitivity of the seismic response across the interface to fluid-saturation variations. Statistical classification was performed on the results from the fluid substitution. The results from the statistical classification indicated which combinations of elastic properties within the reservoir interval provided the best discrimination among different CO_2-brine mixtures.

For this study, well log data from well F-2 was used. Well F-2 is located approximately 69 m down dip from the injection well F-1. Selected logs from the well F-2, acquired before injection, are shown in Figure 4.1. Panels a, b, and c show *Vp*, *Vs*, and gamma ray logs, respectively. These logs contain the reservoir and shales above and below the reservoir. The blue line shows shales, the red corresponds to the upper reservoir zone from about 3183–3194 m, and the green overlay indicates the lower reservoir zone at approximately 3196–3202 m. The increase in the gamma ray count at about 3186 m indicates that a local shale layer divides the upper and lower reservoir intervals and is indicated in blue at that depth in Figure 4.1.

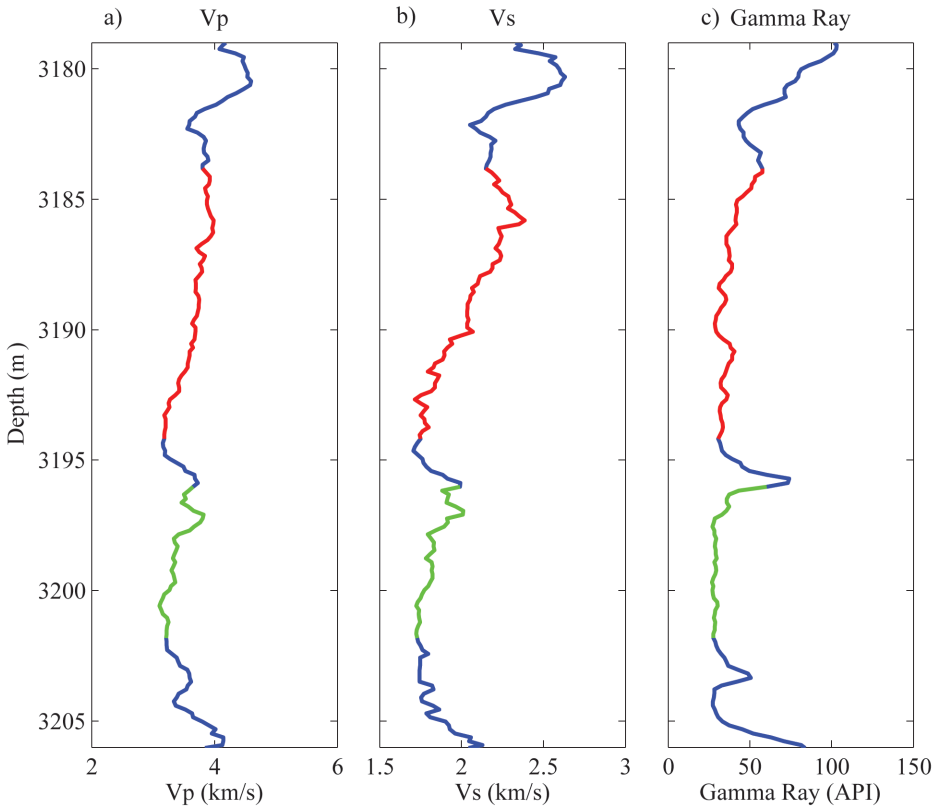

Figure 4.1: Data from the monitoring well F-2, including P-wave velocity (panel a), S-wave velocity (panel b), and gamma ray count (panel c). The red line shows the shallower reservoir zone, which extends from about 3184–3194 m, and the green line shows the deeper reservoir zone, which extends from about 3195–3202 m, and blue indicates shale. The local shale layer that divides the two reservoir zones is apparent from the increase in the gamma ray count between 3194–3197 m.

4.3.1 Rock-Physics Modeling

Rock physics is the study of the relationships between reservoir properties such as porosity, lithology, pore fluid, and cementation (among others) and the elastic properties (P- and S-wave velocities or elastic moduli). Numerical, analytical, or empirically derived rock-physics models transform reservoir properties to the elastic properties. Many models exist, but only a select few typically are applicable for a given reservoir. For this study we divided the Cranfield reservoir into two layers based on the gamma ray

log. For the shallower portion of the reservoir we used a contact-theory model. For the deeper portion of the reservoir, a model based on the Hashin-Shtrikman (1963) bounds was used.

Contact-theory models represent a sandstone reservoir as a pack of identical spheres under varying pressure, mineralogical, fluid, and cementation conditions (Dvorkin and Nur, 1996; Avseth et al., 2000). The upper portion of the Cranfield reservoir consists of cemented sandstone (Lu et al., 2012a), which makes the cemented sandstone contact-theory model the most appropriate. In this model, cement can be deposited in two ways (Figure 4.2a). First, cement can form along grain contacts (dark blue line); second, it can be deposited evenly around the grain surface (light blue line). For both methods, as cement volume increases, porosity of the sand pack decreases, and the overall stiffness of the rock frame increases. For this study we used the cementation method corresponding to a uniform and concentric deposition of cement around the grains to model the portion of the Cranfield reservoir from 3184–3194 m.

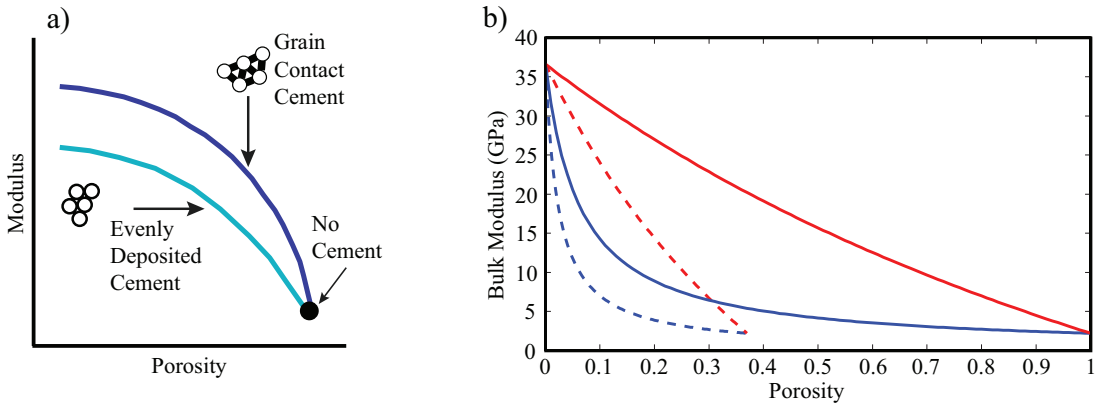

Figure 4.2: Panel a shows a schematic of the contact cement model. Cement can be deposited concentrically around the grain following the lower path on the graph or only at grain contacts, following the upper line on the graph. As cementation increases, porosity decreases, and the elastic moduli (bulk and shear moduli) increase. Panel b shows Hashin-Shtrikman (solid) and modified Hashin-Shtrikman (dashed) bounds. The Hashin-Shtrikman bounds describe mixing of two materials as an isotropic combination of concentric spheres. They are the narrowest set of theoretical bounds for mixing two materials in terms of elasticity. The lower modified bound can be used to represent a sorting trend. The high porosity point is based on critical porosity, which is the maximum porosity that can be achieved while still having all grains in contact with other grains. This high porosity point represents a well-sorted mixture with deteriorating sorting as porosity decreases.

The lower interval of the reservoir, 3195–3202 m, is interpreted to be a sandstone with poor to well sorted variations. To model this sorting trend, we implemented a theoretical bound, namely, the lower modified Hashin-Shtrikman bound, which accommodates a critical porosity component for fluid-saturated granular material. Hashin-Shtrikman bounds are a way of mixing materials of different stiffnesses: either different mineral phases or a solid and a fluid. In Figure 4.2b, the upper bound (solid red line) represents the solid material coating a spherical core of fluid. The lower bound (solid blue line) represents the reverse situation, in which the fluid concentrically coats

the mineral grain. These bounds correspond to a mixture of quartz and brine. The two lines meet at the zero porosity mineral point (upper left) and at the 100% porosity point (lower right). Modified Hashin-Shtrikman bounds (dashed lines Figure 4.2b) are Hashin-Shtrikman bounds normalized to a critical porosity value. These bounds can be used to model velocities of unconsolidated sediments at depth (e.g., Blangy et al., 1993), where critical porosity is the highest possible porosity when grains are in contact with other grains. Loosely consolidated grains, with porosity greater than the critical porosity, tend to behave as if in a suspension and do not show significant changes in elastic moduli with respect to relatively large changes in porosity (Avseth et al., 2005). A lower modified Hashin-Shtrikman bound also provides a heuristic approach to interpret sorting trends (Avseth et al., 2005). The interpretation is that low porosity represents poorly sorted material with a range of grain sizes partially filling the pore space between the larger grains. High porosity represents well-sorted material, with open pore space between equivalently sized grains.

4.3.2 Fluid Substitution

Fluid substitution provides a way to calculate the bulk modulus of a porous rock saturated with any known pore fluid. The Biot-Gassmann equations (Gassmann, 1951; Biot, 1956) provide the basis for this method. Equation 4.1 relates the different bulk moduli of the rock under examination, and Equation 4.2 demonstrates the assumption that the shear moduli are equivalent in the saturated and dry cases.

$$\frac{K_{dry}}{K_0 - K_{sat}} = \frac{K_{dry}}{K_0 - K_{dry}} + \frac{K_{fl}}{\phi(K_0 - K_{fl})} \tag{4.1}$$

$$\frac{1}{\mu_{dry}} = \frac{1}{\mu_{sat}} \tag{4.2}$$

In these equations, K_{dry} is the dry rock bulk modulus, K_{sat} is the saturated rock bulk modulus, K_0 is the bulk modulus of the mineral phase of the rock, and K_{fl} is the bulk modulus of the pore fluid. These equations result in accurate calculations, provided that the following three criteria are met. A homogeneous mineral modulus exists, the rock is isotropic, and low frequency is used to maintain pore-pressure equilibrium (Gassmann, 1951).

Equations 4.3 and 4.4 relate equations 4.1 and 4.2 to the compressional (Vp) and the shear wave (Vs) velocities. For the fluid substitution portion of this study, reformulations of Equation 4.1 were used, solving for K_{dry} (Equation 4.5) and K_{sat} (Equation 4.6).

$$Vp = \sqrt{\frac{K+\frac{4}{3}\mu}{\rho}} \tag{4.3}$$

$$Vs = \sqrt{\frac{\mu}{\rho}} \tag{4.4}$$

$$K_{dry} = \frac{K_{sat}(\phi K_0/K_{fl}+1-\phi)-K_0}{(\phi/K_{dry})(1/K_0-1/K_{fl})+(1/K_0)(1/K_0-1/K_{dry})} \tag{4.5}$$

$$K_{sat} = \frac{\phi(1/K_0-1/K_{fl})+1/K_0-1/K_{dry}}{(\phi/K_{dry})(1/K_0-1/K_{fl})+(1/K_0)(1/K_0-1/K_{dry})} \tag{4.6}$$

To determine the fluid substituted K_{sat} value corresponding to a particular fluid, the stiffness of that fluid (K_{fl}) must be provided. Moduli of fluid mixtures can be calculated using the Voigt (1907) bound, representing patchy saturation, or the Reuss (1929) bound, representing uniform saturation (Knight and Nolen-Hoeksema, 1990). The Voigt bound is an arithmetic average of the moduli of two or more fluids and results in

the least compressible possible mixing of the constituent fluids. The Reuss bound is a harmonic average of the fluid moduli and represents the softest way of mixing two or more fluids. Table 2.1 contains the moduli and density of the fluids used in this study. The properties for CO_2 were interpolated from measured values (Wang, 2000) for a pore pressure of 30 MPa and a temperature of approximately 100° C. This temperature and pressure combination causes the CO_2 to be in the supercritical phase. These were approximate reservoir conditions during injection (Lu et al., 2012a). Values of K_{fl} corresponding to a range of brine and CO_2 percentrages were used in the Gassmann equations. These included 100% CO_2 and 100% brine as well as intermediate compositions of 25, 50, and 75% CO_2, with the remaining proportion consisting of brine in each case.

4.3.3 Amplitude Variations With Angle

Signatures of seismic AVA responses have proven useful in differentiating fluid compositions (Rutherford and Williams, 1989; Castagna et al., 1998; and Simm et al., 2000). The Knott-Zoeppritz (Knott, 1899; Zoeppritz, 1919) equations describe how reflection coefficients change as a function of incidence angle for a two layer problem. These original equations have since been modified and linearized as in Aki and Richards (1980) and Shuey (1985). Effects of AVA are a function of P-impedance (*Ip*), S-impedance (*Is*), and density across the interface of the two-layer or half-space problem model. At relatively small angles (0–10°), seismic amplitude is primarily a function of *Ip*. As the angle of incidence increases, the seismic amplitude becomes primarily a function of *Ip/Is* and density.

Each layer in the AVA model must be assigned a value of *Vp*, *Vs*, and density. These values can come from different data types including core plug velocity measurements, but they most often come from averages of well log sonic and density measurements. The AVA result from a single set of velocities and density measurements is a single set of angle-dependent reflection coefficients. However, using averages for each layer does not account for variations within each individual. Furthermore, it does not provide a reliable representation of the interface between the two layers because the difference in average values of two layers rarely represents the change in properties across an interface (Bosch et al., 2007). To account for the variability in the elastic properties, we used a Monte Carlo simulation to estimate the range of reflection coefficients that could be expected between the overlying shale and the reservoir. This technique returns a range of possible outcomes and allows for the probability of each outcome to be determined. This range of outcomes can be related to variations in the rock properties such as fluid saturation.

The Monte Carlo simulation was performed on well data scaled up to the seismic scale using the Backus (1962) average. The Backus (1962) average is the long-wavelength approximation of a seismic wave propagating through a series of thin layers. When applied to log data as a running average over a specific window size, it provides the seismic velocity at the resolution expected from surface seismic data. We used specific window sizes so that the frequency of the upscaled data was similar to the dominant frequency of the seismic (20–40 Hz) and 3D VSP (50–60 Hz) data acquired at the Cranfield site. For the Monte Carlo simulation we varied the location of the interface between the shale layer and the reservoir over a range of 6 meters. Shifting the shale-

reservoir interface was necessary because of the lack of a definitive and resolvable interface in the upscaled data. Two hundred simulations were run for each of the 20 different half-space models generated by shifting the shale-reservoir interface. In total, 4000 simulations were computed. The same number (4000) of simulations were computed for the five fluid compositions mentioned in the fluid substitution step.

Each simulation included a random selection of a single depth from both the overlying shale zone and from the reservoir zone. The AVA response was computed from the velocities and densities associated with each selected depth. We ran the simulations for each different fluid composition of 0, 25, 50, 75, and 100% CO_2 and for the two different schemes of fluid mixing (Voigt and Reuss). We calculated the AVA response using the full Zoeppritz equations for incidence angles from 0–30 degrees. For each fluid composition, a bivariate PDF was calculated from the 4000 simulations. Those PDFs indicate the probability of a reflection coefficient value occurring at a given angle of incidence for a certain pore-fluid composition.

4.3.4 Classification

Synthetic velocity and density logs calculated using fluid substitution were used to generate crossplots for various combinations of *Vp*, *Vs*, *Ip*, *Is*, *Vp/Vs* and density. I chose these various pairs of elastic properties because they represented a wide range of parameter combinations and because they can be extracted from well logs and from offset surface seismic and VSP data. A bivariate PDF was computed for each crossplot. These PDFs were used to classify the data in terms of pore fluids.

An important element of this procedure was the determination of the classification success rate for each pore fluid, where each different pore fluid corresponds to a class.

For this study, the success rate was defined as the number of correctly classified points divided by the known number of points in that class. Classification success rates were calculated by mapping both the measured well log and modeled data back to the their respective bivariate PDFs and a comparison PDF from a different fluid class. Each data point was mapped to the PDF that showed the highest probability at the location of the data point.

Three parameter combinations showed the highest success rates for all different fluid combinations. These combinations were *Vp/Vs* to *Ip*, *Vp/Vs* to *Vs* and *Vp/Vs* to *Vp*. The fluid compositions compared were 0% and 100%, 0% and 25%, 0% and 50%, and 0% and 75% CO_2. The different CO_2 concentrations were also tested against measured well log data. When an equal probability occurred of a data point belonging to either class, the data point was mapped to both. However, if probability in both PDFs was zero, the data point was mapped to neither class. These two situations were present in each classification procedure and affected the success rates.

4.4 RESULTS

4.4.1 Rock-Physics Modeling

Modeled trend lines relating *Vp* and porosity from the contact cement model (Dvorkin and Nur, 1996) can be seen in Figure 4.3, representing the depth range 3184–3194 m. The red, green, and blue lines represent different simulated grain compositions. Complete mineral compositions for the red, green, and blue lines are in Table 4.1, and the mineral moduli used are in Table 2.1. The calibrated models are important because they can enable extrapolating properties of the reservoir away from the locations of well control by varying the model parameters. Altering porosity, cement, and mineral

composition in the model can be a way to characterize reservoir parameter variations in between wells using surface seismic and/or 3D VSP data.

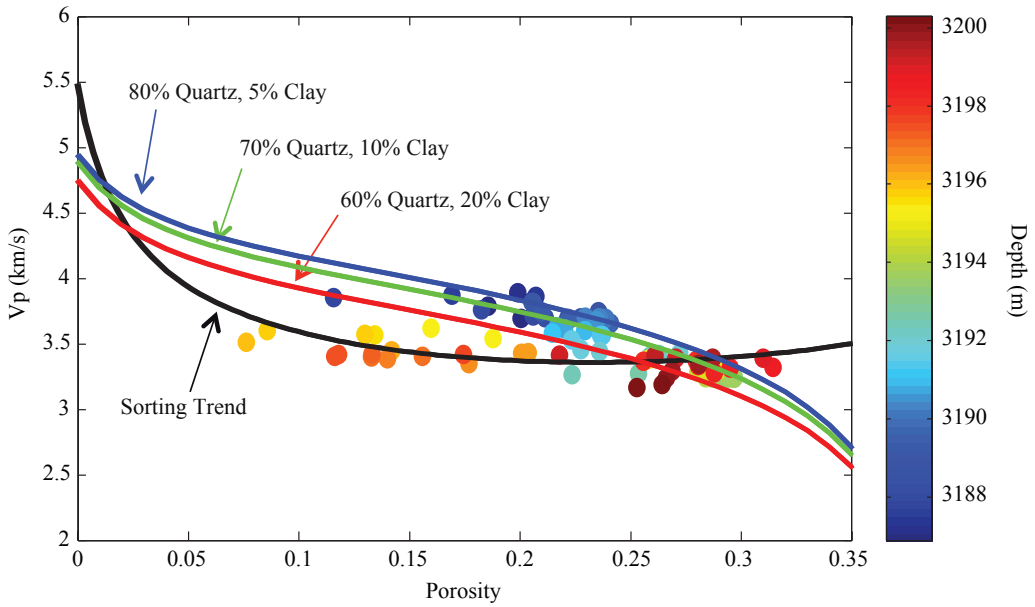

Figure 4.3: *Vp* versus total porosity (points) from the reservoir zone, colored by depth. Blue, green, and red lines are from the contact cement model for different rock frame compositions. Quartz and clay contents are shown, with the exact composition of each line shown in Table 4.1. P-wave propagation velocities in these lines decreases as quartz content decreases as clay content increases. The black line is a modified lower Hashin-Shtrikman bound and represents a sorting trend. In terms of sorting, the lower portion (3195–3202 m) is poorly sorted, and the upper portion is well sorted. The zero porosity end member of the sorting trend is based on a predominantly quartz mineral grain, and the high porosity end member is a fitting value for the trend determined at the critical porosity.

Table 4.1: Percentages of minerals used in the contact cement models.

Line	Quartz %	Clay %	Feldspar %	Muscovite %	Calcite %
Red	60	20	20	0	0
Green	70	10	10	7	3
Blue	80	5	5	5	5

Mineral compositions used in the model construction were based on studies of core samples from the F-2 well. Those samples indicated that the mineral composition of the reservoir consisted of 60–80% quartz, 10–20% clay, and 10–20% feldspar, with the remainder composed of small percentages of muscovite, calcite, and other minerals (Kordi et al., 2010). Variations on these compositions provided a range of effective rock moduli. For the deeper portion of the reservoir (3196–3202 m), a modified Hashin-Shtrikman lower bound was used (Figure 4.3, black line). This model provides an interpretation for the deeper reservoir interval as a mixture of both coarse and fine grains, which results in lower porosity relative to the shallower portion where the grains are well sorted.

4.4.2 Fluid Substitution

Figure 4.4 contains measured velocity logs and modeled logs calculated from fluid substitution with different pore fluids. In all panels of Figure 4.4, the blue curve represents a 100% brine-saturated rock. The green, red, cyan, and magenta lines show the modeled data for 25, 50, 75 and 100% CO_2, respectively. The thin black line is the measured log data. Velocity curves from the reservoir interval, with fluid moduli calculated from the Voigt bound, are shown in Figure 4.4a. The lines in Figure 4.4a show a uniform spacing between different fluid compositions, corresponding to the linearity of the Voigt average. The Voigt average is thought to be physically represented by the patchy saturation model. Figure 4.4b shows the velocity curves for the same reservoir interval using the Reuss bound for the fluid moduli for the different fluid compositions. These lines show a large decrease in velocity with a small amount of dissolved CO_2, but very little difference exists among the lines with higher CO_2

saturation. End member (0 or 100% CO_2) velocity curves were independent of how the fluids were mixed, as expected. Figure 4.4c is a plot of *Vs* for different CO_2 saturations. Shear velocity increases slightly with increasing CO_2 saturation due to the inverse relationship with bulk density.

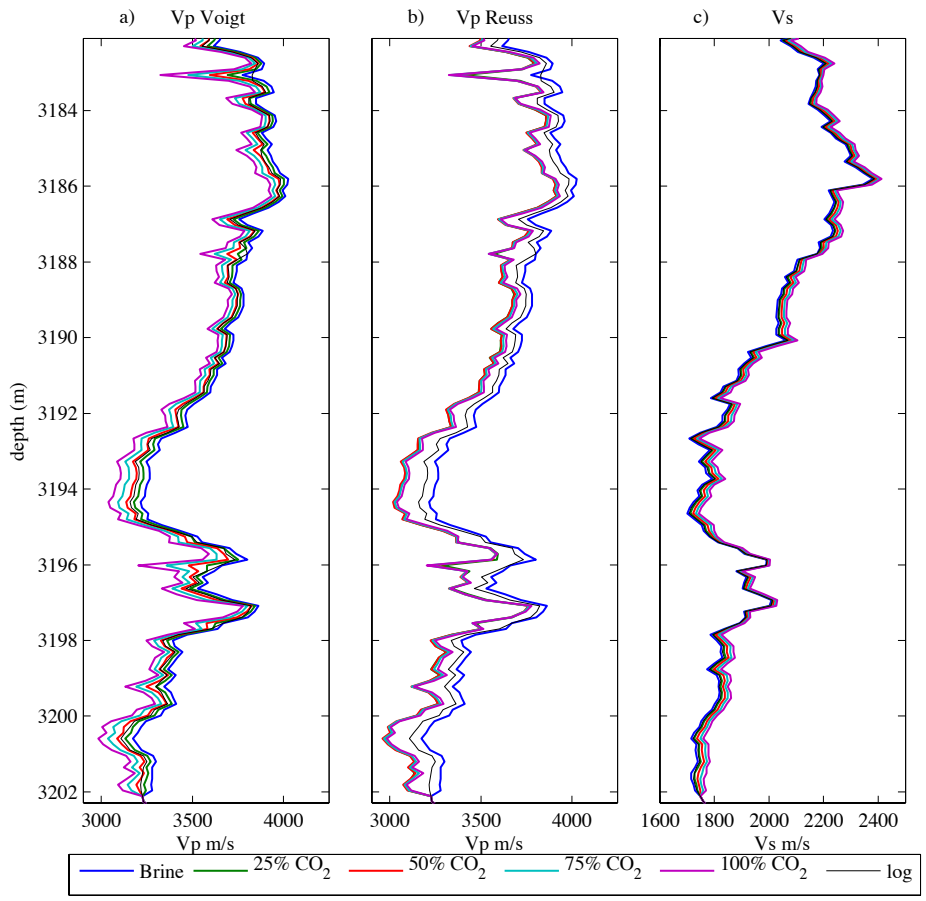

Figure 4.4: Panel a shows the fluid substituted P-wave velocity curves with fluid moduli calculated from the Voigt average (patchy saturation). Panel b shows the same, but the fluid moduli were calculated with the Reuss average. Panel c shows *Vs* data. In these graphs the blue, green, red, cyan, and magenta lines represent pure brine, 25%, 50%, 75% and 100% CO_2, respectively. The thin black line on all graphs is the measured log data included as a reference. The uniform spacing between different fluid compositions is because the Voigt average is linear (panel a). In panel b there is a large gap between the brine saturated curve and the curves containing partial or full CO_2 saturation because the Reuss average moduli changes significantly at low CO_2 concentrations and remains nearly constant with increasing CO_2. In panel c, *Vs* increases with increasing gas saturation solely because of density.

4.4.3 AVA

Angle-dependent reflectivity was calculated using the full Zoeppritz equations, as shown in Chapter 3, for incidence angles of zero to thirty degrees. Four thousand simulations were computed for each fluid composition (0, 25, 50, 75, and 100% CO_2). These correspond to Figure 4.5a–e, respectively. Additionally, the same number of simulations was run based on the measured log data (Figure 4.5f). All the AVA plots in Figure 4.5 are conditional PDFs of reflection coefficients given the angle of incidence and fluid saturation. The elastic properties used to populate these AVA models came from the modeled and measured logs in Figure 4.4a. Warm colors represent a high probability of generating a reflection coefficient given an angle, whereas cool colors indicate a low probability. The black line represents the mean curve for each fluid scenario.

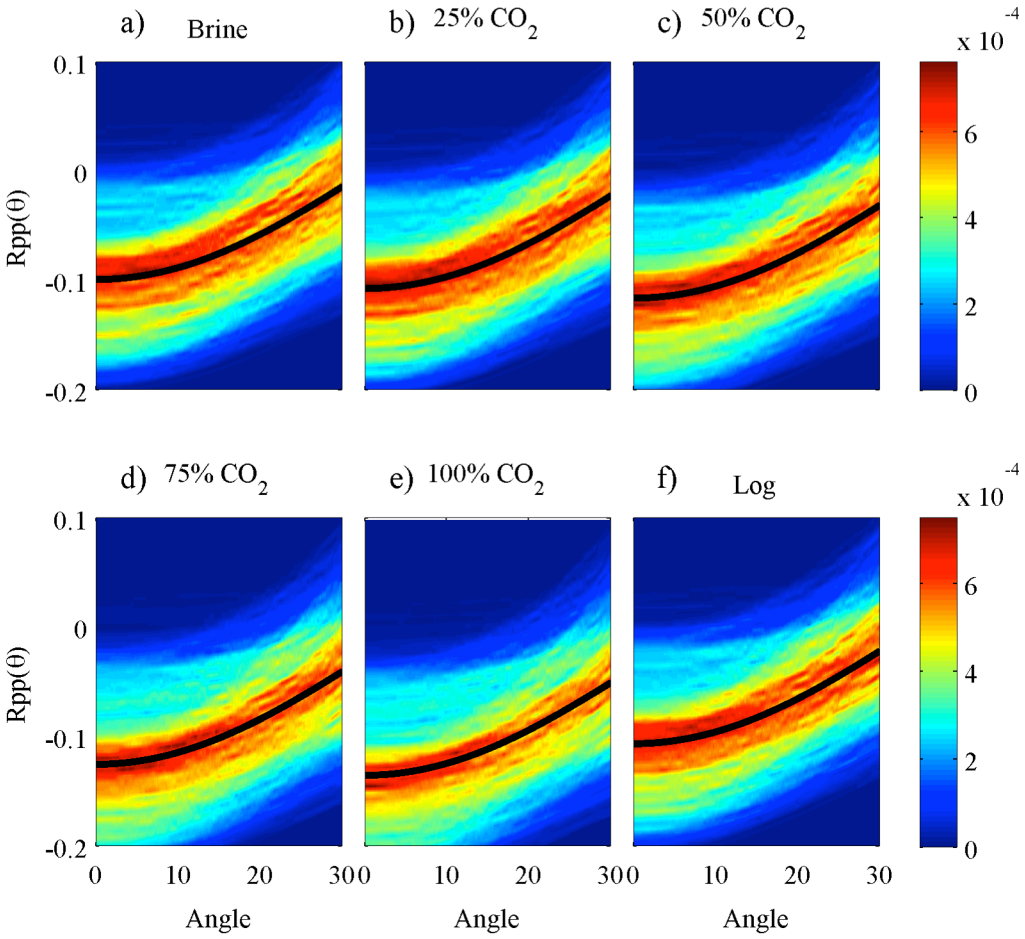

Figure 4.5: Each panel shows a PDF from a Monte Carlo simulation with 4000 realizations of angle-dependent reflectivity for a sandstone-shale interface. Reflection coefficients are on the y-axis and angle of incidence on the x-axis. Warm colors indicate high probability density and cool colors show low probability density. Plots a–e were computed with the lines from Figure 4.4a. Plot f is generated from the measured log data. Only minor differences exist among the AVA probability plots for pure brine and pure CO_2 (a and e) or the intermediate compositions.

The increase of the reflection coefficient value with increasing angle is consistent with a shale over a sequence of saturated sands. In each case, high probability regions correspond to negative values at 0° and less negative to zero values at 30°. All panels of Figure 4.5 show a significant degree of similarity, due to the stiffness of the cemented

sandstone reservoir, which works to minimize the fluid effect on the seismic response in the simulation. PDFs corresponding to AVA simulations generated from the modeled well logs in Figure 4.4b (not shown) were statistically equivalent to the PDFs corresponding to Figure 4.4a.

4.4.4 Classification

The three elastic property combinations that resulted in the highest success rates for mapping the fluid classes were *Vp/Vs-Ip* (Figure 4.6), *Vp/Vs-Vs* (Figure 4.7) and *Vp/Vs-Vp* (Figure 4.8). Bivariate PDFs were generated from these crossplots for each class. I examined the 100% CO_2 and 100% brine classes first because they corresponded to the largest differences in velocity and density. The expectation was that the highest classification success rate would occur for these two end-member classes. Data points from each class were mapped to their respective PDFs to determine their success rates. Figure 4.6a shows 100% CO_2 (blue) and 100% brine (green) data plotted by *Vp/Vs* as a function of *Ip*. Panels b and c show the PDFs generated from the CO_2 and brine data, respectively. Dark colors are areas of high probability, light colors are areas of low probability, and white are areas of zero probability. The numbers in panels b and c show the success rates for mapping to the fluid class of that panel, which were 0.72 when mapping 100% CO_2 data and 0.62 when mapping 100% brine data.

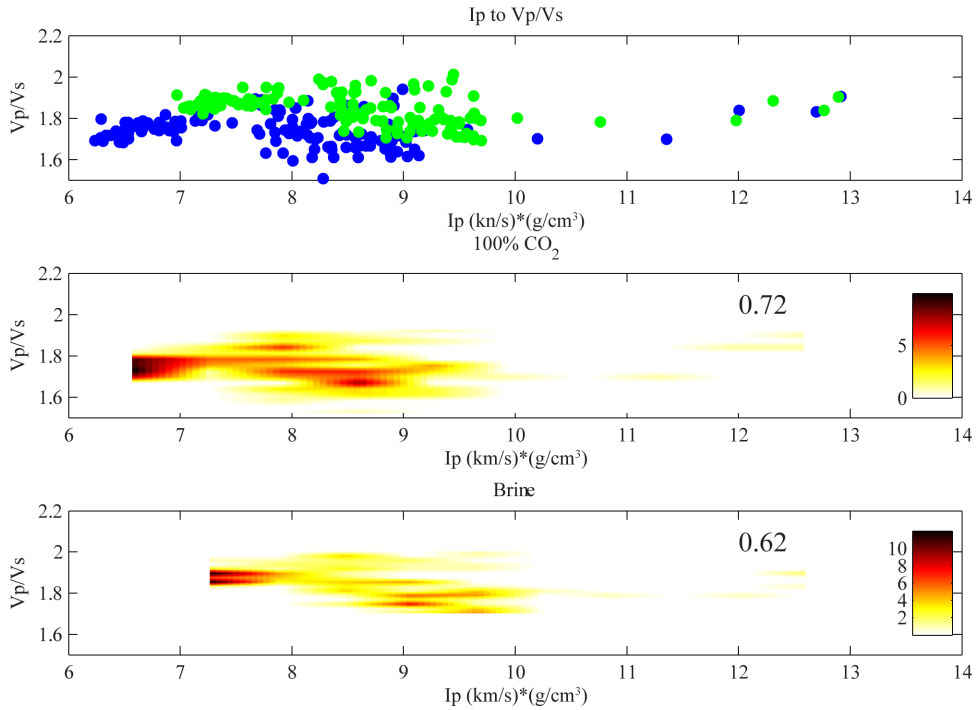

Figure 4.6: Panel a shows *Vp/Vs* as a function of *Ip* for 100% CO_2 (blue) and 100% brine (green). Panels b and c show the bivariate PDFs computed for the data in panel a, for the 100% CO_2 and the 100% brine data, respectively. For panels b and c black and red indicate areas of high probability density, whereas light yellow and white indicate areas of low probability or zero probability density. The number 0.72 on panel b is the success rate for mapping 100% CO_2 data to its PDF. In panel c 0.62 is the success rate for mapping 100% brine data to its corresponding PDF.

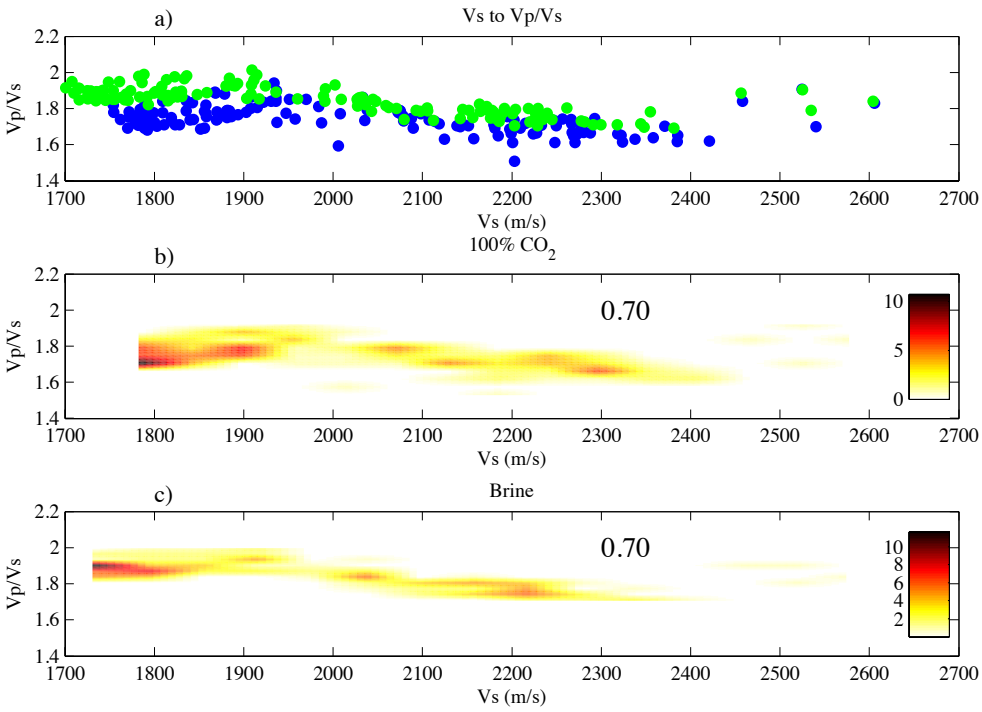

Figure 4.7: Panel a shows modeled data for 100% CO_2 (blue) and 100% brine (green) for *Vp/Vs* as a function of *Vs*. Panel b shows the bivariate PDF generated from the 100% CO_2 data points, and panel c contains the bivariate PDF generated from the 100% brine data. Color in panels b and c range from black and red (high probability density) to light yellow and white (low or zero probability density). The numbers in black on panels b and c indicate the success rate of mapping data back to its PDF.

In Figure 4.7a, *Vp/Vs* as a function of *Vs* was used to crossplot 100% CO_2 and 100% brine data, blue and green, respectively. The data in panel a was used to calculate the PDFs shown in panels b and c that correspond to 100% CO_2 and 100% brine data, respectively. Colors in Figures 4.7a and 4.7b signify the range of probability from low (light) to high (dark). When mapping with this combination of parameters, the success rate for both CO_2 and brine data was 0.70. The axes in Figure 4.8 show *Vp/Vs* as a function of *Vs*. Data plotted in Figure 4.8a corresponds to 100% CO_2 (blue) and 100%

brine (green). The 100% CO_2 data was used to generate the PDF shown in Figure 4.8b, and the 100% brine data was used to generate the PDF shown in Figure 4.8c. When mapping with these parameters, the success rates were 0.68 when mapping 100% CO_2 data and 0.73 when mapping 100% brine data. Figures 4.8a and b are colored to the same scheme as their counterparts in Figures 4.6 and 4.7.

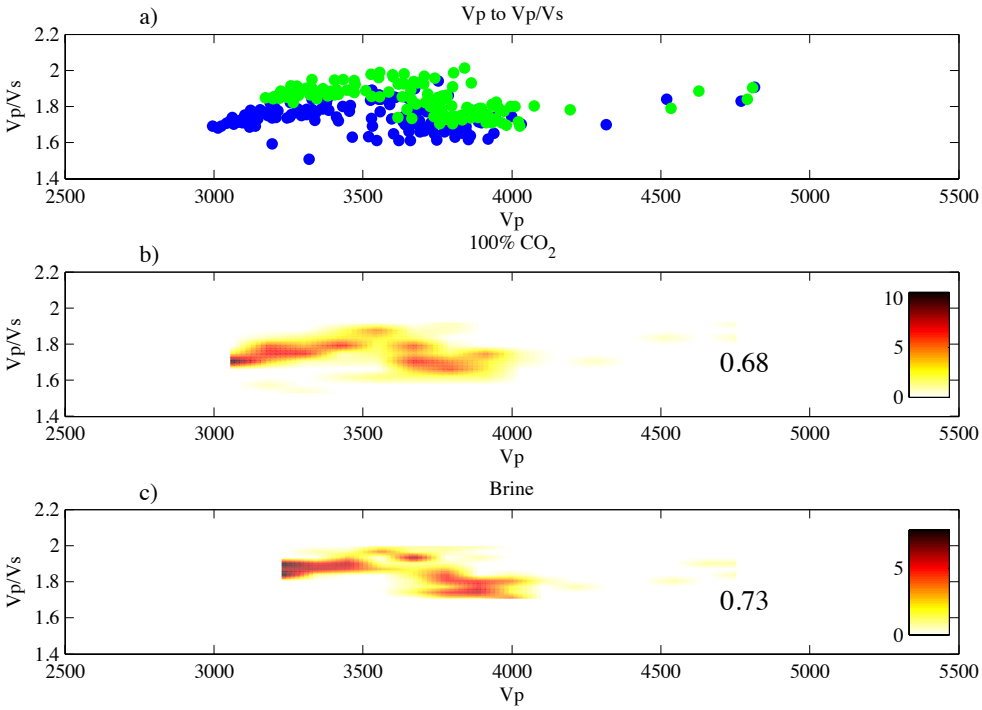

Figure 4.8: *Vp/Vs* as a function of *Vp*. Panel a shows blue and green data representing 100% CO_2 and 100% brine, respectively. Panels b and c show the bivariate PDFs generated from the 100% CO_2 and 100% brine data from panel a. Black and red colors indicate high probability density. Light yellow and white indicate low probability density. Success rates for mapping 100% CO_2 and 100% brine are shown in panels b and c, respectively.

Results from classifying the intermediate fluid compositions generated lower success rates than did classifying the end members, as expected. Table 4.2 shows the

results of mapping intermediate fluid compositions against brine and against measured log data. In Table 4.2 the six columns of data represent the results of plotting 25, 50 and 75 % CO_2 concentrations against measured data (columns 2 through 4) and against 100% brine (columns 5 through 7). Fluid moduli in Table 4.2 were calculated using the Reuss average.

Table 4.2: Classification success rates for the intermediate fluid concentrations mapped to their respective PDFs for the three best performing crossplots from the study. Fluid properties were calculated from the Reuss average. The column headings indicate the two fluid classes being compared. For example, 25/log indicates that 25% CO_2 was being compared to log data, 25/0 indicates that 25% CO_2 data was being compared to 100% brine date. Values in the body of the table indicate the success rate of mapping the data correctly between the mixed fluid (first value) and either the log and or brine data (second value).

Crossplot	25/log	50/log	75/log	25/0	50/0	75/0
Vp/Vs to Ip	.478/.732	.617/.683	.664/.577	.593/.688	.693/.602	.735/.495
Vp/Vs to Vs	.550/.835	.628/.727	.627/.672	.519/.857	.675/.761	.698/.597
Vp/Vs to Vp	.576/.815	.641/.704	.638/.652	.671/.713	.705/.692	.733/.645

Table 4.3 shows the same data as Table 4.2 except that the fluid parameters were calculated using the Voigt average. The results show, in general, an increase in the success rate with an increase in percent CO_2 for both methods of calculating fluid moduli. When using the Reuss average, slight increases occurred in success rates with increases in CO_2 percentage. However, success rates of data derived from the Voigt bounds displayed a larger increase in success rate with increasing CO_2 percentage compared to the respective class calculated with the Reuss bound. The highest success rate for either fluid modeling method corresponded to *Vp* against the *Vp/Vs* ratio, with *Vs* against *Vp/Vs* showing a similar but slightly reduced success rate compared to *Vp-Vp/Vs*.

Table 4.3: The intermediate fluid concentrations mapped to their respective PDFs for the three best performing crossplots from the study. Fluid properties were calculated from the Voigt average. Column headings are the fluid classes being compared with the first value indicating the CO_2 percentage and the second value being either log data or 100% brine data. Values indicate the success rate of mapping the data correctly between the mixed fluid (first value) and either the log and or brine data (second value).

Crossplot	25/log	50/log	75/log	25/0	50/0	75/0
Vp/Vs to Ip	.322/.577	.440/.642	.522/.672	.505/.447	.621/.514	.636/.611
Vs to Vp/Vs	.459/.537	.458/.606	.492/.811	.385/.692	.631/.878	.549/.833
Vp to Vp/Vs	.385/.611	.445/.630	.496/.748	.491/.487	.626/.624	.646/.684

4.5 DISCUSSION

Rock-physics modeling for this study was useful in that it provided a way to correlate the mineral compositions provided by the petrography studies to mineral moduli that were needed for fluid substitution modeling and AVA analysis. Additionally, the calibrated rock-physics model showed that increasing quartz and decreasing clay content in the matrix can cause *Vp* and *Vs* to increase. Increases in cement concentration can have a similar effect. The calibrated models that link lithology, porosity, and cementation to seismic velocity will be useful for providing constraints on those same parameters away from well control.

Fluid composition and the mixing of fluid moduli played an important role in the velocity modeling. When the fluids were mixed using a patchy saturation model, a linear trend resulted in *Vp* with changes in CO_2 saturation. When the fluids were mixed uniformly, as is represented by the Reuss bound, little variation in velocity existed among concentrations of CO_2 of 25 to 100 % (Figure 4.4b). However, a substantial change in velocity occurred between 0 and 25 % CO_2 (Figure 4.4b). This agrees with previous work that indicated that velocities depend on fluid saturations and on the way those fluids are

distributed within the pore space (Mavko and Mukerji, 1998). This phenomenon is similar to the commonly recognized fizz-water problem characterized by a minimal difference in seismic responses between high and low gas content in brine. The consistency between the modeled *Vs* values is easily understood because only density affects *Vs* (Figure 4.4c, Equation 4.4) as a function of fluid composition. Bulk density changes linearly with changes in CO_2 percent because it is calculated from a weighted average of fluid components and rock frame minerals.

A lack of variation in the AVA modeling due to fluid composition is evident in the results. All panels of Figure 4.5 show very similar reflection coefficients at all angles. This lack of variation in the AVA responses can be explained by the stiffness of the rock frame due to the cement content. The stiff frame restricts the sensitivity of the rock elastic properties to fluid changes (Castagna and Backus, 1993). Given the stiffness and relatively high velocities associated with the reservoir rock, I should expect small variations in the AVA response with a change in fluid composition. Additionally, the larger the contrast in the rock properties across an interface, the smaller the effect the fluid will have on the reflection coefficient (Stine, 2004). By shifting the interface in this study I hoped to minimize this effect and mimic the upscaled interface as would be seen with surface seismic or VSP data. However, due to the internal stiffness of the reservoir we were still not able to attribute an AVA response to changes in fluid saturation.

Results from the classification scheme were encouraging because they show a relatively high success rate when using *Vp/Vs* versus *Ip*, *Vp*, or *Vs* within the reservoir interval. These occurrences indicate that *Vp/Vs* is important and useful for characterizing and monitoring injected CO_2. This is because *Vp/Vs* effectively illustrates only the fluid

component of the rock as the terms relating to the rock frame cancel. Additionally, we show that in general, as the difference between the fluid compositions increase, the classification success rate also increases. The ability of *Vp/Vs* to discriminate between different fluids has been shown before in trying to differentiate between brine and hydrocarbons (e.g., Castagna and Backus, 1993).

When examining the scatter plots of the data and the bivariate PDFs (Figure 4.6–4.8), sharp edges are present along the boundaries of the PDFs separating areas of high probability and zero probability. An example of this is Figure 4.7b (*Vp/Vs*=1.8 and *Vs*=1780 m/s). This is an artifact of the binning used when computing the PDFs. It has the potential to have a small negative impact on successfully mapping data points back to their respective classes. Figure 4.9a shows the PDF for 100% CO_2 pore fluid, and Figure 4.9b shows the PDF for 100% brine pore fluid. Black points in both panels are the data from which the distributions were computed. Because of the binning procedure, some data points fall outside the boundaries of their respective PDFs. During the mapping routine, these data points were not assigned to either distribution. One way to minimize this effect in future studies would be to simulate statistically equivalent data points to increase the total number of data points used to compute the PDF. This could help to extend the range of the PDF and smooth the edges to avoid large numbers of data points falling into zero probability regions, thereby likely improving classification success rates.

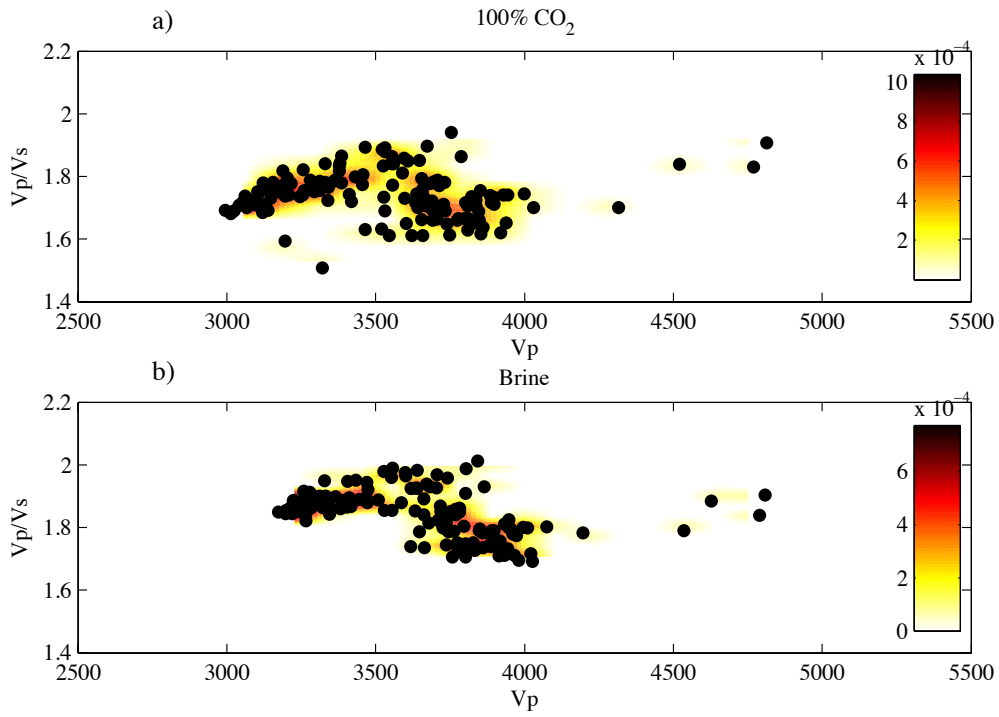

Figure 4.9: Modeled data plotted atop its corresponding bivariate PDF. Panel a shows 100% CO_2 data and panel b shows 100% brine data. Red and black colors in these panels represent high probability density, whereas light yellow and white represent low and zero probability density. These plots illustrate that some high-density clusters of data points extend beyond the edges of the PDFs into areas of zero probability. In the classification scheme, these points were not mapped to any PDF, which lowered the success rate.

4.6 CONCLUSIONS

This study shows that AVA might not be reliable when examining fluid substitution in the Cranfield reservoir because the rock frame is stiff. When looking at a shale-sandstone interface with a large impedance contrast, the reflection coefficient will not show significant changes with respect to changes in fluid composition. Because the changes in fluid composition do not significantly alter either the shear impedance or the density of the rock, the angle-dependent reflection coefficients will not show much variability with changes in fluid. The combination of these two factors works to minimize the change in AVA due to a change in fluid composition.

Fluid mixing laws can significantly impact the elastic properties of the fluid. When mixing two fluids that have very different elastic moduli, such as brine and supercritical CO_2, using the Reuss bound rather than the Voigt bound, the change in effective moduli is more apparent at small percentages of supercritical fluid saturation than higher concentrations. Because shear moduli are fluid independent and density is computed as an arithmetic average, calculated *Vs* for a fluid-saturated rock is independent of the method used to calculate the fluid parameters. Accordingly, crossplots of *Vp* as a function of *Vp/Vs* and *Vs* as a function of *Vp/Vs* provide the best ability to discriminate between variations in fluid composition in a stiff rock frame. Although *Vp/Vs* cannot be used as a direct indicator of fluid composition, crossplots generated with it are useful for comparing modeled fluid substitution data to measured data. From these crossplots, PDFs can be generated to assess the change and the associated uncertainty for time-lapse studies.

This study shows the sensitivity of the elastic properties of the Cranfield reservoir to changes in CO_2 saturation through different quantitative seismic methods. We did this using relatively high resolution well log data. Although surface seismic data and 3D VSP data both are lower resolution than well log data, they provide areal coverage away from well control. Among the methods we examined, the classification scheme provided the most encouraging results. When we apply this to the surface data, we likely will use the same combinations of elastic properties used in the well log data procedure. Those elastic properties are the parameters most commonly extracted from seismic data. Classification of seismically derived elastic properties, calibrated to well data, should

allow for characterization of fluid volume and location and assessment of the associated uncertainty.

Chapter 5: Inversion of Multicomponent 3D VSP Data for Porosity and CO_2 Saturation at the Cranfield Injection Site, Cranfield, MS[1]

5.1 ABSTRACT

Studying how injected CO_2 affects the seismic response of reservoir rocks is important because it can improve subsurface characterization where CO_2 injection is taking place. This study uses multicomponent data from a 3D vertical seismic profile (VSP) and well logs to model and invert probabilistically for the porosity and CO_2 saturation at the Cranfield reservoir. Initially the well logs were used to calibrate a rock-physics model. Once the accuracy of the model was verified, *Ip* and *Vp/Vs* from inverted multicomponent VSP data were used to estimate the porosity and fluid saturation. This inversion generated probabilistic estimates of porosity and CO_2 saturation for the area of the reservoir sampled by both PP waves and PS waves. Inversion results using the measured well log data for calibration showed that the model was able to estimate porosity with a relatively high degree of accuracy, with root mean square (RMS) error being less than 3% for all calibration tests. Fluid saturation was estimated, however, with reduced accuracy, with RMS errors ranging from 6% to 22% depending on the composition of the calibration test fluid. Results from integrating the multicomponent VSP data with the rock-physics model showed that estimated reservoir porosities are quite close to measured values at an observation well. CO_2 saturation estimates indicated that this method can differentiate between areas containing CO_2 and those that do not.

[1] The contents of this chapter were originally published as: Carter, R.W., K. Spikes, and T. Hess, 2014, Inversion of multicomponent 3D VSP data for porosity and CO_2 saturation at the Cranfield injection site, Cranfield, MS: Interpretation, **2**, SE77-SE89. Dr. Spikes provided technical guidance and supervision on this project. The contribution of Mr. Hess included processing of the multicomponent data and helping with shot point selection.

5.2 INTRODUCTION

Multicomponent surface seismic and vertical seismic profile (VSP) data are useful for improving imaging resolution and characterizing fluid composition of subsurface reservoirs. Multicomponent data have proven beneficial in characterizing the subsurface by providing shear-wave information in addition to compressional-wave data (e.g., Miao and Zuk, 2007; Fomel and Backus, 2003; and Sears et al., 2010). Dang et al. (2010) used P-wave (PP) and P-to-S (PS) mode-converted reflection data to differentiate between false hydrocarbon indicators and an oil-bearing sand reservoir. They found that joint inversion of PP and PS data provided enough additional information to characterize false 'bright spots' versus hydrocarbon sands, which were not differentiable in PP data. Miao and Zuk (2007) researched data processing techniques to better constrain anisotropy parameter estimates to improve velocities for prestack time migration of PP and PS data. Fomel and Backus (2003) examined different approaches to register PP data with PS data. They found that a least-squares based registration algorithm could improve resolution relative to other registration methods. The utility of multicomponent data has been realized in monitoring offshore fields with ocean-bottom seismic recorders (Sears et al., 2010). This work showed that using elastic full-waveform inversion of both P and S data could be useful in reservoir characterization by increasing resolution of the final datasets. Shorter wavelengths associated with the slower S-waves improved resolution of the subsurface relative to what could be obtained using strictly P-wave data. Hardage et al. (2009) used multicomponent ocean-bottom cable data to look at near-sea-floor geology. Although the survey used by Hardage et al. (2009) had been designed to study

much deeper targets, the use of multicomponent data enabled near-surface features to be resolved, both vertically and horizontally, with resolution an order of magnitude better than conventional PP data.

VSP data, either P-wave or multicomponent, have advantages over surface seismic data. VSP data have the potential to resolve thinner layers because of broader bandwidth compared to standard surface data (Müller et al., 2010a). Because of the increased resolution, research into the application and processing of VSP data, both 3D and walkaway, has increased in recent years. Burch et al. (2010) successfully used a 3D VSP to help image reservoirs located near base of salt. In a different study, Müller et al. (2010b) examined the entire process through design, acquisition, processing, use and value of 3D multicomponent VSP data. Their study found that increasing the number of shots and the length and number of receivers on the receiver string increased the area that could be imaged with a 3D VSP with a minimal impact on resolution and frequency of the processed VSP dataset. They also found that high quality images could be generated with a reduced number of optimally located sources, potentially making acquisition more affordable. Walkaround VSP data have been found to be useful for measuring azimuthal anisotropy around a well (Dulaijan et al., 2012). Dulaijan et al. (2012) used multicomponent walkaround VSP data to characterize fracture orientation around a well bore by correlating the azimuthal anisotropy to fractures. Similarly Grechka et al. (2000) found that the use of multicomponent VSP data could help to characterize anisotropy. In particular, they showed that multiazimuth walkaway VSP data, when inverted for anisotropic parameters, contains enough information to constrain all but one of the elastic parameters of a monoclinic medium. These advancements indicate that VSP data

processing and interpretation techniques can provide important information for subsurface reservoir characterization. Accordingly, I applied an inversion technique of multicomponent VSP data to estimate porosity and pore-fluid quantities at a CO_2 injection site.

Geologic storage and sequestration of CO_2 both have the potential to increase oil production from mature fields in addition to reducing the amount of anthropogenic CO_2 released into the atmosphere. Recent studies have shown that injected CO_2 can be accommodated in brine and depleted hydrocarbon reservoirs. This potential has been shown at various sites around the world including Snøhvit (Grude et al., 2012), Weyburn (Ma and Morozov, 2010 and Verdon et al., 2010), and Krechba (Mathieson et al., 2010). VSP and other surface seismic methods can potentially provide some of this monitoring capability over large-scale areas where dense well bore coverage would be uneconomical or impractical. Regardless of the field location or scale, an important aspect is to monitor the volume and location of injected CO_2 to ensure secure storage. VSP data have the potential to provide high quality PP and PS data that can be used for accurate monitoring of in-situ CO_2. Additionally, VSP information might be useful for CO_2 monitoring because of the availability of boreholes in many mature and developed hydrocarbon fields. However, the improved resolution compared to surface seismic data comes at the expense of the lateral coverage typically associated with surface seismic data. By comparing the differences between multiple vintages of VSP and/or surface seismic data over the same field, time-dependent variations can be observed. These differences can relate to changes in pressure, fluid type or volume, and/or geomechanical effects.

Multicomponent surface seismic or VSP data can be used in a joint inversion. Joint inversion techniques have been used successfully with rock-physics models to help characterize hydrocarbons, porosity, and lithology (Bachrach, 2006; Spikes et al., 2007; Avseth and Norunn, 2011, and Jiang and Spikes, 2013). The study by Bachrach (2006) used rock physics, stochastic modeling, and a Bayesian estimation method to generate porosity and fluid-saturation maps of expected pay sands. Data came from both surface seismic data and well logs. Results indicated a direct correlation between the uncertainty associated with estimations of porosity and the uncertainty of the associated water saturation. Joint inversion of well log data using a rock-physics model for distributions of reservoir properties was also demonstrated by Jiang and Spikes (2013) in their work on the Haynesville shale. These studies primarily focused on using the elastic parameters computed from well logs in conjunction with a rock-physics model to model lithological parameters for the fluid content of reservoir rocks. Moyano et al. (2011) examined the calibration of rock-physics models and found that the accuracy of the modeling could be improved with a more rigorous approach to both model calibration and quantitative analysis. The study presented here adapts fluid-characterization techniques used for hydrocarbon reservoirs to a reservoir undergoing CO_2 injection for storage and utilization purposes.

5.3 METHODOLOGY

This study consisted of five steps. First I selected the shot points for PP and PS data by modeling reflection angles where both data types sampled the same portion of the reservoir. I then processed the selected shot gathers and mapped them from VSP to CDP geometry. The third step was to calibrate a rock-physics model to the well data and to

test that calibration. Fourth, the VSP data mapped to CDP geometry was jointly inverted for P- and S-impedance. Last, the P- and S-impedance information was then inverted using the rock-physics model to generate probabilistic estimates of porosity and CO_2 saturation in the reservoir.

For this study the 3D VSP and well log data were used. The VSP was shot into well F-1 (see Figure 5.1). Shot points from the VSP are shown by small back dots, and the PP and PS shot points used in this work are shown by the large black squares. Because of the geometry of the VSP and the difference in reflection angles between PP and PS data, only a single pair of shot points sampled the same portion of the reservoir with both PP and PS data (see Figure 5.2). An arc of constant distance from the receiver string is shown, which crosses other potential shots from which PS data could be used to sample the reservoir (see Figure 5.1).

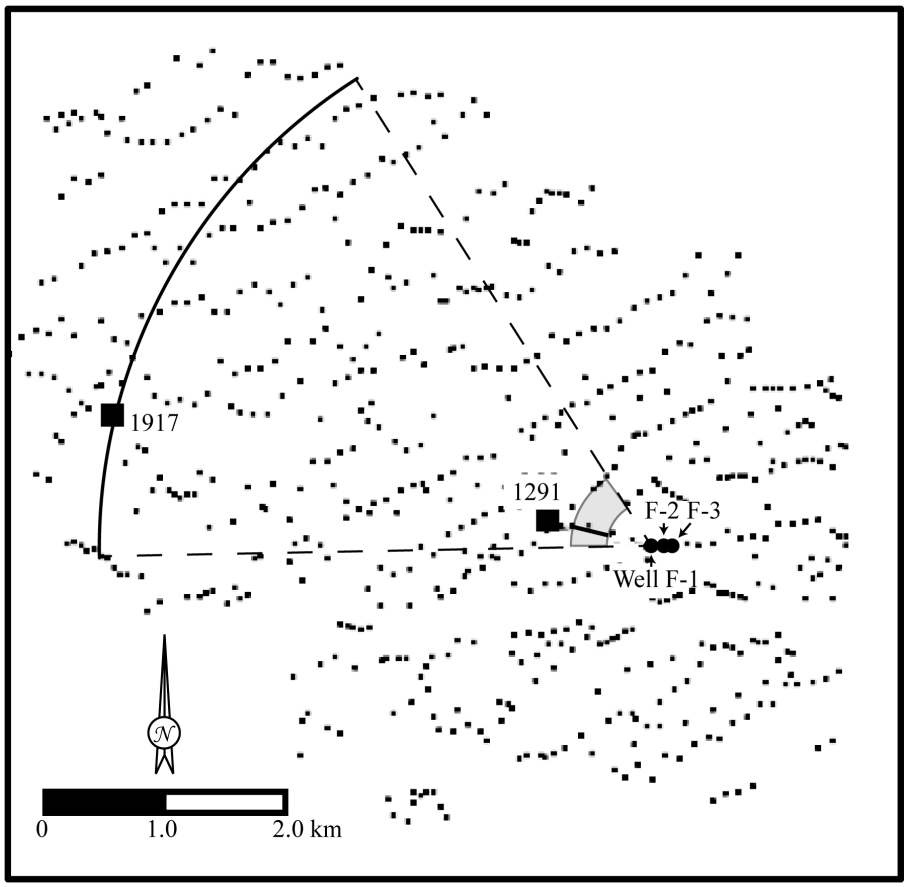

Figure 5.1: A shot point map of the 3D multicomponent VSP survey. The large black circles indicates the location of the VSP receiver string (F-1) and the monitoring wells used in this study (F-2 and F-3). The shot points from which PP and PS data were selected are shown by the black squares 1291 and 1917, respectively. An arc through shot point 1917 shows the offsets from which PS data potentially could be used to sample the reservoir interval. The gray shaded partial toroid near well F-1 shows the area of the reservoir that potentially could be sampled by CDP reflection points if all available PS and PP shots were used. The black line within the shaded region shows the location of the 2D section used in this study.

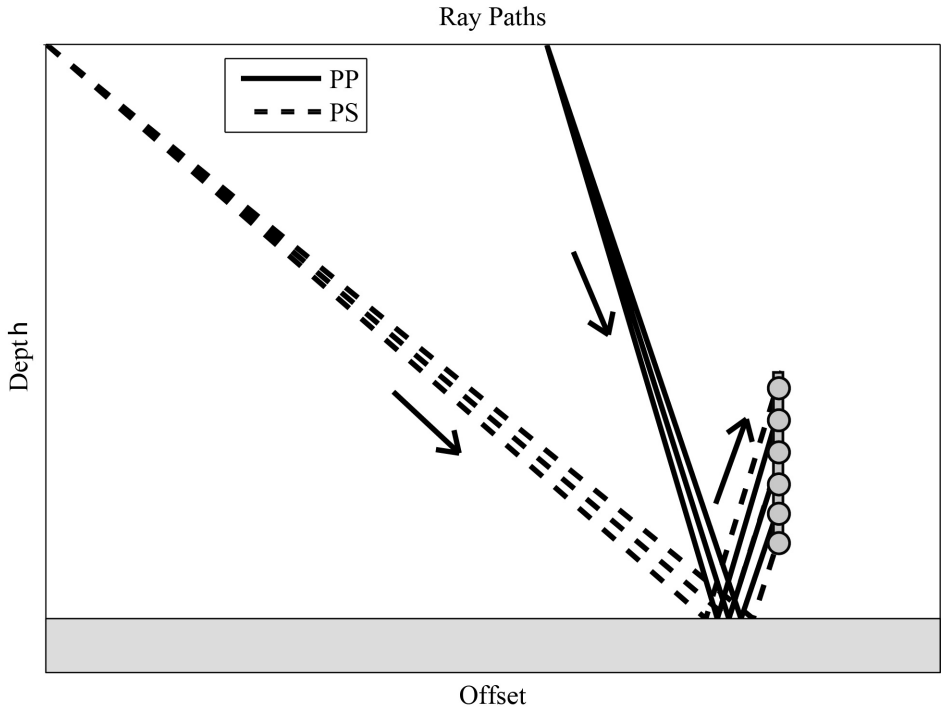

Figure 5.2: Ray tracing schematic to illustrate PP and PS raypaths that are incident at the same subsurface location. Depth is on the vertical axis, and offset from the receiver string is shown on the horizontal axis. The gray bar with gray circles represents the receiver string. Idealized PS data from the distal shot are shown by dashed lines, and the idealized ray paths from the PP shot are shown by solid lines.

5.3.1 Shot point selection

Because of the geometry of the survey and the difference between PP and PS reflection angles, one pair of PP and PS shots sampled the reservoir location near the injection or monitoring wells. Ray tracing with a simple model (constant Vp/Vs=2.0) provided the estimated offset ranges for the pair of PP and PS shot points. An example of this ray tracing is shown in Figure 5.2, where offset from the receiver string (the gray bar with receivers represented by gray circles on the right of the figure) is the x-axis, and depth is the y-axis. The solid lines illustrate idealized PP rays from a single shot, and the dashed raypaths illustrate the idealized PS raypaths from a single shot. Both sets of raypaths sample the same portion of the reservoir and have near parallel up-going rays

incident on the receiver string. From this information a pair of shot points with the appropriate offsets were selected that were within a few degrees of being in line with each other and with the receiver string. This pair of shots sampled the reservoir between the PP shot point and well F-1 (shown by the black line within the gray shaded area of Figure 5.1). Only a single pair of shot points were analyzed, and the receiver string was located at a depth from 2407 to 3143 meters for both shots. However, if additional pairs of shot points were selected, the area of the reservoir being sampled by both PP and PS data could be expanded radially around the receiver string to resemble a partial toroid as shown by the shaded gray area of Figure 5.1.

Logs from well F-2 before injection commenced are shown in Figure 5.3. For comparison, the selected shot gathers from the VSP (PP and PS) are also shown. Panels a, b, and c show the *Vp* and *Vs*, porosity, and gamma ray logs, respectively, whereas panels d and e show the PP and PS information, respectively. The reservoir interval in well F-2 can be divided into two distinct zones. Well F-2 was used because it is the closest well to F-1, closest to the area of the reservoir sampled by the selected shot points, and it contains dipole sonic measurements. The upper reservoir zone shown in dark gray ranges from 3184 to 3194 meters, and the lower reservoir zone, shown in light gray extends from 3196 to 3202 meters. The gamma ray log (panel c) shows an increase in gamma ray count at 3195 meters and indicates a local shale layer that divides the upper and lower reservoir zones. In panels d and e the two shot gathers contain both up-going and down-going waves. The horizons of interest can be seen in panels d and e at the location of the dashed line. The data from shot point 1917 (panel e) has fewer traces than the data from shot point 1291 (panel d) because only a subset of the geophones on the

receiver string sampled energy reflected from the horizon of interest. In panels d and e, down-going (direct) ray paths are shown by events with negative slope. Up-going (reflected) ray paths appear as events with a positive slope.

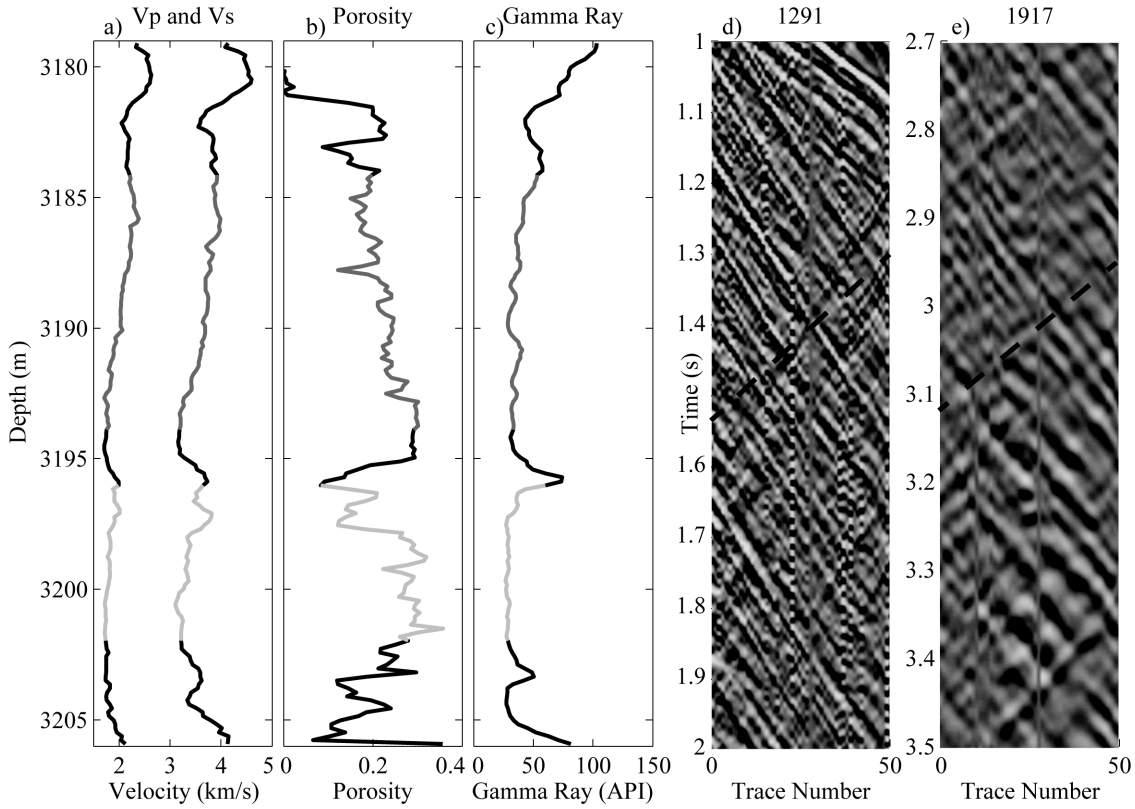

Figure 5.3: Data from Well F-2 and VSP data in well F-1. The dark gray line shows the shallower reservoir zone, which extends from about 3184–3194 m, and the light gray line shows the deeper reservoir zone, which extends from about 3196–3202 m (a, b, and c). The shale layer that divides the two reservoir zones is apparent from the increase in the gamma ray count between 3194–3196 m. Panels d and e show the PP and PS data, respectively, from the VSP. The reservoir zone is indicated by the dashed line in panels d and e.

5.3.2 VSP to CDP mapping

VSP shot gathers have a very different geometry compared to CDP gathers. The conversion from VSP to CDP geometry involved a mapping algorithm as part of the

processing sequence. This step enabled VSP traces to be processed using standard algorithms and workflows. The basic algorithm for the VSP to CDP conversion is outlined by Hardage (1985). First, the down-going wavefield was removed from the up-going wave field with the use of an *f-k* filter. In this case the filter needed to be selected very carefully for the PS data because of similarities between tube-wave energy and PS energy in *f-k* space. Second, the up-going wave field was converted to two-way time by applying a static time shift and normal move out correction. For this work, a fixed *Vp/Vs* of 1.68 was used to convert the up-going S-waves to two-way time. The third step of the process was to convert the VSP data in two-way time to a CDP geometry. This step was accomplished by assuming a constant velocity earth and straight ray paths to map from the source location to each receiver location. Lee (1984a,b) covers in complete detail the mathematical basis for steps two and three, to resample the reflections from time-depth to two-way time in the VSP to the CDP profile.

Processing of the VSP data included the following steps. Initially the three components were rotated into the appropriate directions. Before VSP to CDP mapping, shot-signature deconvolution removed the effects of phase and frequency characteristics of the recording geophone and cable. Next a band-limited gap deconvolution shaped the wavelets to zero phase and removed periodic multiples. The *f-k* filter was then applied to the PP and PS data to remove the down-going wave field. The data were then filtered again in *f-k* space to remove tube waves. With the down-going rays and the tube waves removed, the data were ready for the VSP to CDP transform. Although these basic steps were both used on the PP (vertical component) and PS (horizontal component) data, the

specifics of the *f-k* filters were quite different between the PP and PS data due to nonuniform tube-wave interference.

Figure 5.4 shows both the PP and the PS data from shot points 1291 and 1917, respectively, after the VSP to CDP mapping and after registration. When dealing with PP and PS data, registration is the correlating of horizons from PP data to the same geologic event shown in PS data. Panels a and b show the results from the VSP to CDP mapping of PP and PS data, respectively, in PP time. In panel c, the PS data is shown in PS time, which is approximately 1.68 times that of the two-way travel time because of the constant *Vp/Vs*. Little has changed other than a bulk time shift from panel b to panel c. In panel c the intervals where *Vp/Vs* is not exactly 1.68 show stretching and/or squeezing if the *Vp/Vs* of that interval was lower or higher, respectively, than 1.68. The black box in all three panels shows the location of the reservoir and the subset of the seismic data used in the inversion.

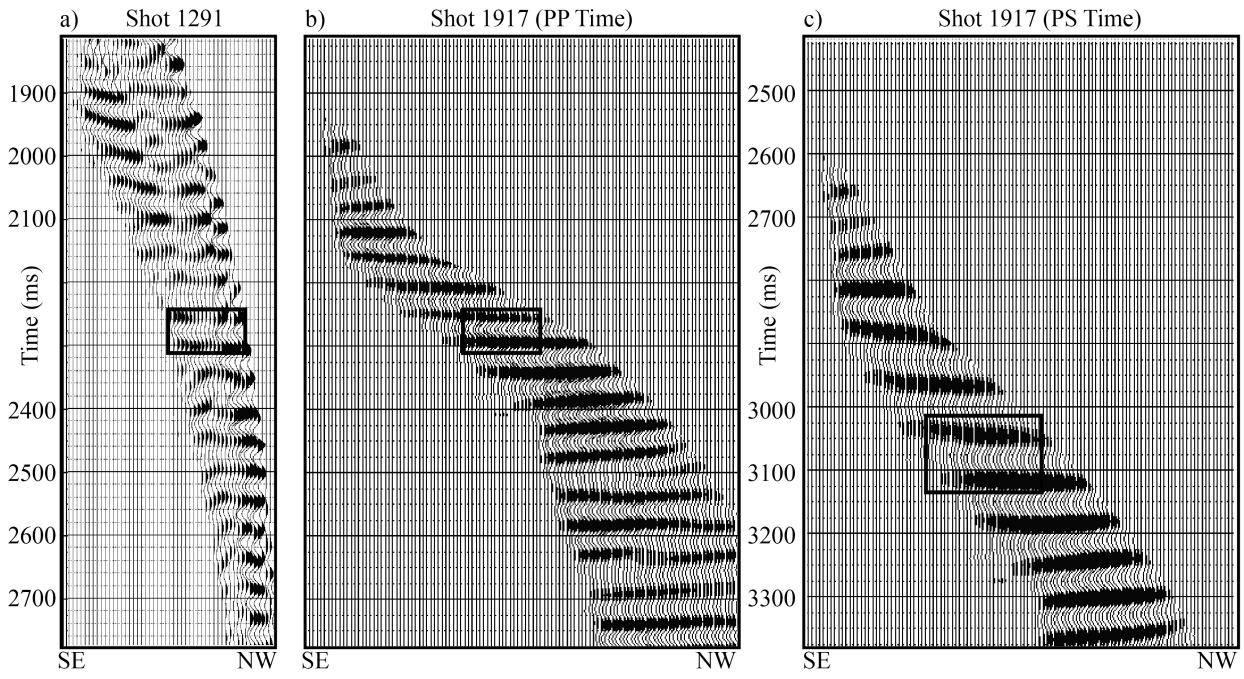

Figure 5.4: Panels a and b show PP and PS data, respectively, in PP time. Panel c shows the same data as panel b, only in PS time. The black box on each panel shows the zone of the reservoir and the data used in the inversion.

5.3.3 Impedance inversion

After registration of the data along the reservoir horizon, the PP and PS data were jointly inverted for *Ip* and *Is* using a commercial model-based algorithm. This inversion required a well within the dataset that contained both P- and S-wave sonic measurements. Even though well F-2 is 69 m away from the seismic line, it was artificially repositioned to fall within the dataset. A comparison of the wavelets and amplitude spectra of the data are shown in Figure 5.5. In Figure 5.5, panels a and c show the PP and PS wavelets, respectively, that were extracted from the seismic data. Panel b shows the amplitude spectrum of the PP data, and panel d shows the amplitude spectrum of the PS data. Even though the PS data do not indicate as high a frequency content as the PP data, the slower velocity means that resolution will not be adversely affected. Panels e and f show the

inverted impedance from the PP and PS (dashed line) data, respectively, along with the impedance from the nearest point of well control (solid line).

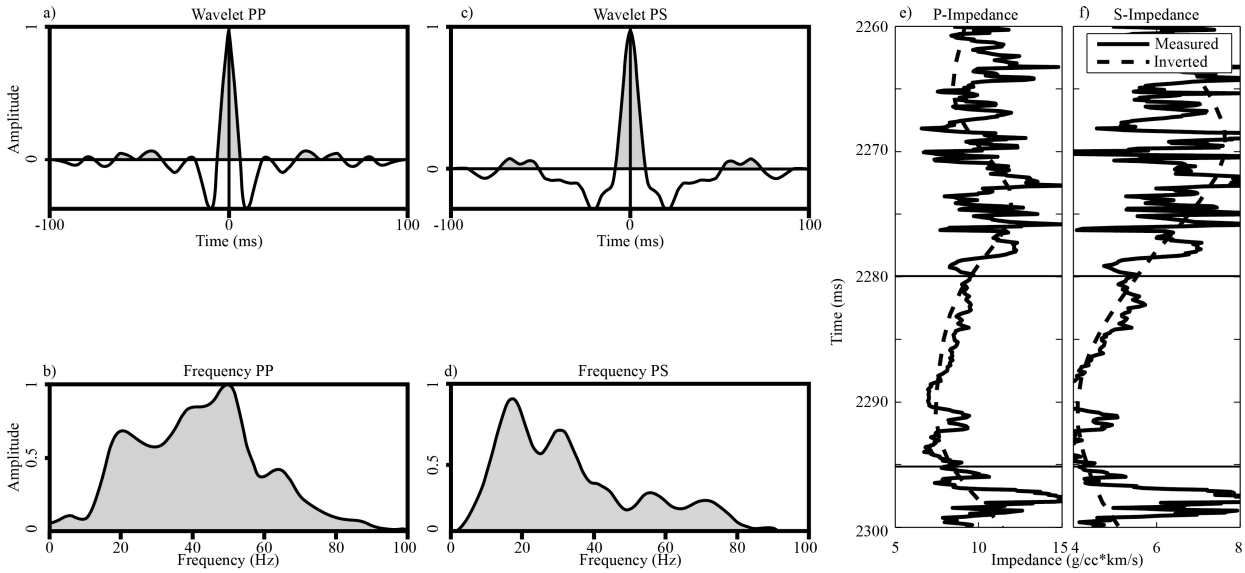

Figure 5.5: Panels a and b show the wavelet and amplitude spectrum, respectively, extracted from shot point 1291. Panels c and d show the wavelet and amplitude spectrum, respectively, extracted from the PS data from shot point 1917. Panel e shows the extracted impedance trace from the PP data with a dashed line and the measured P-impedance (solid line) from the F-2 well. Panel f shows the S-impedance taken from the inverted data from shot point 1917 in the dashed line and the S-impedance from well F-2 with a solid line. The reservoir is located between the horizontal lines on panels e and f.

5.3.4 Rock-physics modeling

Previous work conducted on data from the Cranfield site, in particular on the F-2 well, showed that the reservoir interval is composed primarily of 60–80% quartz, 10–20% clay, and 10–20% feldspar, with the remainder being small percentages of muscovite, calcite, and other minerals (Kordi et al., 2010). Initial rock-physics work done on this well data used a single composition in a contact cement model to represent the mineral grain in the rock-physics model (Carter and Spikes, 2013 and Chapter 4).

However, given the inherent natural heterogeneity of the Cranfield reservoir shown by Kordi et al. (2010), the rock-physics model was expanded to cover the range of documented mineral compositions. To implement these additional compositions I computed the contact cement model 50 times for a range of mineral compositions, ranging from 40% quartz, 40% clay, and a 20% mixture of feldspar and calcite to 100% quartz. A complete list of parameters including the mineral and fluid moduli used to calibrate the rock-physics model can be found in Carter and Spikes (2013) and Chapter 3. A description of the contact cement model and the equations used to calculate the moduli as a function of the physical properties can be found in Chapter 3 and Appendix A, respectively.

Modeling the Cranfield reservoir with the contact cement model consistently with known geology produced results that were inconsistent with known relationships between porosity and clay content. This was due to the lack of pressure dependence of the contact cement model. Numerous studies (e.g., Nur and Simmons, 1969; Nur, 1971; Sayers, 1988; and Mavko et al., 1995) have shown that an increase in confining pressure can cause an increase in seismic velocity due to an increase in intergranular friction and closing of pores and cracks. Alignment of the modeled porosity with the measured porosity required P- and S-wave coefficients to calibrate the model to the measured data from wells F-2 and F-3. Coefficients were chosen that were consistent with the pressure-dependent velocity work completed by Joy (2011) on Cranfield reservoir core samples. The measurements showed that P-wave velocity of core plugs from the Cranfield reservoir increased nonlinearly with an increase in pressure. For differential pressures of 27 to 34 MPa, which are anticipated at 3100 to 3200 meters depth during and after

injection, an increase in P-wave velocity of 8 to 14% is inside the prediction envelope. Shear-wave velocity measurements by Joy (2011) showed less dependence on pressure relative to the P-waves.

Figures 5.6a and b show the contact cement model for all the modeled lithologies with a pore-fluid composition fixed to pure brine. The shallower and deeper sections of the reservoir are shown in panels a and b, respectively. Panels a and b are shaded to porosity with red to blue indicating high to low porosity. Measured data points from their respective zones of the reservoir are overlain in both panels. The data points are colored to the same porosity range as the models. This figure indicates that the modeled porosity and measured porosity correlate closely in both reservoir zones. Additionally it shows that the model covers the range of *Vp/Vs* and *Ip* values present in the data.

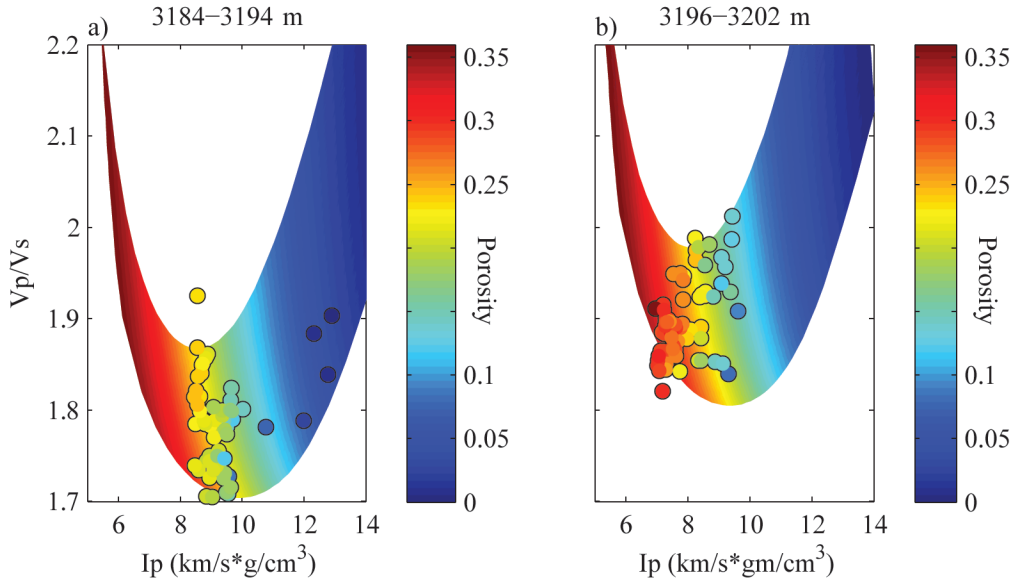

Figure 5.6: Both panels show *Vp/Vs* on the vertical axis and *Ip* on the horizontal axis and are colored according to porosity. Panels a and b represent the shallow and deep portion of the reservoir, respectively, with the modeled values colored according to porosity, with dark red representing high porosity and blue indicating low porosity. The data points shown are measured data from the F-2 well log colored according to the same porosity range as the models.

5.3.5 Porosity and saturation joint inversion

For this study, a statistical approach was used to estimate the pore fluid composition and porosity from *Ip* and *Vp/Vs*. A statistical approach allows for estimating porosity, pore fluid saturation, and the probability of a given combination of the two. The first step of the joint inversion was to compute the models from which to generate the relationships between elastic parameters and reservoir properties. This was done by taking the contact cement models for the range of different mineralogies and porosities shown in Figure 5.6 and completing fluid substitution on them. As a result, each different lithology was modeled for pore-fluid compositions from pure brine to pure CO_2. Data from all the different lithologies and fluid compositions were then binned for certain

ranges of *Ip* and *Vp/Vs*. The number of bins used was based on minimizing nonuniqueness of the data within the bins but also retaining sufficient data to obtain reliable statistical information about the data within the bin. From each bin a bivariate probability density function (PDF) was generated relating porosity and pore-fluid compositions jointly to a given range of *Ip* and *Vp/Vs*. An example of these bins is shown in Figure 5.7. In Figure 5.7, porosity is shown along the y-axis, CO_2 saturation is shown along the x-axis, and joint probability is indicated by color, with black and red indicating higher joint probability. The black data points are the modeled values from within the bin, and the surface represents the probability.

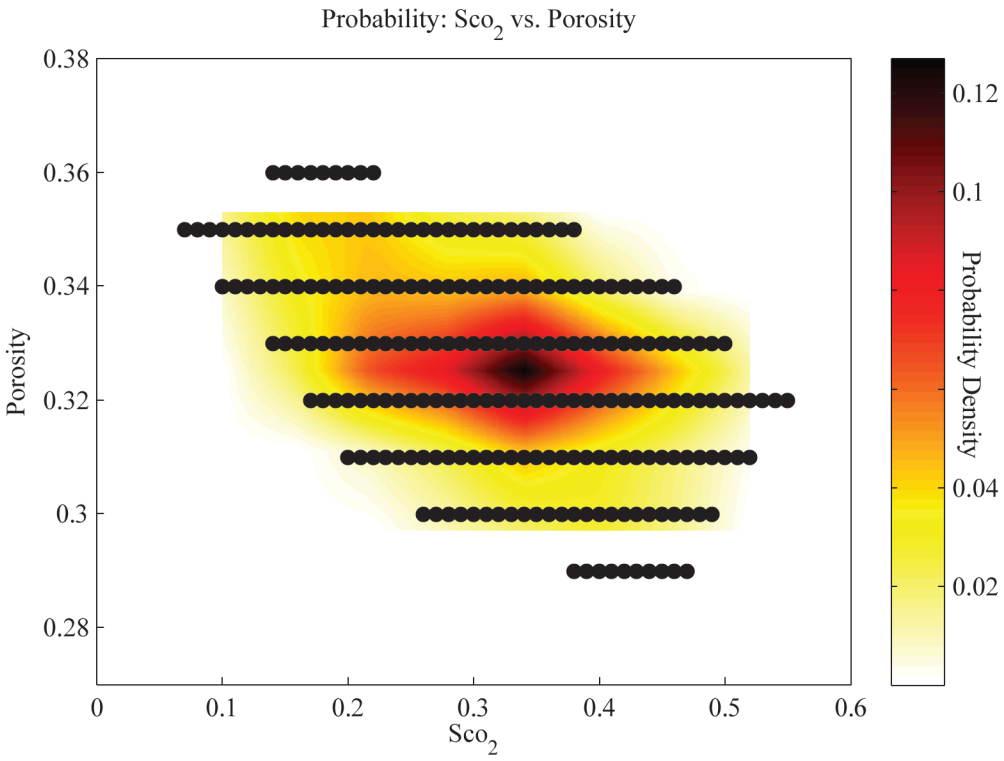

Figure 5.7: The relationship between porosity and fluid saturation for a single bin of the contact cement model. Porosity is shown on the y-axis, CO_2 saturation is shown on the x-axis, and probability is shown by color, with white being low probability density, and black being high probability density. Black data points show the values taken from the model. The surface is a bivariate PDF of the model values shown in the bin.

Measured *Vp/Vs* and *Ip* data were placed in the bins based on their values. Because many saturation and porosity combinations were present in each bin, the bivariate distribution for each bin was sampled. More specifically, 500 joint porosity and fluid saturation values were drawn for each data point. From the 500 bivariate values drawn for each depth point, probabilistic logs of both porosity and pore-fluid composition were compiled. The resultant probabilistic porosity and pore-fluid composition logs show the range of possible porosity and pore-fluid compositions for a given depth point based on the *Vp/Vs* and *Ip* values. After the porosity and pore-fluid logs were generated, they

were smoothed to upscale the results to VSP frequencies. A range of smoothing values was tested to determine the degree needed to best match the inverted and measured porosity logs. Smoothing was accomplished by applying a windowed moving average to the inverted porosity values.

The inversion was calibrated and tested using known porosity values and multiple known pore-fluid compositions. Well log data from well F-2 provided the calibration information. Three different fluid saturations were used. These three were obtained by using Gassmann (1951) fluid substitution from the in-situ saturation to 0, 25, and 50% CO_2 with brine as the remainder. Figure 5.8 shows the results of the joint inversion for the three fluid saturations. Panels a, c, and e show the results of the porosity inversion with calibration pore fluids being 0, 25, and 50% CO_2 mixed with brine. Panels b, d, and f show the results of the inversion for pore-fluid composition for the same calibration fluid saturations as panels a, c, and e, respectively. In panels a, c, and e the x-axis is porosity, and for panels b, d, and f the x-axis indicates water saturation. In all panels the vertical axis is depth, and the green lines are the calibration curves. The shaded region of both panels is the probability of the inversion results returning a given value for a certain depth point. Black and dark red correspond to approximately a P50 value and white to red illustrates the P1-49 values to the left of the P50 line and the P51 to P99 value to the right of the P50 line. Figure 5.9 shows the same information presented in Figure 5.8 with the same shading, except the results in Figure 5.9 have been upscaled to give a high quality match between the measured and inverted values. This upscaling brings the logs to approximately 50 Hz, which is the same range as the VSP data.

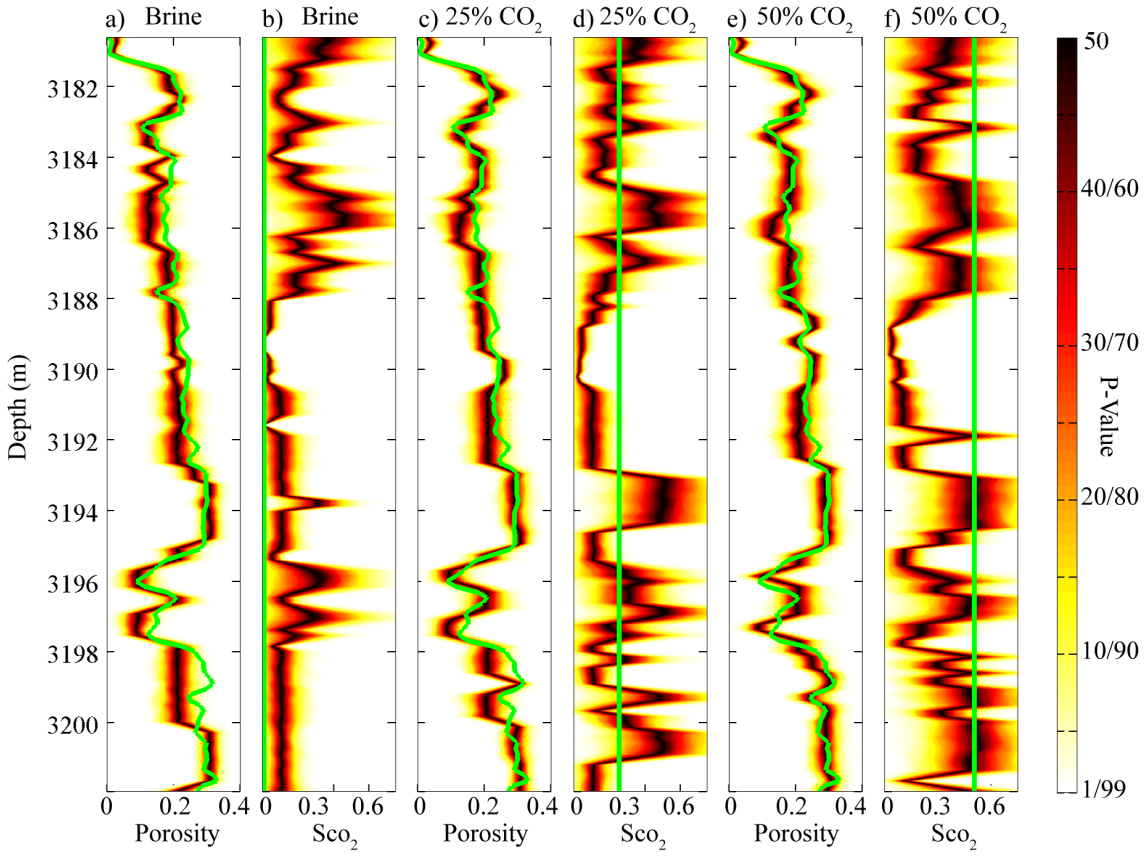

Figure 5.8: Joint inversion results for porosity and CO_2 saturation from calibration data. Panels a, c, and e show porosity results, and panels b, d, and f show the fluid saturation results. The green lines represent the calibration porosity and the calibration fluid-saturation curves that have been fluid substituted to a known and constant fluid composition. Shading in each panel indicates probability of the inverted parameter. From left to right in each panel, white to red to black indicates P1 to P49. P50 is the black line down the center, and black to red to white represents P51-P99 values.

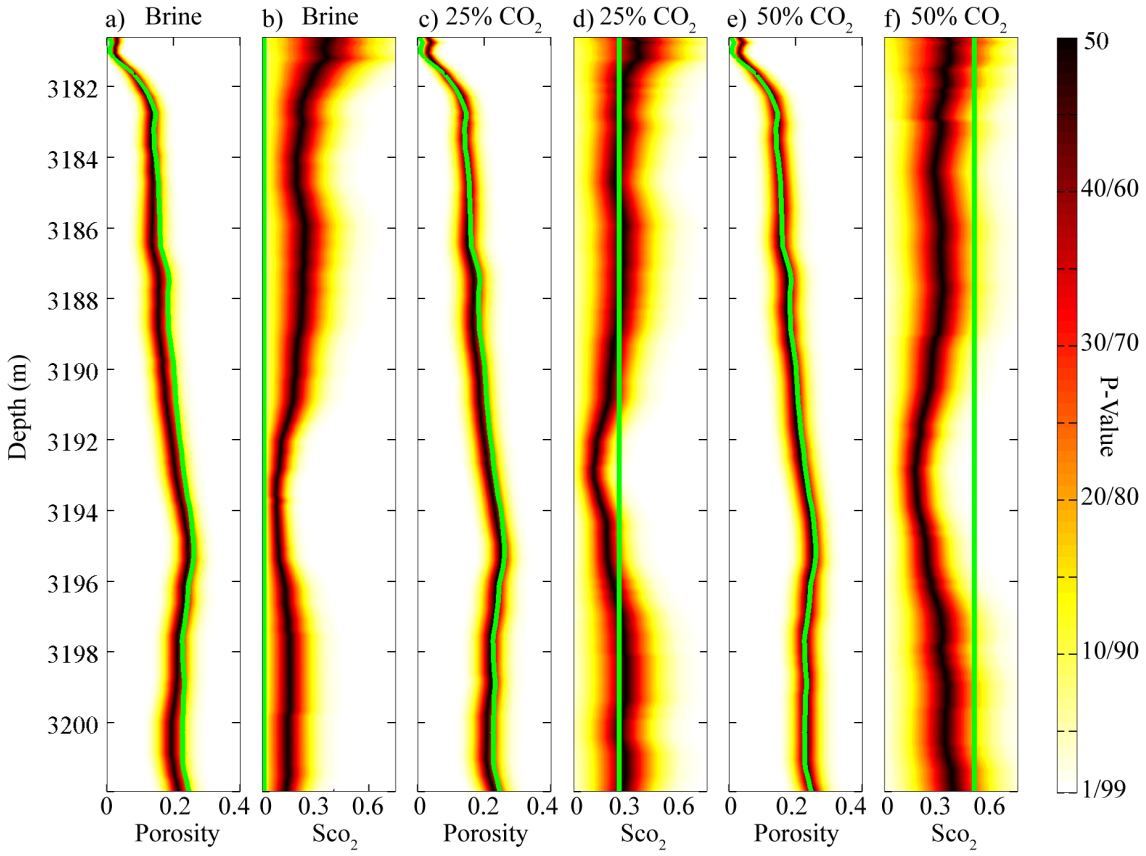

Figure 5.9: This figure shows the same information as Figure 5.8, only upscaled to represent the anticipated VSP data wavelength. The green line in each panel shows the calibration curves, porosity for panels a, c, and e and fluid substituted uniform pore fluid composition for panels b, d, and f. Shading in all panels indicates probability of the inverted result. Black indicates the P50 and white to black shading to the left of the P50 lines indicates P1-P49 probabilities and the black to white shading to the right of the P50 line indicates the range of P51-P99. In all panels depth in meters is shown on the y axis. For panels a, c, and e porosity is shown in the x-axis and for panels b, d, and f water saturation is shown on the x-axis. This figure shows that inverted porosity is relatively accurate, but inverted pore fluid is relatively uncertain.

5.4 RESULTS

Porosity prediction from the joint inversion for all calibration fluid compositions showed relatively reliable results for depths of 3190–3202 m (Figure 5.8). At depths shallower than 3190 m, the modeled porosity in panels a, c, and e slightly under-

predicted the calibration data. For fluid-saturation prediction, the results from the joint inversion tended to return relatively similar results for all three fluid situations, above 3190 m. For the deeper portion of the reservoir, the predicted fluid saturation showed increasing CO_2 saturation in the estimate where the calibration CO_2 saturation was increased. Along with this increase in predicted CO_2 there was also an increase in width of the distribution of predicted CO_2 saturations. Despite the increase in predicted CO_2 with increased CO_2 concentration of the calibration logs, the results did not show a direct one-to-one increase in predicted CO_2 with an increase in CO_2 concentration of the calibration data. Statistical error analysis was not completed on the high resolution results as they were only an interim step in calibrating the model in preparation for inverting the multicomponent data.

Much like their relatively high resolution counterparts in Figure 5.8, panels a, c, and e of Figure 5.9 all showed a good match for the porosity values. For the results shown in Figure 5.9, root mean squared (RMS) error between the modeled P50 porosity value and the measured porosity from the well logs were 2.36, 1.56, and 0.84% for the test calibration situations shown in panels a, c, and e, respectively. Panels b, d, and e, showed that during upscaling much of the high frequency noise was the model is reduced making for a clearer comparison between the inverted fluid saturation and the calibration data relative to the higher resolution well logs. Figure 5.9 demonstrated that as percent CO_2 in the pore fluid of the calibration data increased, the model detected this increased CO_2. The case shown in panel d, with 25% CO_2 and 75% brine as the calibration fluid, showed a close match between calibration and inverted pore fluid composition with an RMS error of only 6% between the modeled P50 pore fluid and the calibration data.

Inverted fluid composition in panel b, with pure brine as the calibration fluid, illustrated that there was an increase in inverted water saturation relative to panel d. Similarly, in the case with a calibration fluid of 50% CO_2 and 50% brine (panel f) the inverted results indicate an increase in CO_2 concentration relative to the 25% CO_2 and 75% brine. In the fluid scenarios modeled in panel b and d, RMS errors of 17.9 and 22.4% resulted between the modeled P50 pore fluid and the uniform calibration fluid. The variations observed in the inverted fluid saturations relative to the calibration fluid illustrates that the model is capable of detecting variations in pore fluid.

This method was applied to the inverted P-impedance and *Vp/Vs* sections obtained from the VSP data. Results from the porosity and fluid saturation inversion at this location of the reservoir can be seen in Figure 5.10. All panels of Figure 5.10 show two-way travel time on the vertical axis and CDP location on the horizontal axis. The black lines running horizontally across all panels represent the top and base of the reservoir as picked from the full 3D PP VSP volume. Well F-1 is located outside of the view in all panels. This well would be located at the equivalent trace index 0. Panels a and c show P-impedance and *Vp/Vs* from shot point 1291 and 1917, respectively, colored by impedance. Panel b shows the P50 porosity with blue representing low porosity values and red indicating high porosity values. In panel d the coloration indicates the P50 of CO_2 saturation in the pore fluid with red indicating higher CO_2 saturations and blue indicating higher percentages of brine. The P50 fluid saturation values show a relatively high percentage of water throughout the reservoir area. In the deeper half of the reservoir is a layer where the model indicates pore fluids of 40–25% CO_2 (60–75% brine). This result is consistent with previous modeling for CO_2 migration in the Cranfield, which

predicted that buoyant rising of CO_2 would not be the dominant cause of migration because of reservoir geometry and permeability (Lu et al., 2013). In the shallower half of the reservoir zone the results indicate that the fluid composition contains a CO_2 percentage less than 25%. The dark blue color in panel c and the corresponding dark red color in panel d between 2270 and 2280 ms and between inlines 62 and 70 indicates an area of the reservoir where the *Ip* and *Vp/Vs* values fall outside the model ranges. Results from this location are not accurate. Pore-fluid compositions and porosity estimates above and below the reservoir, indicated by the black horizontal lines, are not considered accurate because the rock-physics model was not calibrated for lithologies outside the reservoir zone. These zones have been shaded gray.

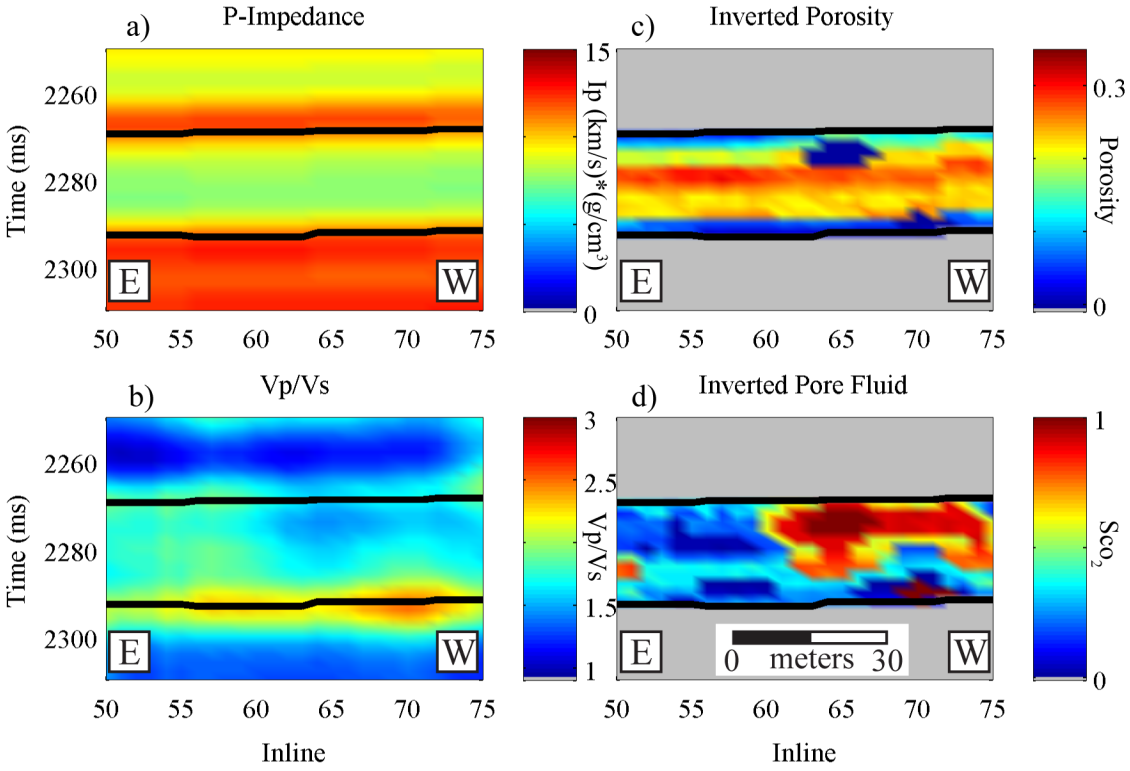

Figure 5.10: Panels a and b show inverted P-impedance and *Vp/Vs* from the multicomponent data, respectively. Inverted porosity and pore fluid from the reservoir zone are indicated in panels c and d, respectively. In panel c, P50 porosity values are indicated by color with red indicating high porosity, and blue indicating low porosity. Panel d shows the same portion of the reservoir as panel c, but it is colored to the P50 value of CO_2 saturation. The dark red location in c and d at approximately 2275 ms and inline 65 is a location in the reservoir where the reservoir parameters fall outside the model calibration. The black lines running horizontally across both panels indicate the top and bottom of the reservoir. In this figure well F-1 would be at inline zero.

The shale layer separating the upper and lower reservoir zones (Figure 5.3) is not visible in the VSP data. I assumed it existed across the seismic line and placed it at 2284 ms. Five time samples on either side of the interface were modeled using both rock-physics models (upper and lower reservoir), and the results were averaged. The inversion was completed for the thickness of the reservoir plus 20 ms above and below to help

capture additional samples that might have been missed due to the picking of the horizons.

5.5 DISCUSSION

The inversion technique provided relatively accurate porosity estimates and constraints on fluid saturation, but the results are somewhat non-intuitive. The porosity estimates primarily correlated with the P-impedance of the reservoir. However, because the inversion provided simultaneous estimates of porosity and fluid saturation, *Vp/Vs* imparts a secondary trend in the porosity estimation. In Figure 5.6 it can be seen how, for a constant *Ip*, estimated porosity will be different depending on the *Vp/Vs* value associated with it. To a lesser extent this is evident by the slight variations in inverted porosity values shown in Figure 5.9, panels a, c, and e.

Inverted fluid saturation results are also somewhat non-intuitive. The concentration of inverted CO_2 in the reservoir is relatively low near the injection well (well F-1) and increases with distance from the monitoring well. A potential explanation for this could be preferential fluid pathways. Hovorka et al. (2011) showed that the Cranfield reservoir is highly channelized. They modeled this channelization to show that injected CO_2 migrated to the more distal monitoring well (F-3) shortly after arriving at well F-2 (Hovorka et al., 2011). The presence of channelization to the west of the injection well (between shot number 1291 and the injection well in Figure 5.1) might explain why the zone nearest well F-1 (smaller inline numbers in Figure 5.10) shows decreased concentration of CO_2 relative to the zone farther away (higher inline numbers in Figure 5.10). During injection, CO_2 was observed at both wells within 13 days of

injection (Hovorka et al., 2011), indicating that presence of CO_2 is realistic over the entire area analyzed by this study. Figure 5.10 provides similar information.

Another explanation for the highly variable inverted fluid-saturation profile seen in Figure 5.10 is the absence of spatial and lateral parameters in the model. The high frequency calibration results of Figure 5.8 show a highly variable result with significantly different fluid saturation estimates at adjacent depth points. The lack of continuity from one data point to the next in the unsmoothed calibration is similar to the final results generated from the multicomponent data. An apparent lack of depth dependence in the calibration data could be translated as a lack of depth and lateral dependence in the final results. This could be a factor in explaining why the fluid saturation does not display a smooth lateral trend.

In the calibration, the joint inversion was completed first, and then the results were smoothed (Figure 5.9). However, in the joint inversion with the multicomponent data, no smoothing took place because the result was already at the desired frequency. The omission of smoothing could be a contributing factor in why the lateral continuity of the final fluid saturation result (Figure 5.10) more closely resembled the fluid saturation estimates in Figure 5.8 (the high-frequency calibration result) than in Figure 5.9 (the lower frequency calibration result). The number of variables in the forward model could be a factor in explaining why the result showed a smooth and laterally continuous porosity model relative to the more discontinuous pore fluid model. In this study it would initially seem that using two input parameters to determine two output parameters would lead to a fully determined problem. However, the calibrated rock-physics model contains multiple lithologies and multiple cement concentrations. Due to the relatively

large number of input parameters, every modeled porosity and pore-fluid combination also has a unique lithology and cement volume associated with it. Therefore, a seemingly fully determined problem is highly underdetermined when all calibration parameters are included. Being underdetermined results in the state of knowledge of the relationship between the variables being decreased relative to an equally determined problem (Takahashi, 2000). The decreased state of knowledge (relative to a fully determined problem) is potentially a reason for why one parameter, porosity, tracks very closely, while the other parameter, fluid saturation, exhibits a significantly increased relative variability. Furthermore, in a joint inversion situation the parameters being estimated tend to be linked (Bachrach, 2006). This linking leads to an under-prediction of one parameter, possibly leading to either an over-prediction or under-prediction of the other parameter. To help improve the accuracy of the fluid-saturation estimate without adversely affecting the porosity estimates, a coefficient on the covariance matrix that generates the bivariate Gaussian random number could be implemented to improve the accuracy of the estimated fluid saturation values (Bachrach, 2006, Spikes et al., 2007).

Reducing the range of uncertainty in fluid-saturation estimates is one way to improve the accuracy and usefulness of this approach for this site and other locations. While this methodology has been shown to provide general trends for fluid composition, the margins of error are still relatively large. To reduce this error a weighting factor might need to be applied to the modeled fluid compositions to increase the sensitivity of the inversion to changes in fluid composition. As an example, if the model predicted a fluid composition of 40% CO_2, a weighting factor could be applied to increase this to 50%. This scaling factor could be varied and calibrated to improve the modeling accuracy of

the range of fluid compositions shown in Figures 5.8 and 5.9. A cause of the lack of sensitivity of the model to changes in fluid composition in the 50-75% brine range can partially be explained by looking the variation in the elastic properties of the reservoir with changes in fluid composition. The host rock of the Cranfield is relatively stiff, and such changes in CO_2 composition can occur with a relatively small variation in elastic properties. This minimal variation in *Vp/Vs* for small to medium changes in the fluid composition is a consistent and well documented challenge in geophysical exploration.

5.6 CONCLUSIONS

This study showed that multicomponent VSP data can be used with the contact cement model to estimate porosity and fluid saturation in the Cranfield reservoir. Additionally this study illustrated that it is possible to selectively choose shot point data from a multicomponent 3D VSP to obtain overlapping coverage of the reservoir with both PP and PS data. The addition of shear-wave data from the multicomponent VSP allowed for relatively high resolution estimates of porosity and fluid composition that would not have been possible to generate using only P-wave data. The high resolution multicomponent VSP data allowed for relatively accurate probabilistic estimates of porosity and pore-fluid saturation, with the latter less accurate than the former.

The joint inversion for porosity and fluid saturation showed a relatively accurate match between inverted and measured values in from the well logs. However, the inverted pore-fluid composition was less accurate than the corresponding inverted porosity values. This situation indicates that although the two parameters in the joint inversion are linked, a weighting coefficient might be necessary to ensure more accurate results for both parameters. The two measurements used in this study, *Ip* and *Vp/Vs*, are

both affected by changes in *Vp*. Although *Ip* and *Vp/Vs* are primarily affected by porosity and fluid saturation, respectively, estimated porosity changes only slightly with changes in fluid saturation because of the effect of fluid composition on P-wave velocity. Additionally, the reduced accuracy of the saturation estimate can be, in part, attributed to the limited sensitivity of the elastic stiffness of the reservoir to fluid saturation. The addition of a weighting coefficient might help to amplify the subtle changes in the reservoir properties due to fluid composition and help improve the inversion for fluid composition. The joint inversion of the 3D VSP data showed reservoir porosities that are consistent with well logs. Additionally, inverted fluid saturation showed the presence of CO_2 in the reservoir. This method currently might not be accurate to determine the percent of CO_2 at any given location in the reservoir. However, inversion of multicomponent VSP data appears to be capable of differentiating between areas that contain CO_2 and those that do not.

Chapter 6: Rock Physics Based Double Difference Inversion for CO_2 Saturation and Porosity at the Cranfield CO_2 Injection Site[1]

6.1 ABSTRACT

Large-scale subsurface injection of CO_2 has the potential to both reduce emissions of atmospheric CO_2 and improve oil recovery. Studying the effects of injected CO_2 on the elastic properties of the saturated reservoir rock can help improve long-term monitoring effectiveness and accuracy at locations undergoing CO_2 injection. This study uses two vintages of existing 3D surface seismic data and well logs to probabilistically invert for the CO_2 saturation and porosity at the Cranfield reservoir using a double difference approach. The first step of this work was to calibrate the rock-physics model to the well log data. Next, the baseline and time-lapse seismic datasets were inverted for acoustic impedance, *Ip*, using a high-resolution basis pursuit inversion technique. Reservoir porosity was derived statistically from the rock-physics model based on the *Ip* values from the impedance estimates derived from the baseline survey. The porosity estimates were used in the double difference routine as the fixed initial model from which CO_2 saturation was then estimated from the time-lapse *Ip* data. Porosity was assumed to remain constant between survey vintages; therefore, the changes between the baseline and time-lapse *Ip* data may be inverted for CO_2 saturation from the injection activities using the calibrated rock-physics model. Comparisons of inverted and measured porosity from well logs indicate quite accurate results. Estimates of CO_2 saturation show less accuracy than the porosity estimates.

[1] This chapter is based on material submitted to for publication under the citation: Carter, R., and K. Spikes, 2014, Rock Physics based double difference inversion for CO_2 saturation and porosity at the Cranfield CO_2 injection site, Under Review. Dr. Spikes provided technical guidance and editing on the work completed in this section.

6.2 INTRODUCTION

Injection of CO_2 into the subsurface for enhanced oil recovery (EOR) or geologic storage and sequestration has the potential to increase oil production from mature fields in addition to contributing to the reduction of anthropogenic CO_2 released into the atmosphere. Recent studies have suggested that injected CO_2 can be accommodated in brine and depleted hydrocarbon reservoirs. This potential has been shown at various sites around the world, including Sleipner (Williams and Chadwick, 2012), Weyburn (Ma and Morozov, 2010 and Verdon et al., 2010), and Krechba (Mathieson et al., 2010). Accurate monitoring of injected CO_2 volumes and CO_2 migration is an important component of any suggested sequestration or EOR project. Remote sensing techniques, in particular surface seismic methods, can potentially provide some of this detailed monitoring capability over large-scale areas where dense well bore coverage would be uneconomical or impractical. Time-lapse seismic techniques might allow for monitoring the lateral extent and changing spatial distribution of injected CO_2 over many years of the life of a project.

Various researchers have focused on monitoring and characterizing injected CO_2 from time-lapse surface seismic data and well logs. Chadwick et al. (2010) quantitatively analyzed multiple observations of data from the Sleipner field and applied a prestack stratigraphic inversion algorithm and compared it to poststack inversion methods. Prestack inversion better characterized thin intra-reservoir mudstone and sand intervals compared to using poststack inversion. Additional work at the Sleipner field was completed by Williams and Chadwick (2012) through the use of a spectral decomposition algorithm to examine individual layers of the thinly stratified CO_2 saturated reservoirs at that location. Their studies detected 'tuning effects' in the seismic

response of the thinly bedded CO_2-saturated layers. Ghaderi and Landrø (2009) examined time-lapse amplitude and travel-time shifts to estimate time-thickness and velocity changes in the Sleipner field. The combination of 4D amplitude and reflection time shifts could discriminate between changes in thickness of the CO_2 saturation zone and velocity changes of CO_2-saturated layers in sand beds. More recently, Daley et al. (2011) compared, simulated, and measured cross-well seismic data to estimate properties of an injected CO_2 plume at the Frio-II project. They generated updated fluid-flow models from the relatively high-resolution cross-well seismic observations.

Information from surface seismic techniques can be correlated to physical rock properties through the use of rock-physics modeling. Frequently, when using rock-physics models to invert for two or more reservoir parameters, multiple independent measurements, such as P and S-wave impedance, are jointly inverted. Joint inversion techniques have been used successfully with rock-physics models to help simultaneously characterize hydrocarbon saturation, porosity, and lithology (e.g., Bachrach, 2006; Spikes et al., 2007; Avseth and Norunn, 2011, and Jiang and Spikes, 2013). The study by Bachrach (2006) used rock physics, stochastic modeling, and a Bayesian estimation method to generate porosity and fluid-saturation maps of expected pay sands. Data came from both surface seismic data and well logs. Results indicated a direct correlation between the uncertainty associated with estimations of porosity and the uncertainty of the associated water saturation. Joint inversion of rock-physics models for distributions of reservoir properties was also used by Jiang and Spikes (2013) in their work on the Haynesville shale. These studies primarily focused on inverting models for lithological parameters or fluid content based on elastic parameters computed from well logs. To

expand the analysis to field scale studies, acoustic and elastic impedance inversions of surface seismic data can be used along with well log measurements.

Reflection seismic inversion techniques are often based on forward modeling because of their computational efficiency (Hampson et al., 2005). In the forward modeling approach, at least one well is needed for calibration. The final impedance result is obtained through an iterative approach where synthetic and real data are compared until the misfit is minimized. Other techniques, which are better optimized to yield higher resolution results, take additional time and often require significant increases in computational power (Tao et al., 2013). One of these methods, basis pursuit inversion, uses a high-resolution inversion algorithm to help resolve small changes in elastic properties in the area of interest (Zhang and Castagna, 2011). The approach also resolves thin layers.

Another approach, deployed here, is double difference inversion. A double difference inversion minimizes the introduction of noise into the final impedance estimates by using the relatively complete inversion result from the baseline dataset as the starting model for inverting subsequent surveys over the same subsurface volume (Tao et al., 2013). Double difference inversion is often used in passive source geophysical investigation of Earth structure where data are limited (Calò et al., 2013 and Allam and Ben-Zion, 2012). Calò et al. (2012) used double difference tomography to develop P- and S-wave velocity models of the deep crust and shallow mantle in southern Italy. Double difference inversion of earthquake arrival times was used along the southern California plate boundary and the San Jacinto fault to examine velocity structures in the region (Allam and Ben-Zion, 2012).

Recently, double difference inversion has been applied to exploration scale surface seismic data because of its computational efficiency and its ability to detect subtle temporal changes between successive datasets (Denli and Huang, 2009 and Zheng et al., 2011). Denli and Huang (2009) conducted a full-waveform double difference inversion of multiple vintages of synthetic seismic data in the time domain. Their inversion provided a quantitative analysis of the changes between the datasets as opposed to the qualitative changes observed in more traditional time-lapse studies. Full-waveform double difference inversion for both P- and S-impedance of ocean bottom cable data from the Valhall field was conducted by Zheng et al. (2011). They found that the double difference method showed enhanced resolution and accuracy of the velocity differences between time-lapse surveys compared to using either the same starting model or independently derived starting models.

In my study the double difference approach was adapted to work with rock-physics modeling to help quantify the CO_2 saturation at the Cranfield reservoir. First, the baseline and time-lapse datasets were inverted for P-impedance (*Ip*). Porosity was computed from the baseline *Ip* using a rock-physics model. Porosity was assumed constant over time between the seismic surveys. Therefore, the observed difference between the two inverted impedances corresponded solely to changes in CO_2 saturation, which was computed from the rock-physics model. Differences between the two vintages of seismic data could also be related to changes in the signal to noise ratio, fold, or acquisition geometry, which is considered noise.

6.3 METHODOLOGY

This study consisted of four primary steps. For the first step I selected and calibrated a rock-physics model for the Cranfield reservoir interval. The baseline (first survey) and time-lapse (repeat survey) surface seismic datasets were then inverted for *Ip*, and the *Ip* volumes were then registered to each other. In step three I inverted the impedance values from the baseline seismic survey for porosity using the rock-physics model. The fourth and final step was to use the porosity volume from step three, combined with the inverted impedance volume from the time-lapse data, to estimate CO_2 saturation in the reservoir from the same fixed rock-physics model. The double difference formulation, therefore, was comprised of the initial inverted porosity model with the time-lapse inverted impedance values.

This study uses two vintages of 3D surface seismic data that were acquired over the entire Cranfield area, denoted by the black box in Figure 6.1. Selected cross-line and inline profiles are presented here in addition to horizon extractions along seismic reflections on the top of the reservoir. The selected cross-line and inline profiles in this study are shown as east-west and north-south dashed lines, respectively, in Figure 6.1. In addition to the surface seismic information, this study uses well logs from within the DAS study area in addition to well logs from producing portions of the field. The wells used in this study are F-2, F-3, and 28-1. The first vintage of seismic data was acquired in 2007, and the time-lapse dataset was acquired in 2010. At the time of acquisition of the time-lapse survey, approximately 2.2 million tons of CO_2 had been injected over the whole field. This study aims to define the location and saturation of the injected CO_2 at the time of the time-lapse survey acquisition in 2010.

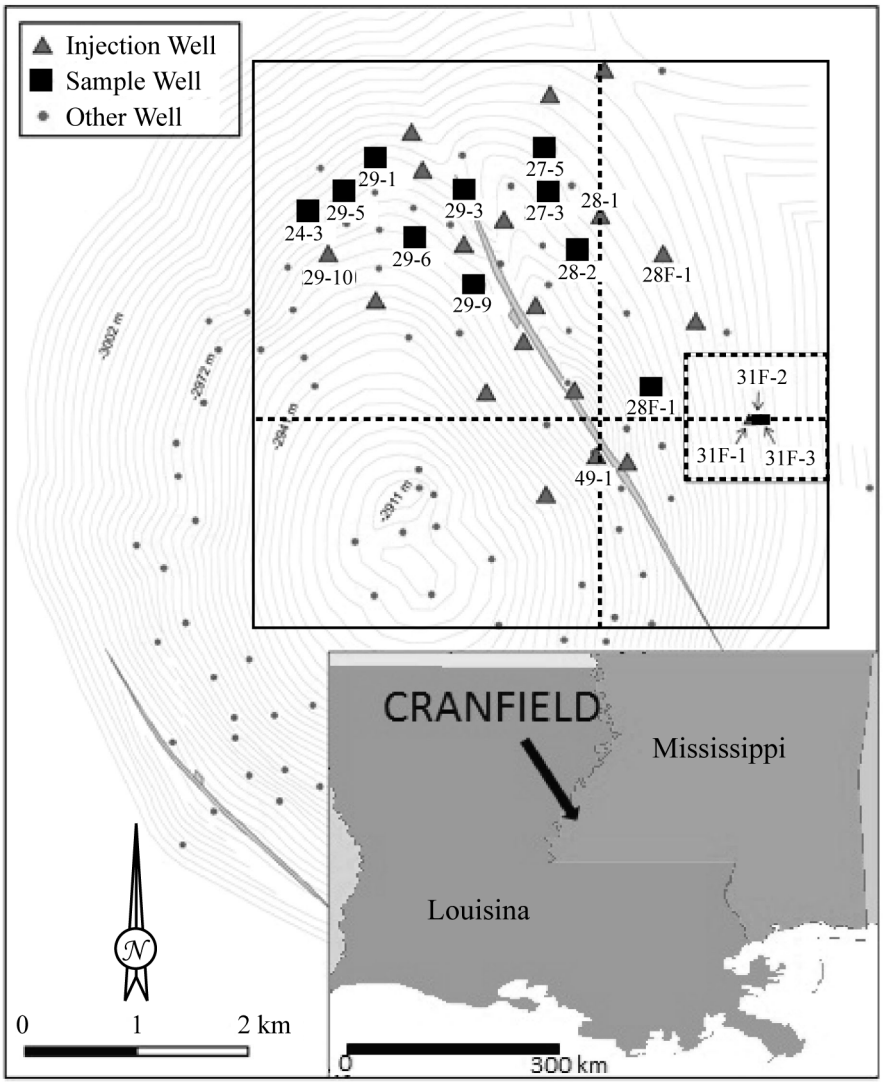

Figure 6.1: Cranfield area map. The dashed box outlines the detail area study, which contains the injection well F-1 and the two monitoring wells F-2 and F-3. Gray triangles indicate the location of injection wells, black squares indicate monitoring wells, and small dots indicate additional wells. The black perimeter box shows the approximate extent of the baseline and time-lapse surface seismic surveys. The dashed east-west and north-wouth oriented lines indicate cross-line 197 and inline 1084, respectively, which are shown in this study. A sealing fault crossing the field is shown by the gray line running diagonally across the larger study area.

6.3.1 Rock-Physics Modeling

Contact-theory models are a subset of rock-physics models that calculate the stiffness of a clastic rock as a function of its constituent parts and composition. These

parts and composition include the elastic moduli of individual spherical grains and intergranular cement, the number of inter-grain contacts per grain, porosity, and overburden pressure acting on those spherical grains (Dvorkin et al., 1994 and Dvorkin and Nur, 1996). We chose the contact cement model (Dvorkin and Nur, 1996) for this study. The contact cement model was derived from Hertz-Mindlin theory (Mindlin, 1949). The original Hertz-Mindlin equations contained a pressure term in the calculation. During the derivation of the contact cement model (CCM), a grain contact cement term was added at the expense of the pressure term. A complete and comprehensive list of these derivations can be found in Dvorkin and Nur (1996).

Figure 6.2 shows the *Ip* and porosity from wells F-2, F-3, and 28-1. Panels a, c, and e show *Ip* for wells F-2, F-3 and 28-1, respectively, whereas panels b, d, and f show the measured porosity from the same wells. The horizontal lines in each panel denote the top and bottom of the reservoir zone. Grain mineralogy in the model was chosen to be consistent with observed mineralogies from petrographic work completed on well F-2. Kordi et al. (2010) showed the reservoir in well F-2 to be comprised of 60–80% quartz, 10–20% clay, 10–20% feldspar, and small percentages of muscovite, calcite, and other minerals. A comprehensive overview of rock-physics modeling parameters can be found in Chapters 3 and 4, Carter and Spikes (2013), and Carter et al. (2014). Figure 6.3 contains the rock-physics modeling results for a 100% brine-saturated model for the porosity range of 10 to 37% and the intergranular cement range of 0 to 27%. The x-axis shows porosity and the y-axis shows *Ip*. The shaded surface corresponds to the modeled quartz content. Blue and cool colors indicate high concentrations of quartz in the matrix, and the red end member indicates 40% quartz with the remaining minerals a mixture of

feldspar, clay, and calcite. The black data points on both panels are the measured porosity values from wells F-2, F-3, and 28-1. Panel b of Figure 6.3 shows the porosity distribution for a narrow range of *Ip* values from the model results.

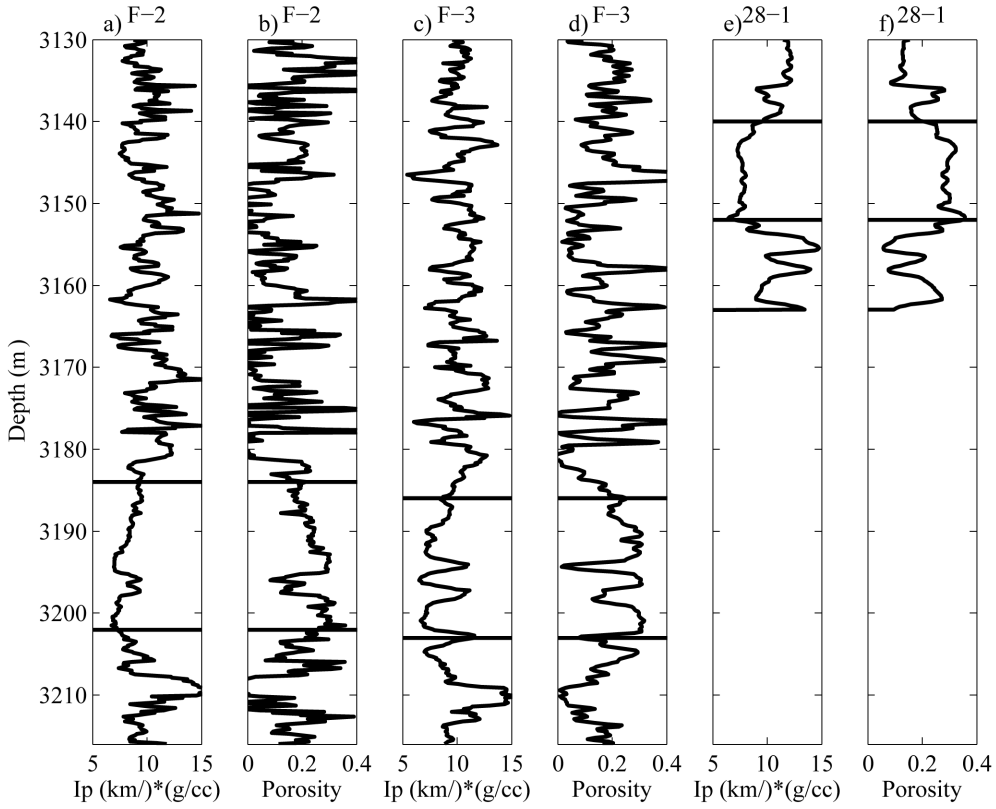

Figure 6.2: Well logs from wells F-2, F-3, and 28-1. Panels a, c, and e show *Ip* from wells F-2, F-3, and 28-1, respectively, while panels b, d, and f show density porosity from wells F-2, F-3, and 28-1, respectively. The horizontal bars in all six panels denote the top and bottom of the reservoir zone in each well.

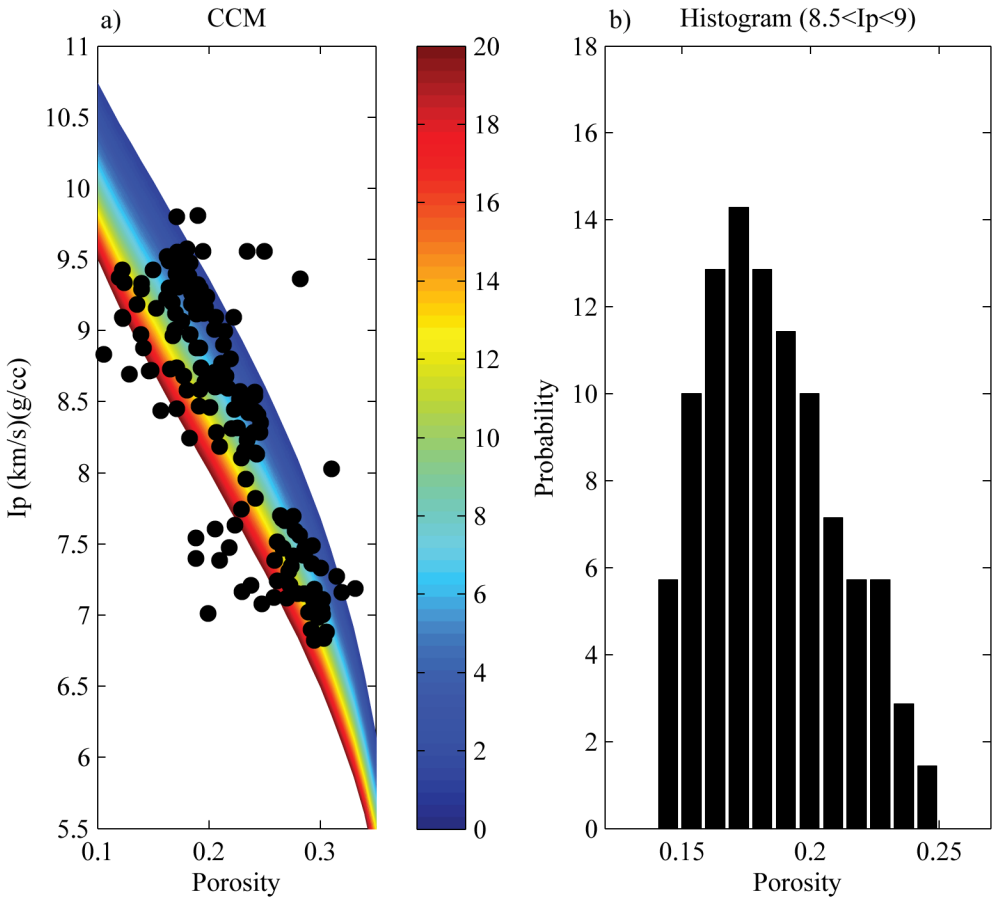

Figure 6.3: Calibrated rock-physics models. Panel a shows the calibrated model for the reservoir. Panel a shows porosity on the x-axis and *Ip* on the y-axis. The shaded region is colored to mineralogy and ranges from pure quartz (blue) to 40% quartz and a clay, feldspar, muscovite mix (red). The black data points are measured data from wells 28-1, F-2, and F-3. Panel b shows the distribution of porosities generated by the model for a narrow range of P-impedance values between 8.5–9 km/s*g/cc.

6.3.2 Basis Pursuit Inversion

Seismic impedance inversion provides a way to extract acoustic and/or elastic impedance values from a reflectivity series. For this study, baseline and time-lapse surface seismic reflection data were inverted for *Ip* using the basis pursuit inversion (BPI) algorithm (Zhang and Castagna, 2011). The BPI algorithm was used because it is optimized to work with thin beds and thin-bed reflectors (Zhang and Castagna, 2011).

BPI uses a set of even and odd wedge dictionaries to compare high-resolution modeled traces to lower resolution measured traces (Figure 6.4). Unlike traditional inversion methods where the interference caused by thin beds degrades seismic resolution, the BPI approach provides useful information about sub-resolution layer thickness and impedance (Zhang and Castagna, 2011). In Figure 6.4 the decomposition of a seismic trace into its respective odd and even traces is shown in panel a. Panels b and d show the odd wedge model and the odd wedge dictionary, respectively. Panels c and e show the same information as panels b and d, but they illustrate the even wedge dictionary.

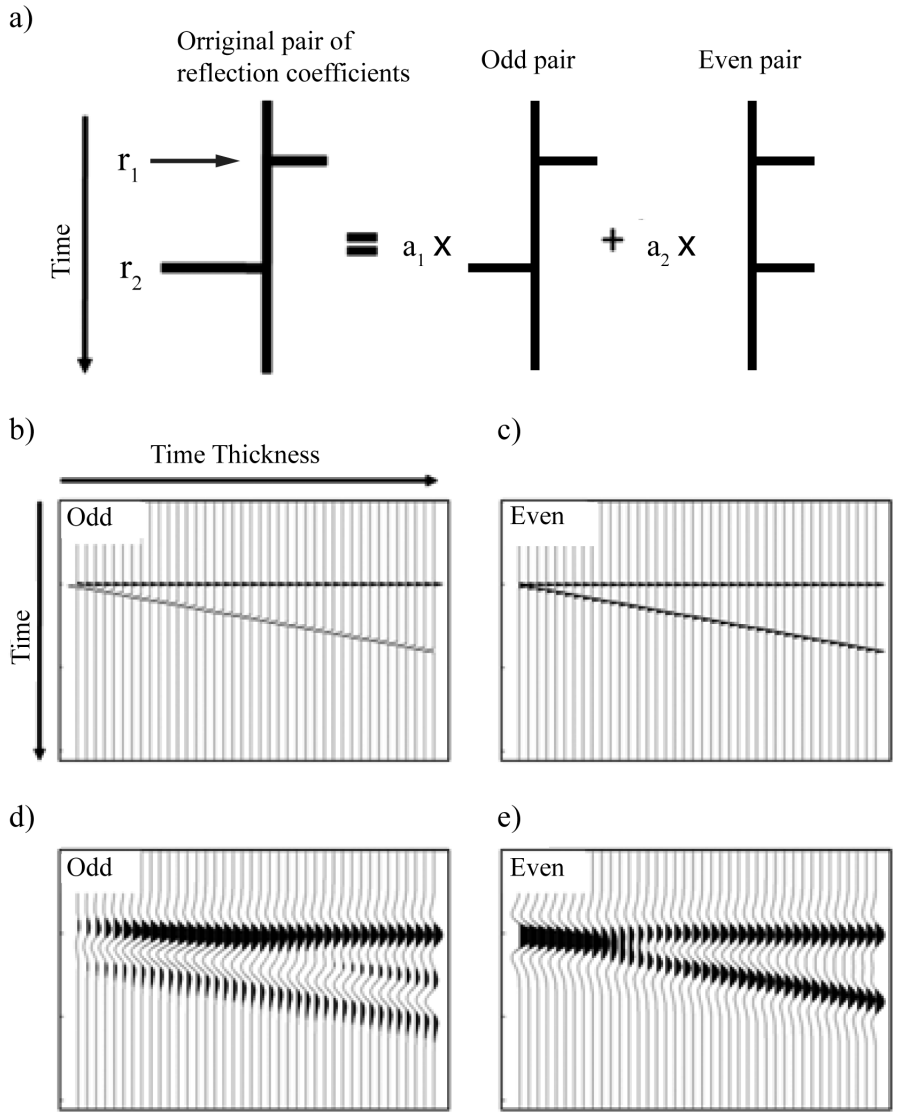

Figure 6.4: Panel a shows how a given seismic reflectivity series can be decomposed into the summation of a weighted even reflectivity series and a weighted odd reflectivity series. In panels b and c the base wedge model is shown. Panel b shows the odd wedge model and panel c shows the even wedge model. By convolving a known wavelet with the models in panels b and c, the odd and even wedge dictionaries are formed and are shown in panels d and e, respectively. Adapted from Zhang and Castagna (2011).

The BPI algorithm works by integrating the wedge dictionary with an L_1-norm optimization method (Zhang et al., 2013a). The objective function for the inversion algorithm is shown in Equation 6.1 and has been adapted from Zhang et al. (2013a).

$$min[\| \mathbf{d} - \mathbf{Wm} \|_2 + \alpha \| \mathbf{m} \|_1] \quad (6.1)$$

In Equation 6.1, **d** is the seismic trace, **W** is the wavelet kernel matrix, which is constructed from the wedge dictionary, **m** is the vector of reflection coefficients, and α is a weighting factor. In this equation it is possible to minimize both the L_1-norm and the mean square error because of the addition of the weighting factor.

In BPI the wedge dictionary is used to deconstruct each seismic trace into a sequence of decomposition coefficients. A final thin-bed reflectivity vector is then reconstructed using the same decomposition coefficients. The coefficients are high-resolution even and odd reflectivity series for each trace. These two series are converted into a high-resolution impedance estimate volume of the subsurface through the incorporation of a low-frequency initial model (Zhang et al., 2013b). A complete and detailed explanation and overview of BPI can be found in Zhang and Castagna (2011).

Inversion volumes of *Ip* for the project presented here were computed and presented in Zhang et al. (2013a) and are presented in later in this chapter. In preparing the volumes for the study presented here, three post-inversion processes were applied after registration to each other to help improve their quality. These three steps were trace smoothing, muting, and scaling. Basis pursuit inversion is a trace-by-trace operation. Because of the trace-by-trace operation of the BPI algorithm, a 3-trace by 3-trace moving

window weighted average was applied to both the baseline and time-lapse inversion volumes to smooth any lateral variation artifacts. In addition, a trace was muted in both the baseline and time-lapse *Ip* volumes if the corresponding trace in either the baseline or time-lapse seismic data had less than seven fold. Seven fold was chosen to be the cutoff value to remove the noisiest data while still preserving as much surface coverage as possible. An additional data-conditioning step compensated for changes between the baseline and time-lapse *Ip* volumes that were not possible due only to changes in CO_2 saturation alone. Changes between the baseline and time-lapse *Ip* volumes could be due to reservoir pressure, geophone coupling, source variations, survey geometry variations, or even the inversion algorithm converging on a different minimum. To minimize the differences, the impedance difference volume was scaled so that the largest observed difference was less than the maximum change due to 100% CO_2 saturation calculated from the rock-physics model. Additionally, the scaling factor was a uniform field scale correction for *Ip* that helped to compensate for changes due to increased pore pressure from injection. The scaling factor was consistent with the observed percent change in *Ip* with a 3–7 MPa increase in pore pressure (reduction in differential pressure) as outlined by Joy (2011).

6.3.3 Porosity Inversion

Estimates of porosity were calculated from the baseline inverted impedance volume using a statistical rock-physics approach. The statistical approach estimated a range of porosities from the *Ip* volume to capture the natural variability of the reservoir, to account for error in the data and the model, and to account for error between the model and the data. The probabilistic porosity estimates include a range of porosities at each

location with their associated uncertainties. To generate the porosity distributions, the rock-physics model was binned according to narrow ranges of *Ip*. An example of the distribution of one of these bins is shown in Figure 6.3 panel b where the selected *Ip* range from the model is 8.5 to 9 (km/s)(g/cc). For every bin we generated a probability density function (PDF) of porosity, given impedance, by fitting a normal Gaussian distribution to the range of porosities within the bin. After a PDF of porosity was generated for each bin, inverted *Ip* values from the baseline survey were input into the rock-physics model. Each inverted *Ip* value was compared to the model bins to determine the impedance ranges to which it belonged. Two hundred random porosity values were then generated based on the mean and standard deviation of the Gaussian PDF of its respective bin. These 200 porosity values provided the mean and standard deviation of expected porosity values at each measured sample in the reservoir.

6.3.4 Double Difference Inversion For CO_2 Saturation

In a typical double difference impedance inversion approach, the final impedance model from one dataset is used as the initial model for inverting the second dataset. Equation 6.2 shows the double difference theory, which has been adapted from Tao et al. (2013).

$$s_{\text{time-lapse}} = f(m_{\text{baseline}}) + \Delta s_{\text{observed}} \tag{6.2}$$

In Equation 6.2 the time-lapse surface seismic data, $s_{\text{time-lapse}}$, can be shown as a combination of the baseline model, $f(m_{\text{baseline}})$, plus the difference between the baseline

and the time-lapse volume ($\Delta s_{\text{observed}}$). In the study presented here we rearrange Equation 6.2 and perform some substitutions to obtain Equation 6.3.

$$f(fl) = f(\phi, fl) - f(\phi) \tag{6.3}$$

From Equation 6.2 to Equation 6.3, $f(m_{baseline})$ has been replaced with $f(\phi)$, $s_{time-lapse}$ has been substituted with $f(\phi, fl)$, and $\Delta s_{observed}$ becomes $f(fl)$. Simple rearrangement of Equation 6.2 with these substitutions then yields Equation 6.3. In Equation 6.3, $f(\phi)$ is the porosity volume computed from the baseline *Ip* data. The term $f(\phi, fl)$ is derived from the time-lapse impedance volume and is a function of both porosity and CO_2 saturation. Subtracting $f(\phi)$ from $f(\phi, fl)$ leaves the residual, $f(fl)$, which is a function of only CO_2 saturation.

The first step of this double difference approach was to apply fluid substitution (Gassmann, 1951) to the calibrated rock-physics model. Fluids ranging from pure brine to pure super critical CO_2 were used for fluid substitution. This step returned a rock-physics model that provided the relationship between *Ip* and porosity for all fluid combinations between pure brine and pure CO_2 for all different mineralogy combinations and cement concentrations.

An example of this process is shown in Figure 6.5. In Figure 6.5 panel a, porosity is shown on the x-axis, and *Ip* is shown on the y-axis. The black lines show the CCM for different mineralogies with pore space saturated with brine. An example data point from the baseline survey is shown by the black circle, and its associated model line is shown in red. Panel b has the same axis as panel a. In panel b, the rock-physics model highlighted

in red from panel a is expanded with fluid substitution and shaded by pore fluid, where red indicates pure brine and dark blue indicates pure CO_2. The black bar in panel b gives the range of *Ip* values and their respective pore fluids for the example data point shown in panel a. The *Ip* value from the inverted time-lapse data determines the location on this black bar where the fluid composition in the reservoir most closely falls.

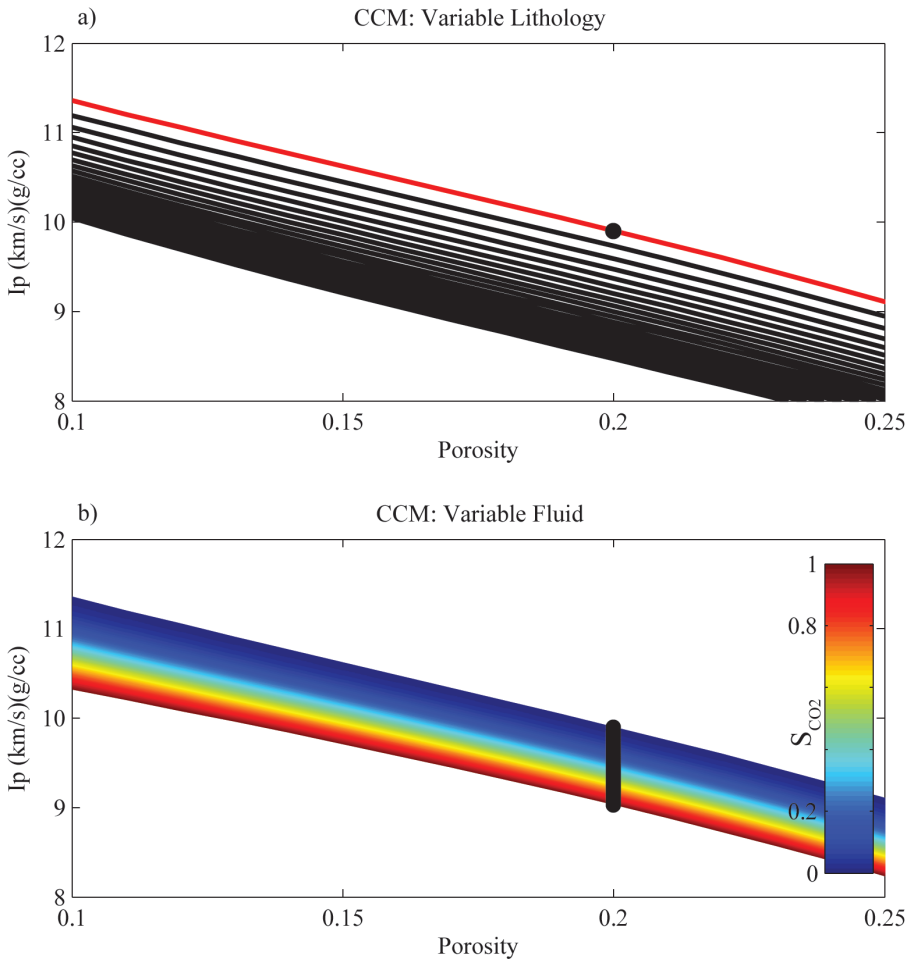

Figure 6.5: Panel a shows the CCM for a range of mineral compositions from pure quartz to a quartz clay mixture. Panel b shows the CCM for a single mineral composition (pure quartz) but for a range of CO_2 saturations. In both panels the y-axis shows *Ip*, and the x-axis shows porosity. In panel a, a single model line is highlighted in red, and a data point indicating a single porosity and impedance combination is shown corresponding to that model line. In panel b the model line from panel a is expanded to cover a range of fluid saturations from pure brine (blue) to pure CO_2 (red). The black vertical bar in the panel highlights the same porosity point as in panel a, and shows the range of *Ip* values that can be expected for the range of CO_2 saturations.

After expanding the rock-physics model to contain variations in fluid saturation, the model was used to estimate CO_2 saturation from the time-lapse seismic data. For every data point in the reservoir and surrounding area in the baseline surface seismic

data, 99 different probable values of porosity were generated from the 200 Gaussian random porosity values modeled. Each data sample in the inverted baseline surface seismic survey has a single *Ip* value and 99 different modeled porosity probabilities. Comparisons of each porosity probability and *Ip* value to the brine-saturated rock-physics model gave a single mineralogy to that combination of porosity and *Ip*. With this association made, each generated porosity and mineralogy combination was compared with its corresponding *Ip* value from the inverted time-lapse dataset to generate the CO_2-saturated rock-physics model. The combination of these three parameters constrained the inversion of CO_2 saturation for a given porosity and mineralogy combination from the time-lapse impedance.

6.4 RESULTS

6.4.1 Impedance Inversion

Registration, muting, and scaling the two impedance volumes produced impedance volumes where the baseline impedances at locations of well control were similar to measured *Ip* values from the wells. At locations of well control the root mean square (RMS) error between the measured baseline *Ip* and the baseline inverted *Ip* ranged from 0.53 to 1.54 (km/s)(g/cc), which is 5.6 to 17%. Away from locations of well control the differences between the baseline and time-lapse impedance volumes were primarily constrained to areas of anticipated CO_2 accumulation. Due to effects of injection, the largest variations between the two volumes were at locations of injection wells. A single east-west oriented cross-line (197) and a north-south oriented inline (1084) from the inverted volumes are shown in Figures 6.6 and 6.7, respectively, while an extraction across the top of the reservoir is shown in Figure 6.8. In all three figures, panel a shows

the baseline impedance data, panel b shows the time-lapse impedance data, and panel c shows the difference between the baseline and the time-lapse data. The black lines running across all panels in the vertical profiles in Figures 6.6 and 6.7 show the top and bottom of the reservoir. The intersection of the cross-line and inline is shown by the vertical dashed line in all panels. In Figure 6.6 the horizontal axis is inline number whereas in Figure 6.7 the horizontal axis is cross-line number. In Figure 6.7 the single solid vertical line is well 28-1. In Figure 6.8 the east-west axis (x-axis) is inline number and the north-south axis (y-axis) is cross-line number. The location of injection wells 28-1 and F-1 are shown by the white dots. In Figure 6.6 two vertical black lines and the single vertical gray line are, from left to right, wells F-1, F-2, and F-3. In panels a and b of all three figures, the relatively low impedance of the reservoir zone can be seen by the black color, while the relatively high impedance of the confining layers can be seen by the warmer colors. In panel c of both figures, red color shows where the baseline data has higher impedance than the time-lapse, and black and gray shows where the time-lapse data has a higher impedance than the baseline data.

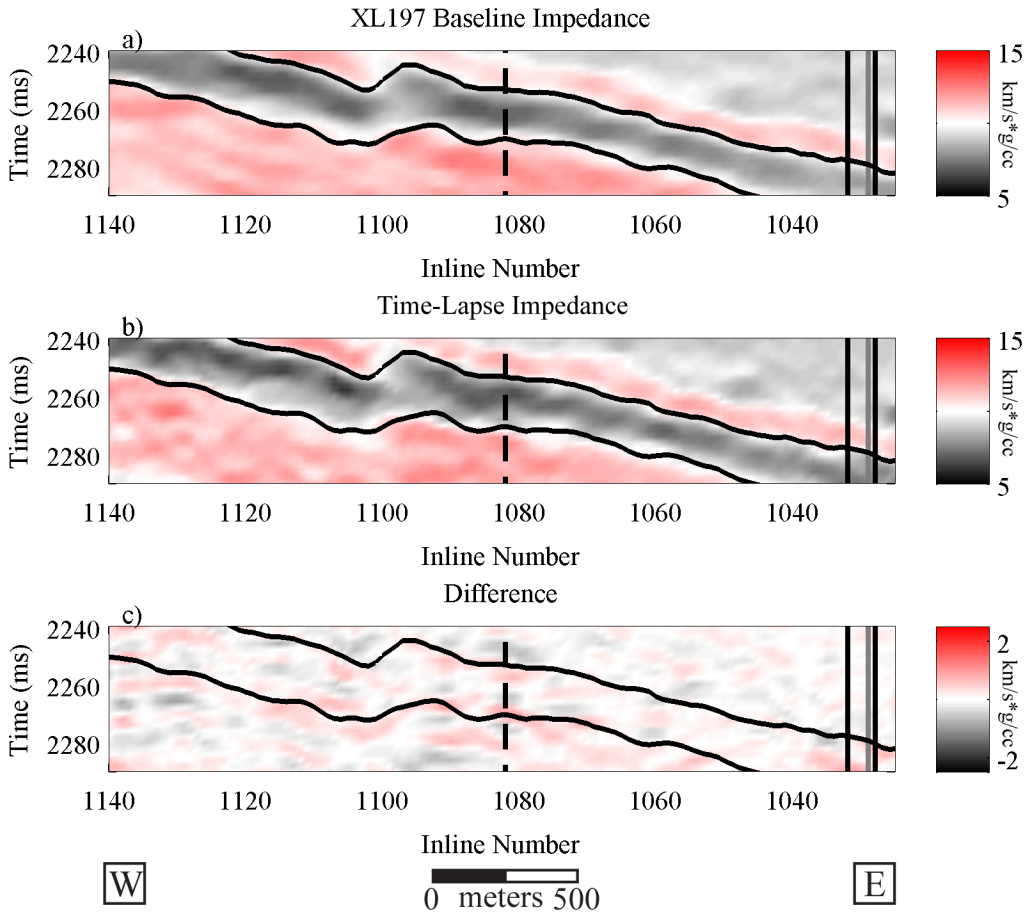

Figure 6.6: Results from the BPI inversion for cross-line 197. Panel a shows the baseline impedance, panel b shows the time-lapse impedance, and panel c shows the difference between the baseline and the time-lapse impedances. In all panels inline number is on the x-axis, and two-way time is on the y-axis. The thin pseudo-horizontal black lines are the picked top and bottom of the reservoir. The two vertical black lines and one gray line are, from left to right, wells F-1, F-2, and F-3. The vertical dashed line shows the intersection of inline 1084.

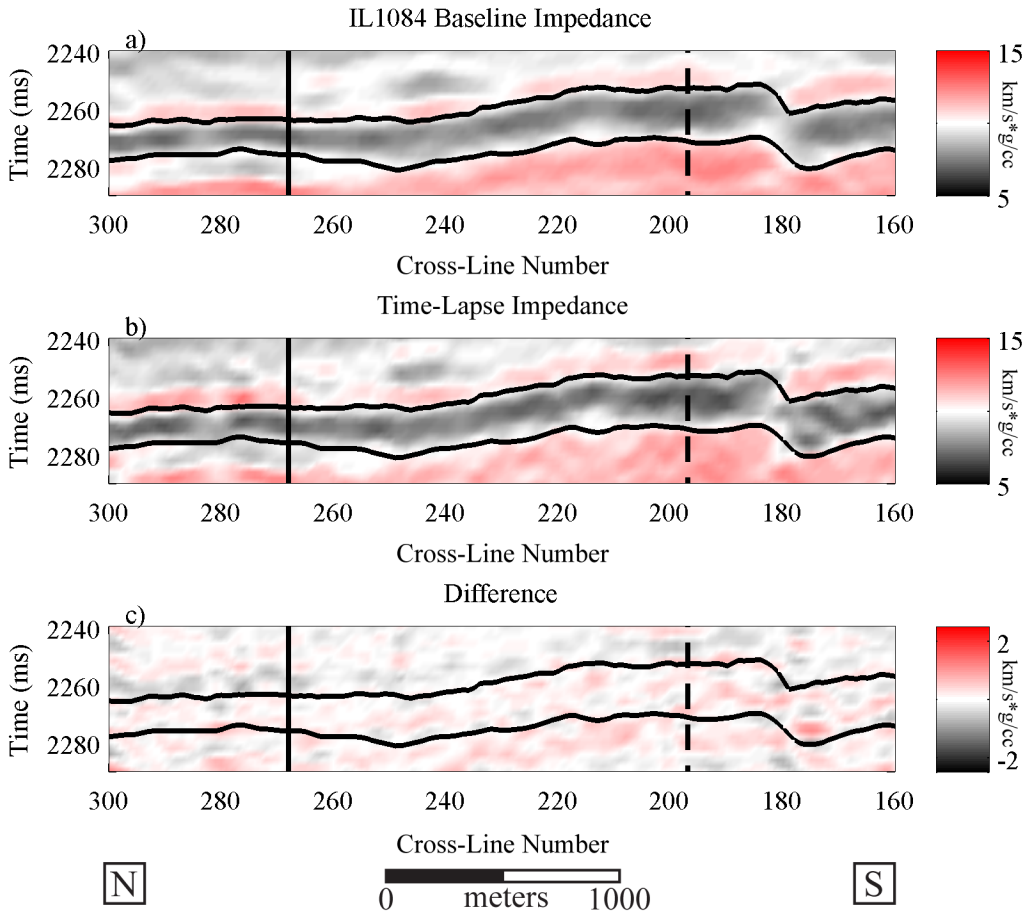

Figure 6.7: Impedance results for inline 1084 from the BPI. Panels a, b, and c, show the baseline, time-lapse, and impedance difference between the two, respectively. All panels show time on the vertical axis and cross-line number on the horizontal axis. Injection well 28-1 is shown by the black vertical line, and the intersection with cross-line 197 is shown by the dashed vertical black line. The top and bottom of the reservoir are denoted by the black lines running horizontally across all panels.

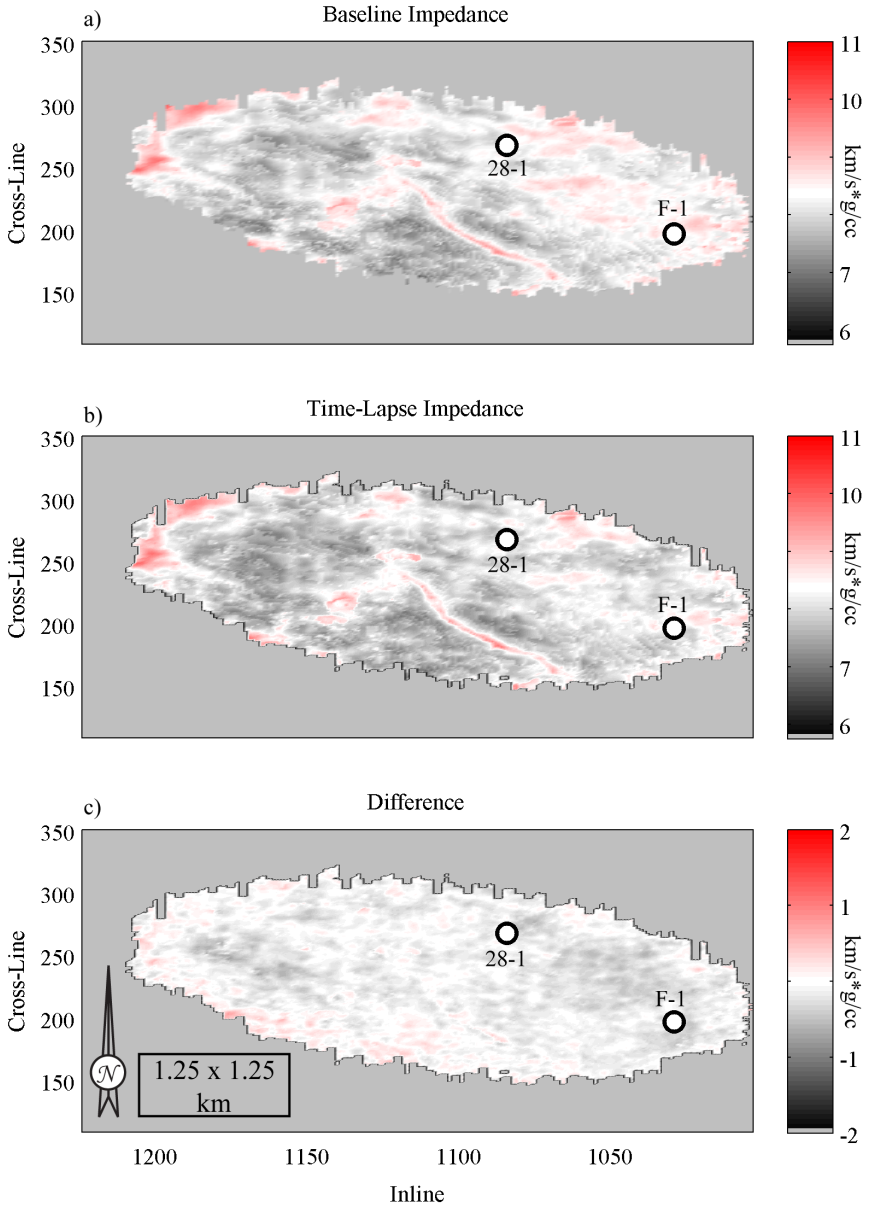

Figure 6.8: Impedance extractions across the top of the reservoir. Panel a and b show the baseline and time-lapse impedance, respectively, while panel c shows the difference between the two volumes. In all three panels inline number is shown on the horizontal axis, and cross-line number is shown on the vertical axis. Injection wells F-1 and 28-1 are shown by the white dots. Color in all three panels show red as high impedance and black as low impedance. The black rectangle in panel c gives the scale for all panels.

6.4.2 Porosity Inversion

The statistical approach in this study resulted in a distribution of inverted porosity values for each baseline *Ip* measurement. The distribution of 200 randomly drawn porosity values provided the range and probability of a given porosity at each bin location. A separate porosity volume was generated for each of the P1 through P99 porosity scenarios. Comparison of the resultant P50 porosity to well log measurements is shown in Figure 6.9. In Figure 6.9, panels a, c, and e show the porosity as the shaded region, and the measured porosity from the well logs as a green line for wells 28-1, F-2, and F-3, respectively. The estimated porosity is colored to probability with black representing the P50 porosity and the yellow on the left and right of the P50 line representing the P10 and P90 probabilities, respectively. Panels b, d, and f show baseline measured impedance, baseline inverted impedance, and time-lapse inverted impedance in the black, green, and red lines, respectively. In all panels of Figure 6.9 the observed data from the well logs has been upscaled to a frequency content similar to that of the inverted data, approximately 50 Hz. The reservoir interval is marked by the two horizontal black lines in all panels. RMS error estimates between the modeled P50 result and the upscaled measured porosity within the reservoir zone was 0.7, 1.2, and 2.1% porosity for wells 28-1, F-2 and F-3, respectively. The RMS error for well F-3 is higher than the others in part because of the mismatch between the measured porosity and the estimated porosity at the top of the reservoir. The mismatch is primarily a function of upscaling the measured porosity data from well log to seismic frequency. Additionally, Figure 6.9 shows that the range of probabilistic porosities is fairly narrow, with the difference between the P10 and the P90 values rarely exceeding 10% of the base porosity. In all three wells, in areas

where the inverted impedance deviates from the measured impedance, there is a mismatch between the measured porosity and the modeled porosity.

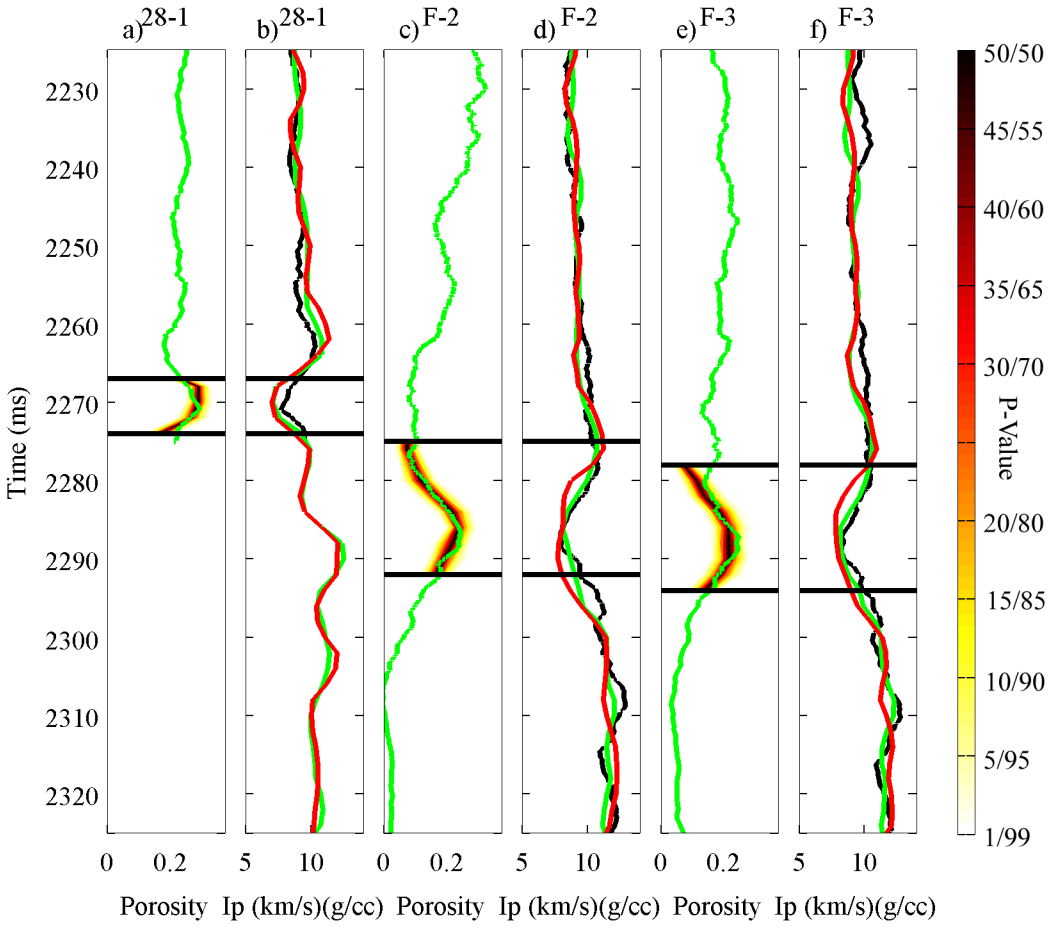

Figure 6.9: Panels a, c, and e show the observed density porosity from wells 28-1, F-2, and F-3, respectively, in green, and estimated porosity probability by color. Color represents the P-value porosity probability with black representing the P50 value. Panels b, d, and f show the measured (black), baseline (green), and time-lapse (red) impedance for wells 28-1, F-2, and F-3, respectively. The reservoir zone is located between the black horizontal lines in all panels.

Porosity estimates from cross-line 197 (east-west) and inline 1084 (north-south) are shown in Figures 6.10 and 6.11, respectively. Figure 6.12 shows the RMS average

porosity estimate calculated from the upper four sample points across the top of the reservoir. Because the P50 porosity closely tracked the measured porosity at all three well locations, only the P50 estimates are shown. In all panels of Figures 6.10 and 6.11, time is shown on the vertical axis. Panel a in Figures 6.10, 6.11, and 6.12 are colored to porosity with blue indicating low porosity and red indicating higher porosity, up to 37%. Panel b in all three figures show the relative standard deviation (RSTD) of the porosity measurements. Blue indicates a lower RSTD and a more accurate porosity estimate, while red indicates a higher RSTD and a less accurate porosity measurement. In all panels of Figures 6.10 and 6.11 the sub-horizontal black traces represent the top and bottom of the reservoir. In both panels of Figure 6.10, the horizontal axis is inline number, and the vertical black and gray lines from left to right are wells F-1, F-2, and F-3, respectively. The vertical dashed line is where cross-line 197 meets inline 1084. In Figure 6.11 panels a and b the x-axis shows cross-line number with the dashed vertical line showing where cross-line 197 intersects inline 1084. The vertical black line in both panels shows the location of injection well 28-1. In both panels of Figure 6.12 the x-axis is inline number, and the y-axis is cross-line number. The white dots in Figure 6.12 are the location of injection wells. Results of the porosity inversion indicate the relatively high porosity of the reservoir zone and show some lateral porosity variation within the reservoir. At the edges of the reservoir where there is some ambiguity if the sample is reservoir sand or confining shale and at the other lower porosity zones within the reservoir, there is higher RSTD and higher error than at high porosity zones, as shown in Figures 6.10 and 6.11. Figure 6.12 shows that the porosity in the eastern portion of the

survey area is, in general, lower than that of the western and southern portions of the survey area.

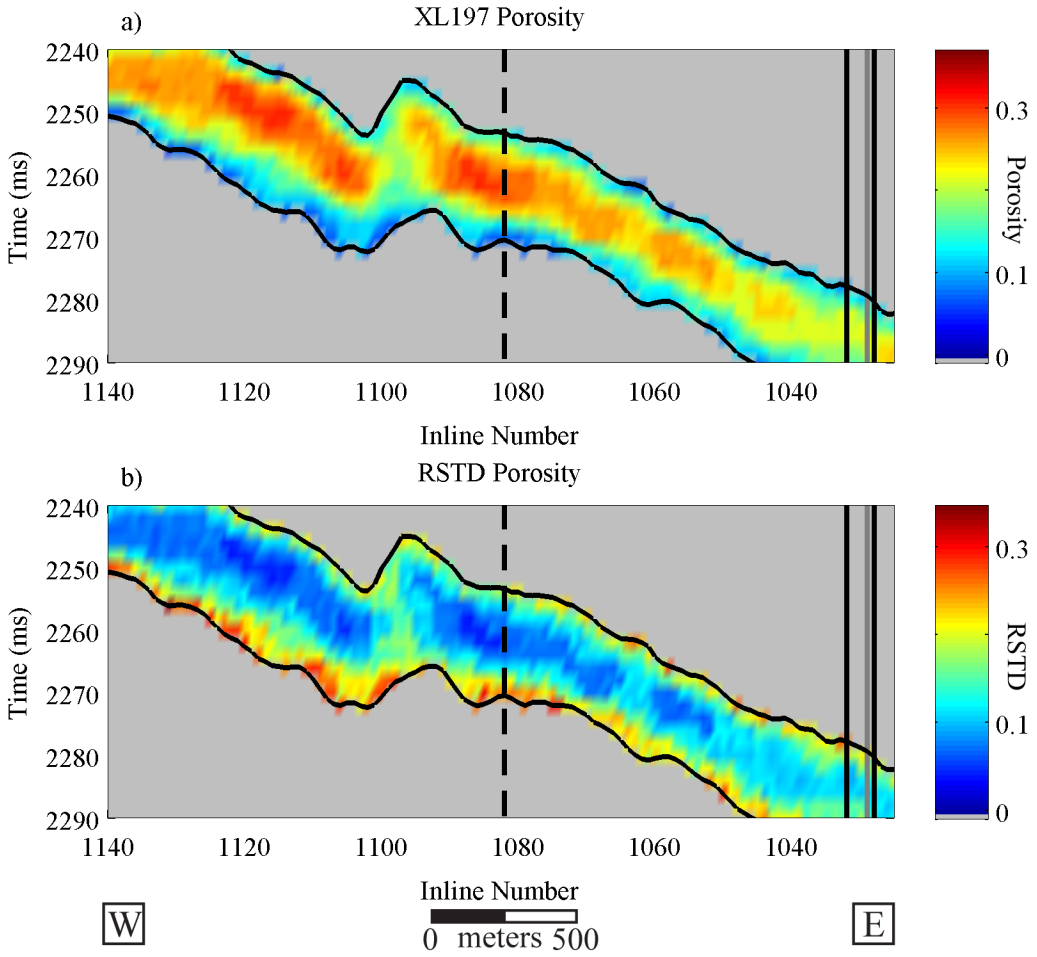

Figure 6.10: Panel a shows the P50 porosity for cross-line 197, and panel b shows the RSTD of those porosity estimates for the same cross line. In panel a, red and warm colors indicate higher porosity while blue and cool colors indicate lower porosity. In panel b, higher RSTD is indicated by red and warm colors, and low RSTD is shown by blue and other cool colors. In all panels time is shown in the y-axis, and inline number is shown on the horizontal axis.

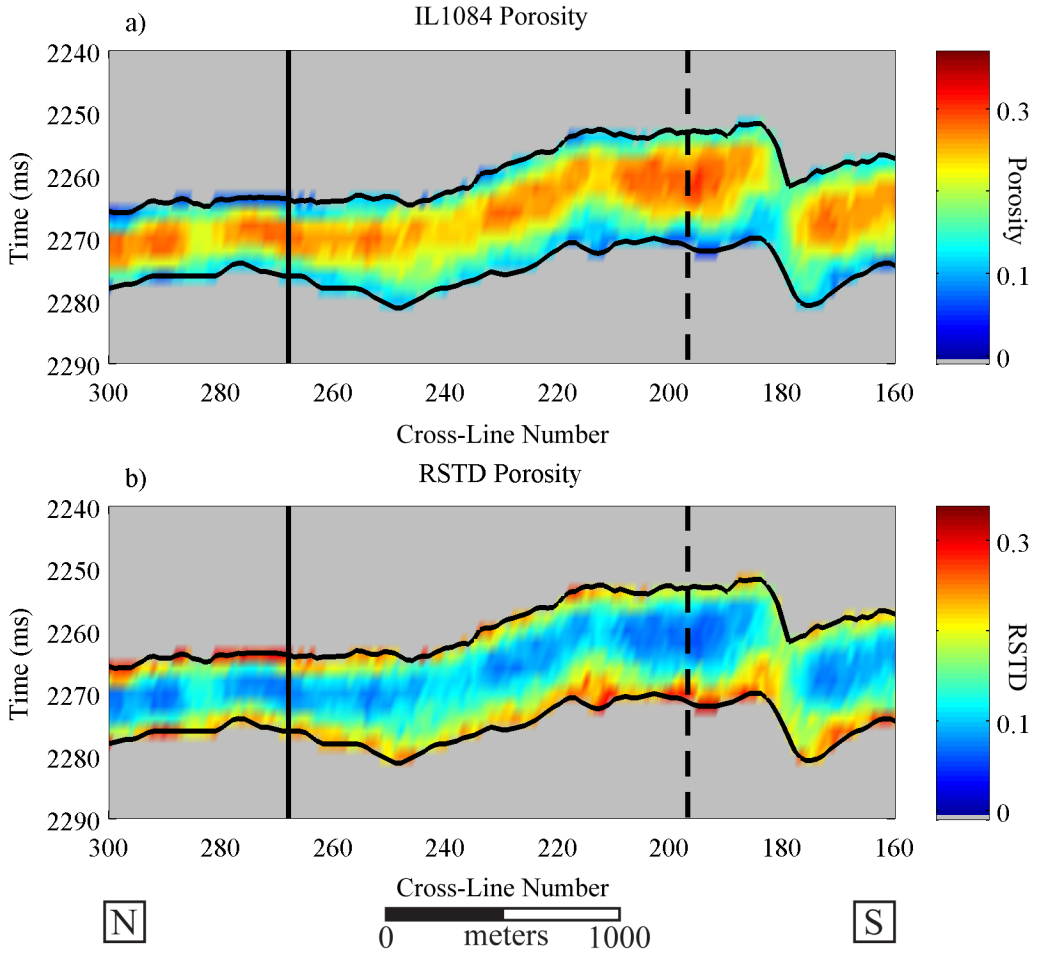

Figure 6.11: Estimated porosity and the RSTD of those porosity estimates are shown in panels a and b, respectively, for inline 1084. All panels show cross-line number on the horizontal and time on the vertical axis. The vertical black line in both panels is injection well 28-1, and the dashed vertical line is the intersection with cross-line 197. In both panels red and warm colors correspond to higher values, and blue and cool colors correspond to lower values.

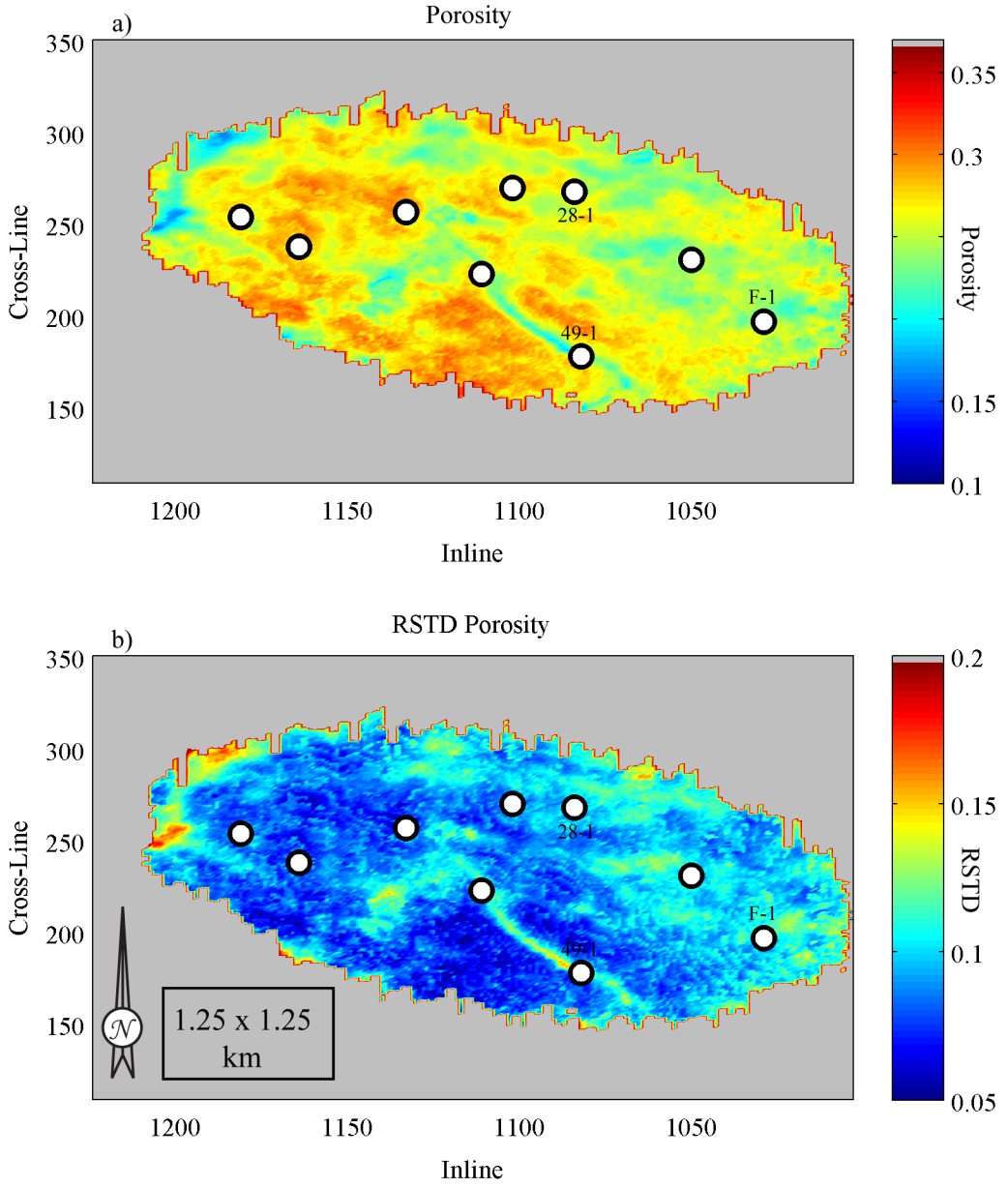

Figure 6.12: Porosity and RSTD values extracted across the top of the reservoir are shown in panel a and b, respectively. Porosity values are RMS averages of the top four samples from the reservoir. In both panels inline number is shown on the horizontal axis while cross-line number is shown on the vertical. In panels a and b red indicates both higher porosity and higher RSTD. Blue in panels a and b indicates both lower porosity and lower RSTD. Both panels share the same scale as indicated by the shown grid block in panel b.

6.4.3 Inversion for CO_2 saturation

CO_2 saturation was estimated for each of the P1 through P99 porosity volumes. Because the P50 porosity volume was shown to be closest to the measured porosity at the well locations, only the P50 CO_2 saturation is shown here. CO_2 saturation inversion results can be seen in Figures 6.13, 6.14, and 6.15. The vertical profiles in Figures 6.13 and 6.14 show time on the vertical axis. The x-axis shows inline number and cross-line number in Figures 6.13 and 6.14, respectively. The lateral black lines show the interpreted top and bottom of the reservoir. The vertical dashed line in all panels shows where the selected cross-line profile and inline profile intersect. Figure 6.15 shows the estimated CO_2 saturation calculated across the top of the reservoir and the associated RSTD values for those CO_2 estimates. The white and gray dots in all panels show the location of injection wells, with wells F-1, 28-1 marked as such.

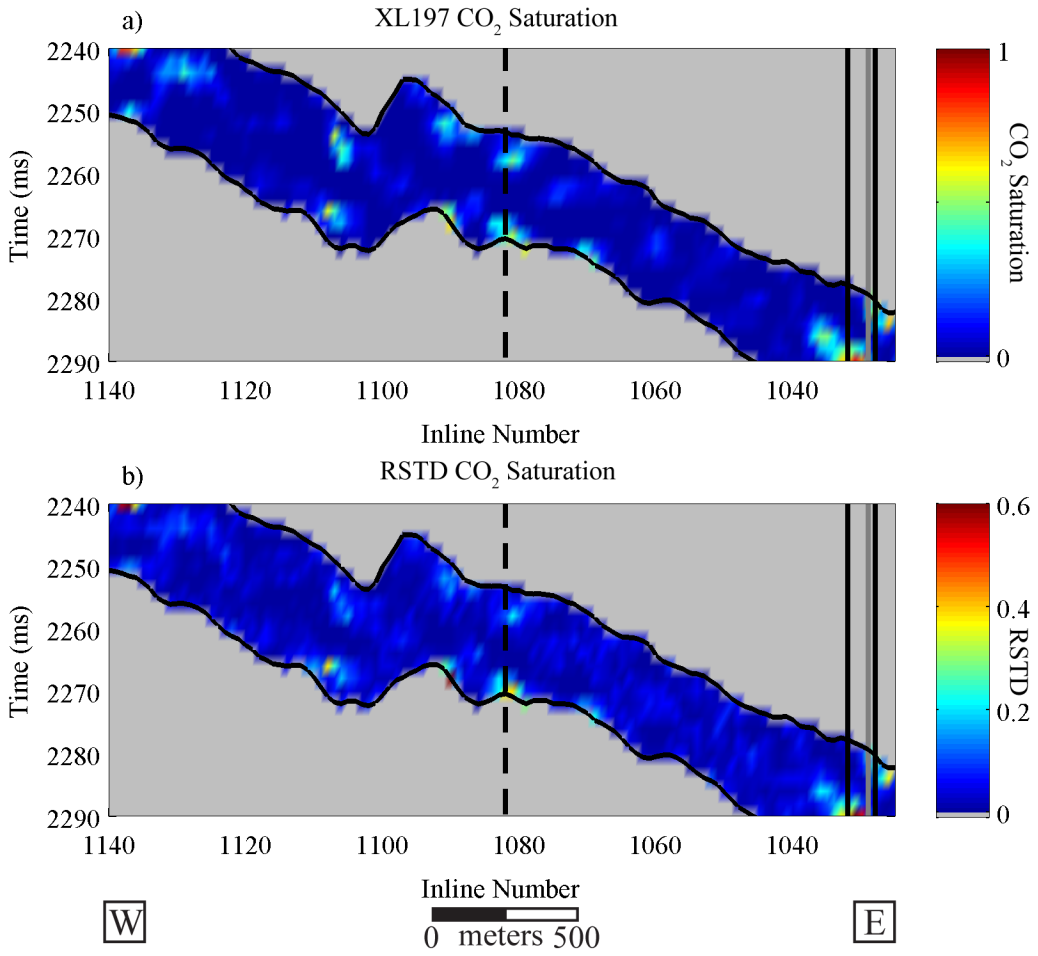

Figure 6.13: P50 CO_2 saturation is shown in panel a for cross-line 197, and the RSTD of those CO_2 saturation values are shown in panel b. The vertical axis shows time, and the horizontal axis shows inline number in both panels. The non-vertical black lines in both panels show the upper and lower limits of the reservoir. Wells F-1, F-2, and F-3 are indicated by the black, gray, and black vertical lines, respectively. The dashed black vertical line shows the intersection with inline 1084. Panel a is colored according to CO_2 saturation with dark blue indicating pure water and dark red indicating pure CO_2. Panel b is colored according to RSTD with dark blue showing a relatively low RSTD and dark red showing a relatively high RSTD.

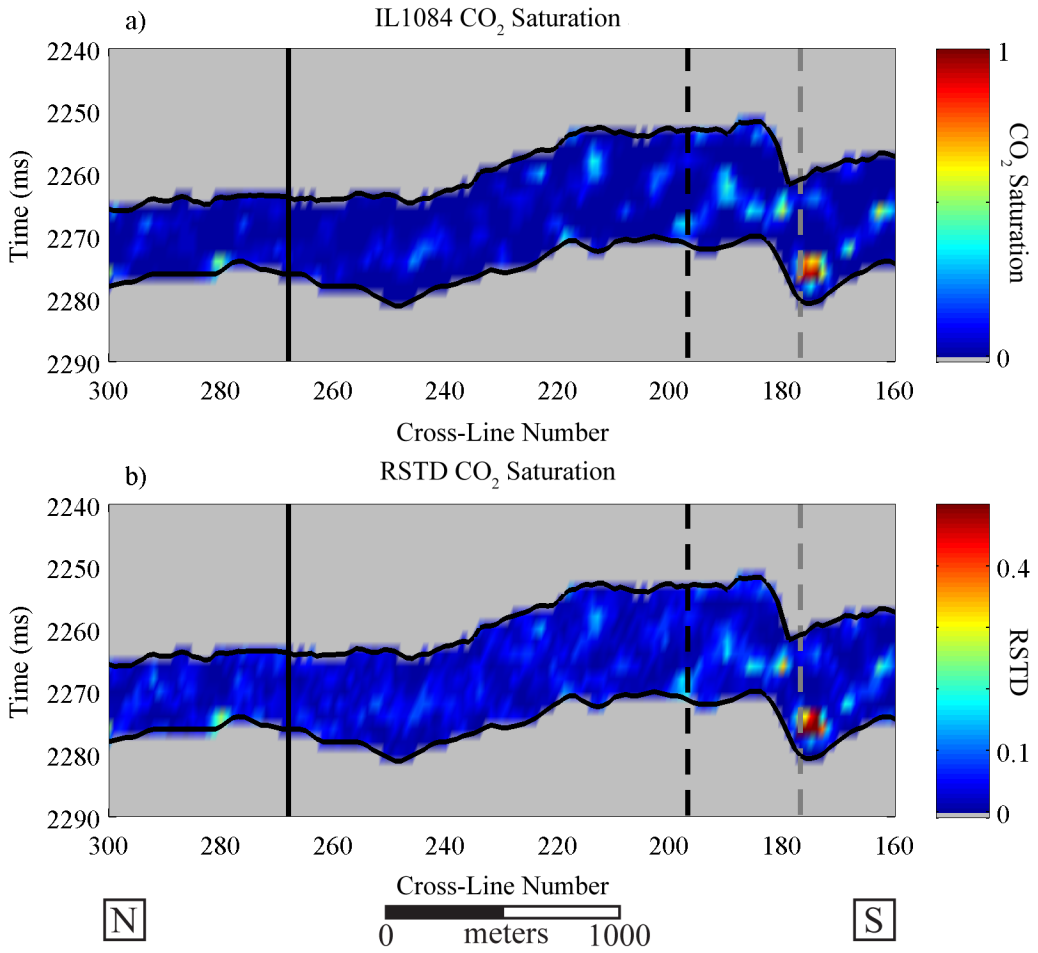

Figure 6.14: Panels a and b show the P50 CO_2 saturation and the associated RSTD for inline 1084, respectively. Cross-line number is the horizontal axis, and time is the vertical axis in both panels. Injection well 28-1 is shown by the black vertical line, and the intersection with cross-line 197 is shown by the black dashed vertical line in both panels. The dark gray dashed line in both panels shows the approximate position of injection well 49-1, which is located two inlines to the west. The black lines running across both panels delineate the reservoir zone. In panel a, CO_2 saturation is shown by color. Red indicates higher CO_2 saturation, and blue shows higher water saturation. In panel b the RSTD of the panel a values are shown with red showing higher RSTD and higher error whereas blue and cooler colors show lower RSTD and error.

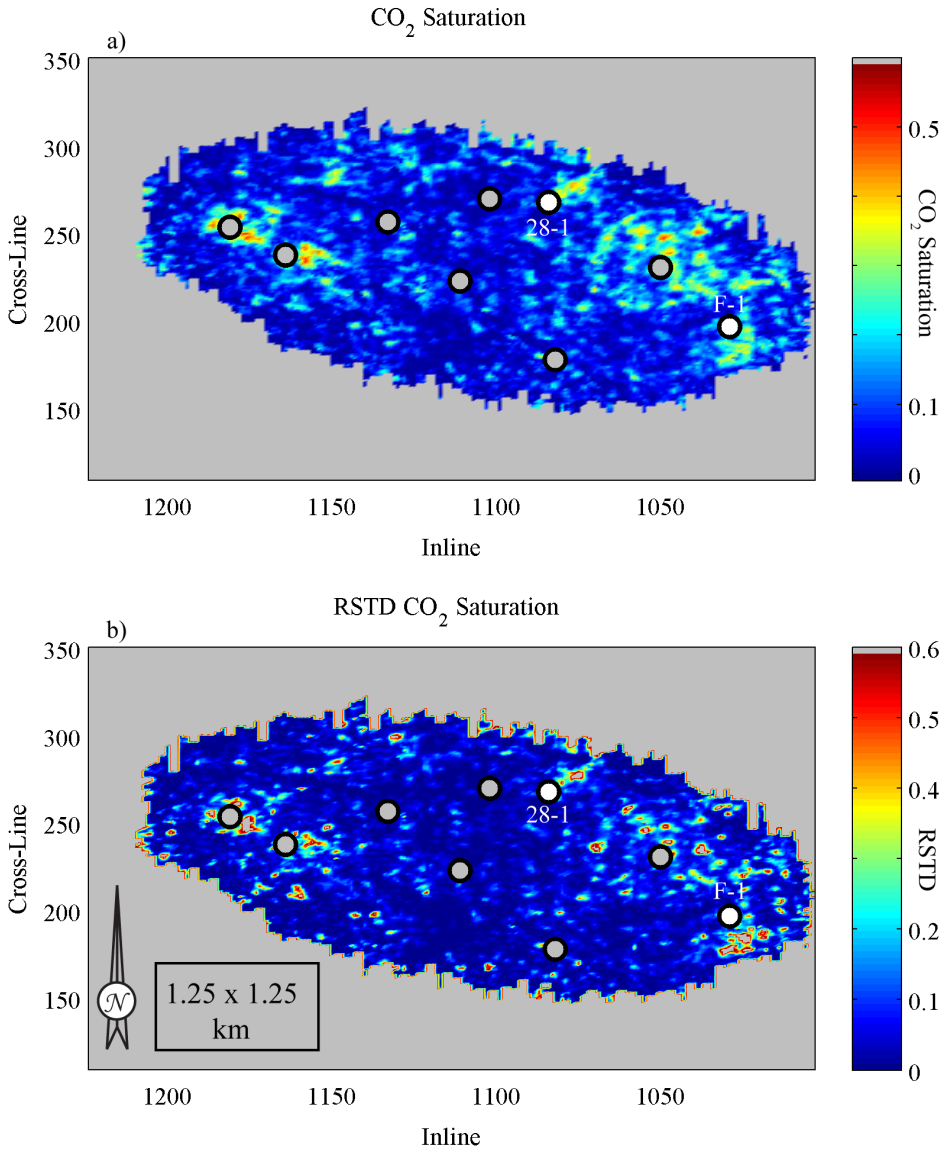

Figure 6.15: Panel a shows the estimated CO_2 saturations values as calculated from an RMS average of the top three samples in the reservoir. Panel b shows the RSTD values that associated with the CO_2 values shown in panel a. In both panels inline number is shown on the vertical axis while the x-axis shows cross-line number. The white dots are injection wells 28-1 and F-1. Additional injection wells are shown by the gray dots. Panel a is colored to CO_2 saturation with red indicating a pure CO_2 pore fluid and blue indicating a pure brine pore fluid. In panel b red indicates a higher RSTD value and higher potential error in the value, and blue indicates a lower RSTD value and lower potential error. A scaled grid cell is shown to illustrate scale for both panels.

Figure 6.13 shows modeled P50 CO_2 saturation values and the RSTD for those saturation values in panels a and b, respectively. In panel a, dark red indicates pure CO_2 saturation, and dark blue indicates pure brine saturation, with intermediate colors showing intermediate saturation levels. Panel b shows the RSTD of those estimates values with red indicating higher RSTD and blue indicating a lower RSTD. The three vertical lines in both panels from left to right are the location of injection well F-1 and monitoring wells F-2 and F-3. This figure shows an accumulation of CO_2 near injection well F-1 and a small plume of CO_2 rising to the west (left) away from the well. An accumulation of CO_2 is near the top of the reservoir at wells F-2 and F-3. Additional accumulations of CO_2 are located at other points in the reservoir and might be attributed to CO_2 plumes from out of plane injectors.

Figure 6.14 shows similar information as Figure 6.13 for the north-south oriented inline 1084. Panel a shows the P50 estimated CO_2 saturation, and panel b shows the RSTD of those CO_2 saturation values. In panel a, red and warm colors show pure CO_2 and high CO_2 saturation. Blue and cool colors show higher water saturation. In panel b, high RSTD values are shown by red and warm colors while low RSTD values are shown by blue and cool colors. In both panels the solid vertical line denotes the location of injection well 28-1. Despite the relatively large amount of CO_2 injected into this well, the inversion does not indicate an accumulation of CO_2 in any particular area.

In Figure 6.15 the CO_2 and associated RSTD values calculated across the top of the reservoir are shown. Estimated CO_2 saturation values are calculated from an RMS average of the top four samples of the reservoir zone and are shown in panel a. Panel b

shows the associated error of the CO_2 saturation estimates as a function of RSTD. In both panels, red indicates higher values and blue indicates lower values. In both panels of Figure 6.15, x-axis (east-west) is inline number and y-axis (north-south) is cross-line number. The white dots shown on both panels are the location of the injection wells with the highest recorded injection volume of CO_2. Wells 28-1, F-1, and 49-1 are labeled for reference.

6.5 DISCUSSION

In this study the inverted porosity values correlated quite closely with the measured porosity at the borehole locations. Porosity is often inversely correlated to impedance for a specific interval or rock type (e.g., Bosch et al., 2009, Mavko et al., 2009, and Avseth et al., 2005). The inverse correlation between *Ip* and porosity can be seen in the model in Figure 6.3, with similar behavior shown in all the wells as in Figures 6.2 and 6.8. When estimating porosity from inverted impedance volumes, the porosity estimates can be only as accurate as the impedance data used to generate those estimates. Comparisons of observed to inverted impedance at locations of well control indicated a fairly close match. Additionally, the measured porosity is quite similar to the estimated porosity at those same locations of well control implying that the final porosity estimate is a reliable starting point from which to estimate the pore fluid.

The results show CO_2 is most highly concentrated in approximately the same locations as the injection wells and are consistent with other studies completed on the Cranfield study area using other analytic approaches (Ditkof, 2013 and Hossieni, personal communication). However, there are many smaller pockets of high CO_2 saturation at locations away from the injection wells. Knowledge of the location of out-

of-plane injection wells can help to delineate between genuine and potentially erroneous estimations of high CO_2 saturation. For example, the gray dashed line in Figure 6.14 shows CO_2 injection well 49-1. Well 49-1 is located approximately at inline position 1082 (west of shown profile), and including it into the interpretation of the results can help explain an accumulation of CO_2 that might otherwise be considered anomalous. Looking at the results in Figure 6.15, the plume seen in Figure 6.14 at the location of 49-1 is visible. Figure 6.15 also shows that there are considerable concentrations of CO_2 in the western portion of the field at the locations of the two western-most shown injection wells. In the middle portion (approximate inline numbers 1100 to 1140) of the field there are no significant CO_2 concentrations visible at the top of the reservoir, despite there being active injector wells in that area. The lack of visible CO_2 in this portion of the field could be caused by multiple situations. It is possible that the CO_2 injection into this portion of the field has not migrated up the water column in the reservoir and is, therefore, not visible across the top of the reservoir. Additionally, and more likely, CO_2 injected into this portion of the field could have replaced hydrocarbons that were produced. The change in *Ip* resulting from hydrocarbon, notably methane, and CO_2 exchanging places is different than that from brine and CO_2, so the estimated CO_2 saturation could be less than the amount actually in place. The inability to differentiate injected CO_2 from displaced gas-phase hydrocarbon with surface seismic data is consistent with the results of laboratory scale studies completed by Siggins (2010). Studies of time-shift analysis conducted by Ditkof (2013) showed no time-shifts between the baseline seismic survey and the time-lapse survey this area of the field. The lack of observed time-shifts in this portion of the field was attributed to hydrocarbon

displacement and associated production due to CO_2 injection (Ditkof, 2013). Similarly, the estimated absence of CO_2 in the middle portion of the field is interpreted to be predominantly due to the associated production of hydrocarbons from the same areas of the reservoir.

Comparisons of the porosity and CO_2 saturation results to their corresponding RSTD values help clarify the validity of results at certain locations. In terms of porosity, higher porosity corresponds to a lower RSTD. This relationship is most evident at the top and bottom of the reservoir where resolution cannot clearly differentiate between reservoir and seal. Near the interface between reservoir and seal, low porosity values are estimated, and the RSTD for those estimates is correspondingly high. Similarly, the CO_2 saturation results show a very low RSTD at locations of pure water saturation and increasing RSTD at locations with higher CO_2 saturation. Because injection and storage reservoirs typically have efficiency factors less than 0.5 (Zhou et al., 2008), estimated CO_2 saturations approaching or exceeding that number are taken to be highly uncertain. This factor can explain why the RSTD values are very low for pure brine saturation but increase with increasing CO_2 saturation.

Another factor that could contribute to uncertainty in this study is the pore pressure changes due to CO_2 injection. The injection at wells 28-1, F-1, and other injection wells has increased pore pressure in the reservoir. The change in impedance due to pore pressure can, in some situations, be as large as the change in impedance due to CO_2 saturation (Landrø, 2001 and Stovas and Landrø, 2004). In this work a uniform pressure correction was applied to the entire field. However, a spatially variable pressure correction would provide improved results. The reduced differential pressure caused by

CO_2 injection would be heavily concentrated around the injection well and would decrease with increased lateral distance from the injectors. Future work could include additional data and processes to account for a laterally variable pressure effect on the *Ip* volumes to give a more accurate volume from which to invert porosity and CO_2 saturation.

6.6 CONCLUSIONS

This study shows the integration of rock-physics modeling and time-lapse seismic data to invert both porosity and CO_2 saturation in a double difference approach. The double difference approach to rock-physics estimations enabled the quantitative estimation of CO_2 saturation changes from changes in inverted *Ip* between different vintages of surface seismic surveys. Analysis of the change in *Ip* between two different 3D surface seismic surveys with respect to a known porosity model quantitatively linked the observed impedance changes to changes in CO_2 saturation.

Results showed that the accuracy of the porosity estimation at borehole locations was closely tied to the accuracy of the initial impedance inversion results. The use of high quality impedance inversion results and a properly calibrated rock-physics model returned relatively high quality probabilistic models for porosity within the reservoir. Probabilistic estimates of CO_2 saturation could then be derived from integrating the probabilistic porosity estimates with the observed change in seismic impedance from the baseline survey to the monitoring (time-lapse) survey. This method showed the possibility to differentiate locations with CO_2 in the pore fluid from those without CO_2 in the pore fluid. In this study, changes in impedance due to pressure were assumed constant

over the whole field. Including additional pressure information in the future might improve the accuracy of the probabilistic CO_2 saturation estimates.

Chapter 7.0: Conclusions and Future Work

7.1 CONCLUSIONS

In this dissertation I investigate the relationship between the elastic, physical rock, and fluid properties of the Cranfield reservoir. The contact cement model coupled with Gassmann fluid substitution allowed for representation of the P- and S-wave velocities and also the density of the Cranfield reservoir with different compositions of pore fluid. From the modeled relationships between the elastic properties and the physical reservoir properties, a workflow was constructed that analyzed the sensitivity of different combinations of elastic parameters to changes in fluid compositions. The elastic parameters most sensitive to fluid composition were then used with the rock-physics model and statistical methods to estimate the CO_2 saturation of the reservoir at three different scales.

The work in Chapter 4 showed that AVA was not a reliable way to differentiate between fluid saturations in the Cranfield reservoir due to the dominance of large impedance contrast between the relatively stiff sandstones of the reservoir and the relatively compliant overlying shales. However, the results of Chapter 4 did show that the best way to differentiate between different fluid saturations in the Cranfield was through the use of a combination of *Vp/Vs* and *Vp*, *Vs*, or *Ip*. None of these elastic properties alone can be used as an unambiguous direct indicator of fluid composition or porosity. However, when crossplotted against *Vp/Vs* and in conjunction with statistical methods, it is possible to assess the changes in fluid composition over time and the associated uncertainty with those changes. For a given value of *Ip*, *Vp/Vs* could be used

to indicate CO_2 saturation in the Tuscaloosa. A lower value of *Vp/Vs* correlated to an increase in CO_2 saturation for a given *Ip*. Similarly, for a given reservoir composition, increases in *Ip* correlated with decreases in porosity.

Chapter 5 built on and applied the results from Chapter 4. P- and S-impedance values were inverted from the 3C 3D VSP data. The *Ip* and *Is* values were then inverted using the rock-physics model ultimately yielding estimates of porosity and CO_2 saturation. Porosity and CO_2 saturation were estimated for the small portion of the reservoir that was sampled by both the P-wave and the mode converted S-wave data. It also demonstrated how to select and process shot points from multicomponent VSP data for completing *Ip* and *Is* inversions. This study also showed how to invert those impedance values jointly using a rock-physics model to obtain porosity and CO_2 saturation estimates. Probabilistic estimates of porosity and CO_2 saturation showed that the addition of the shear component from the S-impedance enabled estimating porosity and CO_2 saturation without the need for a time-lapse survey. The method outlined in this study provided a way to estimate reservoir porosity relatively accurately and CO_2 saturation of the sampled portion of the reservoir with somewhat less accuracy. Ultimately, the approach used in this chapter showed the capability of providing relatively narrow constraints on porosity and also providing some constraints on locations of CO_2 saturation. The distribution of CO_2 within the reservoir as shown in Chapter 5 suggests that the channelization within the Cranfield reservoir creates preferential flow pathways for the injected CO_2. Additionally, the results from this section need to be understood in relation to the fact that the data used was single fold. Because of this, it is possible that the relatively low signal to noise ratio of the data could have skewed the

results. Nonetheless, this workflow was an important step in utilizing all available data and setting up a framework for further studies.

In Chapter 6 the methods used in Chapter 5 were adapted to work with multiple vintages of poststack surface seismic data at the expense of the shear component. The *Ip* information, inverted from the baseline surface seismic data, was inverted using the brine-saturated rock-physics model yielding a probabilistic estimate of reservoir porosity. The estimated reservoir porosity and *Ip* information from the time-lapse surface seismic data were then inverted using the rock-physics model saturated with a range of CO_2 saturations. From the porosity estimates and the time-lapse *Ip* values, estimates of CO_2 saturation were generated. This portion of the study showed that it is possible to use a double difference rock physics approach to estimate both reservoir porosity and CO_2 saturation in two different steps. This work showed that the accuracy of the probabilistic porosity estimates were closely related to the quality of the impedance inversion used on the baseline surface seismic dataset. The quality of the CO_2 saturation estimates, however, was based heavily on the qualities of the baseline and time-lapse impedance inversions and on the quality of the registration between the two datasets. Areas where the datasets were poorly registered yielded highly anomalous and unreasonable CO_2 saturations. Those that were registered properly showed a positive correlation between observed CO_2 saturations and known injected volumes.

The main contribution of this dissertation is in the workflows that it provides. Taken as a whole this dissertation provides an outline from which to assess the fluid saturation properties of a reservoir from multiple different data sources. Chapter 4 outlined a method and approach to select the elastic properties of the reservoir that are

most sensitive to changes in saturation. Chapter 5 outlined a way to use those parameters in conjunction with multicomponent 3D VSP data. This is one of the first studies to use a multicomponent 3D VSP dataset to estimate CO_2 saturation within a reservoir. Few previous studies have used multicomponent 3D VSP information for quantitative interpretation and analysis of fluid saturation and porosity. The work presented in Chapter 5 shows the value of using multicomponent 3D VSP information to give relatively high resolution compressional and shear information for target areas of the reservoir. In Chapter 6 a workflow is presented that allows for estimating porosity and pore fluid from multiple vintages of relatively low-resolution surface seismic data, without the use of S-wave information. A take-away from Chapter 6 is that some data limitations, such as only having poststack data or having low-resolution data, can be overcome with the right methodology. Because of the lack of shear information, as used in Chapter 5, the methodology had to be adapted to work with poststack time-lapse information. The resulting workflow showed that useful information regarding fluid and porosity could be extracted from time-lapse surface seismic data even if the available data was poststack and lacking shear component.

The workflows presented in this dissertation need not be coupled only with the contact cement model, or be used exclusively for constraining CO_2 saturation. Through the use of the correct rock-physics model, the desired elastic parameters can be related to any number of physical properties that are different from the ones investigated here. The workflows presented in this dissertation can easily be adapted for use with a wide range of reservoir lithologies, fluid compositions, and properties of interest. This dissertation has shown the application and utility that can be gained from integrating multiple

geophysical methods. Through the careful integration of rock physics, inversion, and statistical methods, it is possible to quantitatively interpret geophysical data, and seismic data in particular, for a wide range of desired rock and fluid properties.

7.2 LIMITATIONS

The work presented in this dissertation shows that surface seismic data can be a useful tool for monitoring CO_2 after it is injected into the subsurface for either EOR or sequestration purposes. However, the results in this dissertation should not be interpreted as being error free or totally unambiguous. There is a significant amount of uncertainty in the geophysical methods presented in this dissertation. Uncertainty is present at nearly every level of data acquisition. From measured well log velocities to seismic processing, the resulting data is a best fit estimate from many measurements as opposed to being perfectly accurate measurement of the subsurface. In the workflows outlined here, there is uncertainty and some ambiguity in the rock-physics modeling from assumptions that are incorporated to compensate for the modeling being an underdetermined problem. Additionally, a large amount of uncertainty can originate from the seismic inversion process itself. Interpretation of surface seismic data is inherently non unique, and as such the results from inversion cannot be assumed to be error-free.

Additional limitations for this work can stem from the geologic properties of the reservoir itself. In relatively stiff, low porosity reservoir rock such as the Cranfield, detectability of changes in fluid saturations is greatly reduced compared to a more compliant reservoir rock. The limited detectability of saturation changes due to the stiff reservoir and pore spaces might prevent small saturation changes from being observed using methods presented in this work. Similar to the lithology parameters that limit the

detectability of fluid changes, pre-injection pore fluid composition might hinder and limit the detectability of injected CO_2 as well. This work assumed that injected CO_2 displaced brine, which has significantly different elastic properties than the injected CO_2. If, however, the injected CO_2 had displaced hydrocarbons, as is the case with EOR, the change in elastic properties between injected CO_2 and displaced fluid might not be large enough to be detected using surface seismic methods. Adding to the difficulty in modeling and detecting injected CO_2 are the considerable unknowns about the physical properties CO_2 itself. How the injected CO_2 mixes with the in situ reservoir fluids can also have an affect on detectability. Similarly, the phase of the CO_2 in the reservoir is not entirely known and can be expected to be a significant source of error and uncertainty in modeling and characterizing CO_2 saturation at injection sites.

The data itself provided their own limitations in what could be accomplished and the ultimate quality of the result. Design, acquisition, and processing of both the baseline and time-lapse surveys were not conducted with an emphasis on quantitative interpretation. Because of this, the resolution, repeatability, and the usefulness of the surveys for quantitative work was reduced. The significant change in near surface conditions during the acquisition of two surface seismic datasets resulted in significant changes in the seismic information that was not due to the changes in CO_2 saturation within the reservoir. A further limitation with the surface seismic datasets was the initial processing. A processing workflow that preserved amplitudes and offset dependent change in reflectivity would have improved the usefulness of the datasets and might have reduced the uncertainty in the final results. Additionally, while injection of CO_2 for EOR increases the economic viability of CO_2 injection, the addition of hydrocarbons in the

modeling adds significant complexity and uncertainty in the results. For high quality monitoring of CO_2 injection, ensuring the maximum possible repeatability in survey design and acquisition is important. As a result a permanent or semi-permanent seismic array to enable high repeatability and consistent geometries between different vintages of seismic acquisition might improve data quality when implemented in conjunction with processing workflows designed for quantitative interpretation. Furthermore, selecting CO_2 injection sites away from hydrocarbon production and other human induced changes in the subsurface can help improve the data quality and reduce monitoring uncertainty. Similarly, locating injection site in areas with surface conditions conducive to high repeatability surface seismic data acquisition might help improve the quality of monitoring results. However, implementing these recommendations can be at a potential economic cost relative to injection sites similar to the Cranfield site.

In spite of these limitations and uncertainties, the workflows and results presented in this dissertation show that geophysical methods involving 3D VSP datasets and time-lapse surface seismic datasets can provide significant useful information for this site in terms of CO_2 injection for utilization or storage purposes. Much like exploring for hydrocarbons using seismic techniques, the results for one location are often not applicable to other locations. Geophysical data must be analyzed at each site particularly where the geologic setting varies from one site to the next.

7.3 FUTURE WORK

In this work, assumptions were made regarding how overburden and pore pressure affected the elastic properties of the reservoir rock. Specifically in Chapter 6 it was assumed that an increase of pore pressure from the injection of CO_2 did not

contribute to lateral changes in impedance between the baseline and the time-lapse data. However, injection of fluid into a reservoir can and has been shown to raise pore pressure both directly around the injection well and, to a lesser degree, at areas away from the injection well. Including a pore pressure term or a pressure-dependent rock-physics model could help to improve the accuracy and validity of the results. An additional possible avenue from which to continue this work would be the use of prestack surface seismic data. Including prestack surface seismic data would provide some S-wave information and much larger coverage area than that provided strictly by the multicomponent 3D VSP. Shear information from prestack data could allow for improved fluid estimates over a larger area.

An additional avenue for future work could include further work with multicomponent 3D VSP data. In this study a single PP shot point was selected in addition to a single PS shot point. This effectively resulted in single fold data. Using VSP data with additional closely located shot points could effectively raise the fold used at each location and possibly result in significantly improved quality of results. A final area of further study would be to expand the number of shot points selected for PP and PS extractions. In this study only one pair of points was selected, yielding a single 2D slice of the reservoir. Use of additional shot points and improved VSP geometry could significantly increase the area of the reservoir imaged using this technique. Incorporating additional shot points into this dissertation was beyond the limitations of the existing 3D VSP data. However, as additional datasets become available, exploring and expanding on this technique could provide relatively higher resolution of larger areas of a reservoir than were used in this study.

Appendix A

In the contact cement model (Dvorkin and Nur, 1996), the following equations were used to calculate the elastic and physical properties of the cemented standstone of the Cranfield Reservoir. For modeling the reservoir the critical porosity (ϕ_0) was set to equal 0.37.

$$K_{eff} = \frac{1}{6} C(1-\phi_0) M_c \dot{S}_n \quad \text{(A1)}$$

$$\mu_{eff} = \frac{3}{5} K_{eff} + \frac{3}{20} C(1-\phi_0) \mu_c \dot{S}_\tau \quad \text{(A2)}$$

$$M_c = \rho_c V_{Pc}^2 \quad \text{(A3)}$$

$$\mu_c = \rho_c V_{Sc}^2 \quad \text{(A4)}$$

In Equations A3 and A4 ρ_c is the density, and V_{Pc} and V_{Sc} are the P and S-wave velocities, respectively, of the contact cement. The terms $\dot{S}_n$ and $\dot{S}_\tau$ are proportional to the compressional and shear moduli of a simple grain pack of two grains cemented to each other. The $\dot{S}_n$ and $\dot{S}_\tau$ terms are a function of the cement properties and the volume of cement present at the grain contact. Coordination number is represented by *C* and is the number of grain contacts for each individual grain. Typically 9 is used for the *C* value.

$$\dot{S}_n = A_n \alpha^2 + B_n \alpha + C_n \quad \text{(A6)}$$

$$A_n = -0.024153 \Lambda_n^{-1.3646} \quad \text{(A7)}$$

$$B_n = 0.20405 \Lambda_n^{-089008} \quad \text{(A8)}$$

$$C_n = 0.00024649\Lambda_n^{-1.9864} \tag{A9}$$

$$\dot{S}_\tau = A_\tau \alpha^2 + B_\tau \alpha + C_\tau \tag{A10}$$

$$A_\tau = -10^{-2}(2.26\sigma^2 + 2.07\sigma + 2.3)\Lambda_\tau^{0.079\sigma^2+0.1754\sigma-1.342} \tag{A11}$$

$$B_\tau = (0.0573\sigma^2 + 0.0937\sigma + 0.202)\Lambda_\tau^{0.0274\sigma^2+0.0529\sigma-0.8765} \tag{A12}$$

$$C_\tau = 10^{-4}(9.654\sigma^2 + 4.94\sigma + 3.1)\Lambda_\tau^{0.01867\sigma^2+0.4011\sigma-1.8186} \tag{A13}$$

$$\Lambda_n = \frac{2\mu_c}{\pi\mu}\frac{(1-\sigma)(1-\sigma_c)}{(1-2\sigma_c)} \tag{A14}$$

$$\Lambda_\tau = \frac{\mu_c}{\pi\mu} \tag{A15}$$

In Equations A6 through A15 σ is the Poissons ratio of the grains, and μ is the shear modulus of the grains. Similarly, σ_c and μ_c are the Poissions ratio and shear modulus of the intergranular cement, respectively. In these equations α is a cement deposition parameter that can be related to both the porosity of the sandstone (ϕ) and the means of cement deposition. The first method of cement deposition is that the cement is deposited only at grain contacts. In the second method of cement deposition, cement is deposited to evenly coat the grains. The equation for α that relates to the first method of cement deposition is given by Equation A16 while the α term that relates to the second method of cement deposition is given by Equation A17. For this dissertation I used the α given by Equation A17.

$$\alpha = 2\left[\frac{\phi_0-\phi}{3C(1-\phi_0)}\right]^{\frac{1}{4}} \tag{A16}$$

$$\alpha = \left[\frac{2(\phi_0-\phi)}{3(1-\phi_0)}\right]^{\frac{1}{2}} \tag{A17}$$

References

Aki, K., and P. G. Richards, 1980, Quantitative Seismology: Theory and Methods: W.H. Freeman and Co, San Francisco.

Allam, A. A., and Y. Ben-Zion, 2012, Seismic velocity structures in the southern California plate-boundary environment from double-difference tomography: Geophysics Journal International, **190**, 1181–1196.

Artola, F., and V. Alvarado, 2006, Sensitivity analysis of Gassman's fluid substitution equations: Some implications in feasibility studies of time-lapse seismic reservoir monitoring: Journal of Applied Geophysics, **59**, 47–52.

Avseth, P., J. Dvorkin, G. Mavko, and J. Rykkje, 2000, Rock physics diagnostics of North Sea sands: line between microstructure and seismic properties: Geophysical Research Letters, **27**, 2761–2764.

Avseth, P., T. Mukerji, and G. Mavko, 2005, Quantitative seismic interpretation, applying rock physics to reduce interpretation risk: Cambridge University Press.

Avseth, P., and S. Norunn, 2011, Rock physics modeling of static and dynamic reservoir properties – a heuristic approach for cemented sandstone reservoirs: The Leading Edge, **30**, 90–96.

Bachrach, R., 2006, Joint estimation of porosity and saturation using rock-physics modeling: Geophysics, **71**, O53–O63.

Backus, G. E., 1962, Long-wave elastic anisotropy produced by horizontal layering: Journal of Geophysical Research, **68**, 4427–4440.

Biot, M. A., 1956, Theory of propagation of elastic waves in a fluid saturated porous solid. I. Low-frequency range: Journal of the Acoustical Society of America, **28**, 168–178.

Blangy, J. P., S. Strandenes, D. Moos, and A. Nur, 1993, Ultrasonic velocities in sands, revisited: Geophysics, **58**, 344–356.

Bortfeld, R., 1961, Approximation to reflection and transmission coefficients if plane longitudinal and transverse waves: Geophysical Prospecting, **9**, 485–503.

Bosch M., L. Cara, J. Rodrigues, A. Navarro, and M. Diaz, 2007, A Monte Carlo approach to the joint estimation of reservoir and elastic parameters from seismic amplitudes: Geophysics, **72**, O29–O39.

Bosch, M., C. Carvajal, J. Rodrigues, A. Torres, M. Aldana, and J. Sierra, 2009, Petrophysical seismic inversion conditioned to well-log data: Methods and application to a gas reservoir: Geophysics, **74**, O1–O15.

Burch, T., B. Hornby, H. Sugianto, and B. Nolte, 2010, Subsalt 3D VSP imaging at Deimos Field in the deep water Gulf of Mexico: The Leading Edge, **29**, 680–685.

Calò, M., L. Parisi, and D. Luzio, 2013, Lithospheric P- and S-wave velocity models of the Sicilian area using WAM tomography: procedure and assessments: Geophysics Journal International, **195**, 625–649.

Carter, R. W., and K. T. Spikes, 2013, Sensitivity analysis of Tuscaloosa sandstones to CO_2 saturation, Cranfield field, Cranfield, MS: International Journal of Greenhouse Gas Control, **18**, 485–496.

Carter, R., K. Spikes, and T. Hess, 2014, Inversion of multicomponent 3D VSP data for porosity and CO_2 saturation at the Cranfield injection site, Cranfield, MS: Interpretation, **2**, SE77–SE89.

Castagna, J. P., and M. Backus, 1993, Offset Dependent Reflectivity—Theory and Practice of AVO Analysis: Society of Exploration Geophysics.

Castagna, J. P., H. W. Swan, and D. J. Foster, 1998, Framework for AVO gradient and intercept interpretation: Geophysics, **63**, 948–956.

Chadwick, A., G. Williams, N. Delepine, V. Clochard, K. Labat, S. Sturton, M. Buddensiek, M. Dillen, M. Nickel, A. Lima, R. Arts, F. Neele, and G. Rossi, 2010, Quantitative analysis of time-lapse seismic monitoring data at the Sleipner CO_2 storage operation: The Leading Edge, **29**, 170–177.

Daley, T. M., J. B. Ajo-Franklin, and C. Doughty, 2011, Constraining the reservoir model of an injected CO_2 plume with crosswell CASSM at the Frio-II brine pilot: International Journal of Greenhouse Gas Control, **5**, 1022–1030.

Dang, Y., L. Bing, X. Miao, P. Wang, S. Zhang, and L. Shen, 2010, Delineating oil-sand reservoirs with high-resolution PP/PS processing and joint inversion in the Junggar Basin, Northwest China: The Leading Edge, **29**, 1212–1219.

Das, A., and M. Batzle, 2008, Modeling studies of heavy oil in between solid and fluid properties: The Leading Edge, **27**, 1116–1123.

Denli, H., and L. Huang, 2009, Double-difference elastic waveform tomography in the time domain: 79th Annual International Meeting, SEG, Expanded Abstracts, 2302–2306.

Ditkof, J., 2013, Time-lapse seismic monitoring for enhanced oil recovery and carbon capture and storage field site at the Cranfield field, Mississippi: The University of Texas at Austin Masters Thesis.

Dodds, K., T. Daley, B. Freifeld, M. Urosevic, A. Kepic, and S. Sharma, 2009, Developing a monitoring and verification plan with reference to the Australian Otway CO_2 pilot project: The Leading Edge, **28**, 812–818.

Dulaijan, A. K., C. J. Owus, and C. D. Weber, 2012, Azimuthal anisotropy analysis of walkaround vertical seismic profiling: a case study from Saudi Arabia: Geophysical Prospecting, **60**, 1082–1094.

Dvorkin, J., G. Mavko, and A. Nur, 1991, The effects of cementation on the elastic properties of granular material: Mechanics of Materials, **12**, 207–217.

Dvorkin, J., A. Nur, and H. Yin, 1994, Effective properties of cemented granular material: Mechanics of Materials, **18**, 351–366.

Dvorkin, J., and A. Nur, 1996, Elasticity of High-porosity sandstones: Theory for two North Sea datasets: Geophysics, **61**, 1363–1370.

Eidsvik, J., H. Omre, T. Mukerji, G. Mavko, and P. Avseth, 2002, Seismic reservoir prediction using Bayesian integration of rock physics and Markov random fields: A North Sea example: The Leading Edge, **21**, 290–294.

Fomel, S., and M. M. Backus, 2003, Multicomponent seismic data registration by least squares: 73rd Annual International Meeting, SEG, Expanded Abstracts, 781–784.

Gassmann, F., 1951, Uber die elastizitat poroser medien: Vier. Natur Gesellschaft, **96**, 1–23.

Ghaderi, A., and M. Landrø, 2009, Estimation of thickness and velocity changes of injected carbon dioxide layers from prestack time-lapse seismic data: Geophysics, **74**, O17–O28.

Grechka, V., P. Contreras, and I. Tsvankin, 2000, Inversion of normal moveout for monoclinic media: Geophysical Prospecting, **48**, 577–602.

Grude, S., M. Landrø, and B. Osdal, 2012, Time lapse pressure-saturation discrimination for CO_2 storage at Snøhvit field: 82nd Annual International Meeting, SEG, Expanded Abstracts, 1–5.

Hampson, D. P., B. H. Russell, and B. Bankhead, 2005, Simultaneous inversion of prestack seismic data: 75th Annual International Meeting, SEG, Expanded Abstracts, 1633–1636.

Hardage, B., 1985, Vertical seismic profiling (2nd Edition): Geophysical Press.

Hardage, B. A., P. E. Murray, R. Remington, M. De Angelo, D. Sava, H. H. Roberts, W. Shedd, and J. Hunt Jr., 2009, Multicompenent Sesimic Technology Assessment of Fluid-gas Expulstion Geology and Gas-Hydrate Systems: Gulf of Mexico, in T. Collett, A. Johnson, C. Knapp, and R. Boswell, eds, Natural gas hydrates: Energy resource potential and associated geologic hazards: American Association of Petroleum Geologists Special Publication, **89**, 247–265.

Hashin, Z., and S. Shtrikman, 1963, A variational approach to the elastic behavior of multiphase materials: Journal of the Mechanics and Physics of Solids, **11**, 127–140.

Haas, A., and O. Dubrule, 1994, Geostatistical Inversion – a sequential method of stochastic reservoir modeling constrained by seismic data: First Break, **12**, 561–569.

Han, D.-H., A. Nur, and D. Morgan, 1986, Effects of porosity and clay content on wave velocities in sandstones: Geophysics, **51**, 2093–2107.

Hovorka, S.D., T. A. Meckel, R. H. Trevino, J. Lu, J. P. Nicot, J. W. Choi, D. Freeman, P. Cook, T. M. Daley, J. B. Ajo-Franklin, B. M. Freifeild, C. Doughty, R. C. Carrigan, D. L. Brecque, Y. K. Kharaka, J. J. Thordsen, T. J. Phelps, C. Yang, K. D. Romanak, T. Zhang, R. M. Holt, J. S. Lindler, and R. J. Butch, 2011, Monitoring a large volume CO_2 injection: Year two results from SECARB project at Denbury's Cranfield Mississippi, USA: Energy Procedia, **4**, 3478–3485.

IPCC, 2013, Climate Change 2013: The physical science basis. Contributions of working group 1 to the fifth assessment report of the Intergovernmental Panel on Climate Change In: Stocker, T. F., D. Qin, G. K. Plattner, M. Tignor, S. K. Allen, J. Boschung, A. Naules, Y. Xia, V. Bex, and P. M. Midgley, (editors). Cambridge, United Kingdom and New York, NY, USA.

Jiang, M., and K. T. Spikes, 2013, Estimation of reservoir properties of the Haynesville Shale by using rock-physics modeling and grid searching: Geophysics Journal International, **195**, 315–329.

Joy, C. A., 2011, The effects of pressure variations and chemical reactions on the elasticity of the lower Tuscaloosa sandstone of the Cranfield field, MS: The University of Texas at Austin Master Thesis.

Knight, R., and R. Nolen-Hoeksema, 1990, A laboratory study of dependence of elastic wave velocities on pore scale fluid distributions: Geophysical Research Letters, **17**, 1529–1532.

Knott, C. G., 1899, Reflection and refraction of elastic waves, with seismological applications: Philosophical Magazine, **48**, 567–569.

Kordi, M., S. Hovorka, K. Milliken, R. Treviño, and J. Lu, 2010, Diagenesis and reservoir heterogeneity in the Lower Tuscaloosa Formation at Cranfield Field,

Mississippi: presented at the 60th Annual Convention of the Gulf Coast Association of 96 Geological Societies and the Gulf Coast Section of SEPM. San Antonio, Texas. October 10-12, 2010. GCCC Digital Publication Series #10–13.

Landrø, M., 2001, Discrimination between pressure and fluid saturation changes from time-lapse seismic data: Geophysics, **66**, 836–844.

Lee, M. W., 1984a, Vertical seismic profiles at the multi-well experimental site, Garfield County, Colorado: USGS Open-File Report 84–168.

Lee, M. W., 1984b, Delineation of lenticular type sand bodies by the vertical seismic profiling method: USGS Open-File Report 84–265.

Lu, J., P. J. Cook, S. A. Hisseini, C. Yang, K. D. Romanak, T. Zhang, B. M. Freifeld, R. C. Smyth, H. Zeng, and S. D. Hovorka, 2012a, Complex fluid flow revealed by monitoring CO_2 injection in a fluvial formation: Journal of Geophysical Research, **117**, B03208.

Lu, J., Y. Kharaka, J. Thordsen, J. Horita, A. Karamalidis, C. Griffith, A. Hakala, G. Ambats, D. Cole, T. J. Phelps, M. A. Manning, P. Cook, and S. Hovorka, 2012b, CO_2–rock–brine interactions in Lower Tuscaloosa Formation at Cranfield CO_2 sequestration site, Mississippi, USA: Chemical Geology, **291**, 269–277.

Lu, J., M. Kordi, S. D. Hovorka, T. A Meckel, and C. A. Christopher, 2013, Reservoir characterization and complications for trapping mechanisms at Cranfield CO_2 injection site: International Journal of Greenhouse Gas Control, **18**, 361–374.

Lumley, D., 2010, 4D seismic monitoring of CO_2 sequestration: The Leading Edge, **29**, 150–155.

Ma, J., and I. Morozov, 2010, AVO modeling of pressure-saturation effects in Weyburn CO_2 sequestration: The Leading Edge, **29**, 178–183.

Mathieson, A., J. Midgley, K. Dodds, I. Wright, P. Ringrose, and N. Saoul, 2010, CO_2 sequestration monitoring and verification technologies applied at Krechba, Algeria: The Leading Edge, **29**, 216–222.

Mavko, G., T. Mukerji, and N. Godfrey, 1995, Predicting stress-induced velocity anisotropy in rocks: Geophysics, **60**, 1081–1087.

Mavko, G., and T. Mukerji, 1998, Bounds on low-frequency seismic velocities in partially saturated rocks: Geophysics, **63**, 918– 924.

Mavko, G., T. Mukerji, and J. Dvorkin, 2009, The Rock Physics Handbook: Cambridge University Press.

Miao, X., and T. Zuk, 2007, Anisotropic velocity updating for converted-wave prestack time migration: Geophysics, **72**, D29–D32.

Mindlin, R. D., 1949, Compliance of elastic bodies in contact: Journal of Applied Mechanics, **16**, 259–568.

Moyano, B., E. H. Jensen, and T. A. Johansen, 2011, Improved quantitative calibration of rock physics models: Petroleum Geoscience, **17**, 345–354.

Mukerji, T., A. Jorstad, P. Avseth, G. Mavko, and J. R. Granli, 2001, Mapping lithofacies and pore-fluid probabilities in a North Sea reservoir: Seismic inversions and statistical rock physics: Geophysics, **66**, 988–1001.

Müller, K., W., W. L. Soroka, B. N. P. Paulsson. S. Marmash, M. A. Baloushi, and O. A. Jeelani, 2010a, 3D VSP technology now a standard high-resolution reservoir-imaging technique: Part 1, acquisition and processing: The Leading Edge, **29**, 686–697.

Müller, K., W., W. L. Soroka, B. N. P. Paulsson, S. Marmash, M. A. Baloushi, and O. A. Jeelani, 2010b, 3D VSP technology now a standard high-resolution reservoir-imaging technique: Part 2, interpretation and value: The Leading Edge, **29**, 688–704.

Nur, A., 1971, Effects of stress on velocity anisotropy in rocks with cracks: Journal of Geophysical Research, **76**, 2022–2034.

Nur, A., and G. Simmons, 1969, Stress-induced velocity anisotropy in rocks: An experimental study: Journal of Geophysical Research, **74**, 6667.

Reuss, A., 1929, Berechnung der Fleissgrenzen von Mischkristallen auf Grund der Plastizitatsbedingung fur Einkristalle: Zeitschrift fur Angewandte Mathematik aus Mechanik, **9**, 49–58.

Rowbotham, P. S., D. Marion, P. Lamy, E. Insalaco, P. A. Swaby, and Y. Boisseau, 2003, Multidisciplinary stochastic impedance inversion: Integrating geological understanding and capturing reservoir uncertainty: Petroleum Geoscience, **9**, 287–294

Russell, B. H., K. Heldin, F. J. Hilterman, and R. L. Lawrence, 2003, Tutorial: Fluid-property discrimination with AVO: A Biot-Gassmann perspective: Geophysics, **68**, P29–P39.

Rutherford, S. R., and R. H. Williams, 1989, Amplitude-versus-offset variations in gas sands: Geophysics, **54**, 680–688.

Sayers, C., M., 1988, Stress-induced ultrasonic wave velocity anisotropy in fractured rock: Ultrasonics, **26**, 311–317.

Sears, T., J., P. J. Barton, and S. C. Singh, 2010, Elastic full waveform inversion of multicomponent ocean-bottom cable seismic data; application to Alba Field, U.K. North Sea: Geophysics, **75**, R109–R119.

Sen, M. L., 2006, Seismic inversion: 120 pp, Society of Petroleum Engineers Publications, Richardson, Texas.

Shuey, R. T., 1985, A simplification of the Zoepprtiz equations: Geophysics, **50**, 609–614.

Siggins, A. F., M. Lwin, and P. Wisman, 2010, Laboratory calibration of the seismo-acoustic response of CO_2 saturated sandstone: International Journal of Greenhouse Gas Control, **4**, 920–927.

Simm, R., R. White, and R. Uden, 2000, The anatomy of AVO crossplots: The Leading Edge, **19**,150–155.

Spikes, K., T. Mukerji, J. Dvorkin, and G. Mavko, 2007, Probabilistic seismic inversion based on rock-physics models: Geophysics, **72**, R87–R97.

Stine, J. A., 2004, Sensitivity of AVO reflectivity to fluid properties in porous media: The University of Texas at Austin Masters Thesis.

Stovas, A., and M. Landrø, 2004, Optimal use of PP and PS time-lapse stacks for fluid-pressure discrimination: Geophysical Prospecting, **52**, 301–312.

Tao, Y., M. K. Sen, R. Zhang, and K. Spikes, 2013, A robust stochastic inversion workflow for time-lapse data: hybrid starting model and double difference inversion: Journal of Geophysics and Engineering, **10**, 035011.

Takahashi, I., 2000, Quantifying information and uncertainty of rock property estimation from seismic data: Stanford University PhD Dissertation.

Tosaya, C.A., 1982, Acoustical Properties of Clay-bearing Rocks: Stanford University PhD Dissertation.

Urosevic, M., R. Pevzner, A. Kepic, P. Wisman, V. Shulakova, and S. Sharma, 2010, Time-lapse seismic monitoring of CO_2 injection into a depleted gas reservoir – Naylor Field, Australia: The Leading Edge, **29**, 164–169.

Verdon, J. P., J. M. Kendall, J. D. White, D. A. Angus, Q. J. Fisher, and T. Urbancic, 2010, Passive seismic monitoring of carbon dioxide storage at Weyburn: The Leading Edge, **29**, 208–214.

Voigt, W., 1907, Bestimmung der Elastizitatskonstanten von Eisenglanz: Anallen der Physik, **24**, 129–140.

Wang, Z., 2000, Dynamic versus static properties of reservoir rocks, in seismic and acoustic velocities in reservoir rocks: SEG Geophysics Reprint Series, **19**, 531–539.

Williams, G., and A. Chadwick, 2012, Quantitative seismic analysis of a thin layer of CO_2 in the Sleipner injection plume: Geophysics, **77**, R245–R256.

Zhang, R., and J. Castagna, 2011, Seismic sparse-layer reflectivity inversion using basis pursuit decomposition: Geophysics, **76**, R147–R158.

Zhang, R., R. Ghosh, M. K. Sen, and S. Srinivasan, 2013a, Time-lapse surface seismic inversion with thin bed resolution for monitoring CO_2 sequestration: A case study

from Cranfield Mississippi: International Journal of Greenhouse Gas Control, **18**, 430–438.

Zhang, R., X. Song, S. Fomel, M. K. Sen, and S. Srinivasan, 2013b, Time-lapse seismic data registration and inversion for CO_2 sequestration study at Cranfield: Geophysics, **78**, B329–B338.

Zheng, Y., P. Barton, and S. Singh, 2011, Strategies for elastic full waveform inversion of time-lapse Ocean Bottom Cable (OBC) seismic data: 81st Annual Meeting, SEG, Expanded Abstracts, 4195–4200.

Zhou, Q., T. J. Birkholzer, C. F. Tsang, and J. Rutqvist, 2008, A method for quick assessment of CO_2 storage capacity in closed and semi-closed saline formations: International Journal of Greenhouse Gas Control, **2**, 626–639.

Zoeppritz, K., 1919, ErdbebenwellenVIIIB, Ueber Reflection and Durchgang seismischer Wellen durch Unitestigkeitsflaechen: Goettinger Nachrichten, **I**, 66–84.

Vita

Russell Wirkus Carter was born in Anchorage, Alaska. He graduated from Wasilla High School in 2003, and went on to complete a Bachelor of Arts, double majoring in Geology and International Relations, from Colgate University in 2007. From 2007 to 2010 he worked as a geologist in California, Denmark, Germany, UAE, Qatar, and Bahrain. He started graduate school at the University of Texas at Austin in 2010 to pursue the degree of Doctor of Philosophy in Geophysics. During the summers of 2012 and 2013 he worked as an intern for ConocoPhillips in Anchorage, Alaska and Houston, Texas.

Permanent contact: rwirkuscarter@gmail.com

This dissertation was typed by the author.